UNIVERSITY OF SOUTHAMPTON

Faculty of Engineering and Applied Sciences
School of Electronics and Computer Science
Sustainable Electronic Technologies

Machine learning enabled thermoelectric generator design and optimization

by

Yuxiao Zhu
ORCiD: 0000-0003-1867-2297

A thesis for the degree of
Doctor of Philosophy

July 2024

University of Southampton

Abstract

Faculty of Engineering and Applied Sciences
School of Electronics and Computer Science
Sustainable Electronic Technologies

Doctor of Philosophy

Machine learning enabled thermoelectric generator design and optimization

by Yuxiao Zhu

With increasing global recognition of environmental protection and carbon emission reduction, renewable energy development is drawing heightened attention. At the same time, energy conversion efficiency needs to be improved, requiring techniques such as energy harvesting. In this context, thermoelectric generators (TEGs), which can recycle thermal energy, have garnered significant interest from researchers.

Traditional modelling of thermoelectric generators (TEGs) typically involves two approaches: theoretical models and mathematical models. The theoretical, 1-D and 2-D mathematical models often suffer from reduced accuracy due to the omission of specific parameters. On the other hand, the 3-D mathematical model, commonly known as 3-D finite element analysis (FEA), is hindered by slow computational speeds. To address these limitations, this thesis proposes a novel approach using artificial neural networks (ANNs) to model TEGs, achieving accuracy and computational efficiency.

This thesis first demonstrates the application of ANNs in constructing a forward model for a thermoelectric generator. This method attains computation speeds thousands of times faster than 3D FEA while preserving 98% accuracy compared to the results from 3D FEA. Furthermore, when integrated with optimization algorithms, this model can effectively optimize the structure of the thermoelectric generator, demonstrating a significant advancement in modelling and design efficiency.

Later in this work, an ANN has been applied to build accurate and fast forward modelling of the segmented thermoelectric generator (STEG). More importantly, an iterative method is adopted in the ANN training process to improve accuracy without increasing the dataset size. This approach strengthens the proportion of the high-power performance in the STEG training dataset. Without increasing the size of the training dataset, the accuracy was increased from 92% to 98%. Coupling with a genetic algorithm, the trained artificial neural networks can optimise design within 10 seconds for each operating condition. It is over 4,000 times faster than the optimization performed by the conventional FEA model. Such an accurate and fast modeller also allows the mapping of the STEG power against different parameters.

Then, the hybrid TEG system is analyzed. Radiative cooling (RC) can provide a continuous temperature difference, which a TEG can convert into electrical power. This novel combination of radiative cooling with TEG expands the category of sustainable energy sources for energy harvesting. Using 3D FEA, this system provides a systematic analysis of the concept of RC-TEG by investigating the impact of radiative cooler properties, TEG parameters, and environmental conditions to provide a complete picture of the performance of RC-TEG devices. The capability of RC-TEG to provide continuous power supply is simulated using real-time environmental data from both Singapore and London on two different days of the year, demonstrating continuous power supply sufficient for a wide range of IoT devices in all four scenarios.

Finally, this thesis introduces an ANN-based model designed to predict the performance of hybrid PV-TEG systems. Utilizing a cyclic approach, the ANN model incorporates various factors, including PV coating, morphology, TEG geometry parameters, temperature-dependent material properties, and environmental conditions like solar irradiance and convection. The model's integrated nature allows independent use of PV and TEG components, enhancing its adaptability and generalizability. Remarkably, compared to FEA simulations, the ANN model demonstrates over 98% accuracy and a significant boost in computational efficiency, with a 6,000-fold increase in simulation speed. This efficiency enables extensive parameter sweeps, offering insightful analysis into the influence of various factors on the PV-TEG system's performance.

Overall, the ANN model's rapid processing capabilities are particularly beneficial for large-scale simulations and practical applications in renewable energy technology.

Declaration of Authorship

I declare that this thesis and the work presented in it is my own and has been generated by me as the result of my own original research.

I confirm that:

1. This work was done wholly or mainly while in candidature for a research degree at this University;
2. Where any part of this thesis has previously been submitted for a degree or any other qualification at this University or any other institution, this has been clearly stated;
3. Where I have consulted the published work of others, this is always clearly attributed;
4. Where I have quoted from the work of others, the source is always given. With the exception of such quotations, this thesis is entirely my own work;
5. I have acknowledged all main sources of help;
6. Where the thesis is based on work done by myself jointly with others, I have made clear exactly what was done by others and what I have contributed myself;
7. Parts of this work have been published as:

   Yuxiao Zhu, Daniel W. Newbrook, Peng Dai, C.H. Kees de Groot, Ruomeng Huang, Artificial neural network enabled accurate geometrical design and optimisation of thermoelectric generator, Applied Energy, 2022,
   URL: `https://doi.org/10.1016/j.apenergy.2021.117800`.

   Yuxiao Zhu, Daniel Newbrook, Peng Dai, Jian Liu, Kees de Groot, and Ruomeng Huang, Segmented thermoelectric generator modelling and optimisation using artificial neural networks by iterative training, Energy & AI, vol. 12, no. December 2022, URL: `https://doi.org/10.1016/j.egyai.2022.100225`.

Yuxiao Zhu, Daniel W. Newbrook, C.H. Kees de Groot, Ruomeng Huang, Comprehensive analysis of radiative cooling enabled thermoelectric energy harvesting, JPhys Photonics, vol. 5, 2023,
URL: `https://doi.org/10.1088/2515-7647/accac1`.

Signed:.. Date:..................

Acknowledgements

As I stand at this significant milestone of completing my PhD thesis, I am filled with deep gratitude and appreciation for those who have been pillars of support, guidance, and inspiration throughout this challenging yet rewarding journey.

First and foremost, I extend my heartfelt thanks to my supervisor, Ruomeng Huang, whose expertise, patience, and insightful guidance have been invaluable. Ruomeng's unwavering support and encouragement have shaped my research and significantly contributed to my personal and professional growth.

I am equally grateful to Kees de Groot and Harold Chong, whose profound knowledge and perspectives have enriched my understanding and appreciation of my research field. Their constructive feedback and encouragement have been crucial in navigating the complexities of my study, and their belief in my abilities has been a constant source of motivation.

I would also like to sincerely thank my classmate and friend, Daniel. His companionship, shared insights, and support have made the arduous journey of PhD research more enjoyable and meaningful. Daniel's presence has been a reminder of the strength found in collaboration and mutual support.

Similarly, my gratitude extends to Peng Dai, whose friendship, understanding, and shared moments of both challenge and triumph have greatly enriched my PhD experience. Peng's solidarity and encouragement have been a beacon of light during the most demanding phases of my research.

The journey to completing this thesis has been a testament to the power of collaboration, mentorship, and friendship. Each of you has left an indelible mark on my journey; I am eternally grateful for that. Thank you for your invaluable contributions, believing in me, and being part of this significant chapter of my life.

To my beloved family,

This thesis stands as a tribute to my academic journey and the boundless love, sacrifice, and support you've given me during my studies abroad. Every page reflects your belief in me, showing the strength and encouragement I've received from you.

To my mom, Dingying, the guiding light in my life, our weekly chats across the miles have been my haven. Filled with laughter, advice, and sometimes tears, these conversations have kept me connected to home, no matter how far away I am. Your wisdom and love have guided me, lighting my way through both tough and happy times.

To my dad, Deyou, your hard work and sacrifices have made my dreams possible. Your quiet strength and never-give-up attitude have taught me to keep going and to be dedicated, helping shape who I am today.

This dedication is a small way to show my deep thanks for all you've done. I've reached this important point because of you. You've supported my studies and been my emotional support, motivation, and home.

List of Publications

Journal Publications

1. Yuxiao Zhu, Daniel W. Newbrook, Peng Dai, C.H. Kees de Groot, Ruomeng Huang, Artificial neural network enabled accurate geometrical design and optimisation of thermoelectric generator, Applied Energy, 2022, `https://doi.org/10.1016/j.apenergy.2021.117800`.
2. Yuxiao Zhu, Daniel W. Newbrook, Peng Dai, C.H. Kees de Groot, Ruomeng Huang. Segmented thermoelectric generator modelling using artificial neural networks, Energy proceedings, 2022, `https://www.energy-proceedings.org/wp-content/uploads/icae2021/1643099407`.
3. Yuxiao Zhu, Daniel Newbrook, Peng Dai, Jian Liu, Kees de Groot, and Ruomeng Huang, Segmented thermoelectric generator modelling and optimisation using artificial neural networks by iterative training, Energy & AI, vol. 12, no. December 2022, `https://doi.org/10.1016/j.egyai.2022.100225`.
4. Yuxiao Zhu, Daniel W. Newbrook, C.H. Kees de Groot, Ruomeng Huang, Comprehensive analysis of radiative cooling enabled thermoelectric energy harvesting, JPhys Photonics, vol. 5, 2023, `https://doi.org/10.1088/2515-7647/accac1`.
5. Yuxiao Zhu, Daniel W. Newbrook, Peng Dai, Jian Liu, Jichao Li, Chunming Wang, Harold Chong, C.H. Kees de Groot, Ruomeng Huang, Artificial neural network enabled photovoltaic-thermoelectric generator modelling and analysis (Submitted).
6. Callum Wheeler, Yuxiao Zhu, Kai Sun, Ruomeng Huang, Otto L. Muskens and Cornelis H. (Kees) de Groot, Temperature Coefficient of Resistivity of W-doped VO_2 Thin Films via Atomic Layer Deposition for High Sensitivity Microbolometer Designs (Submitted and not in this thesis).

Conferences

1. Yuxiao Zhu, Daniel W. Newbrook, Peng Dai, C.H. Kees de Groot, Ruomeng Huang, Segmented thermoelectric generator modeling using artificial neural networks. The 13th International Conference of Applied Energy, 2021 (Oral).
2. Yuxiao Zhu,Daniel W. Newbrook, Peng Dai, C.H. Kees de Groot, Ruomeng Huang, Accurate thermoelectric generator performance evaluation by deep learning using artificial neural network, Virtual Conference of Thermoelectric, 2021 (Oral).
3. Yuxiao Zhu, Daniel W. Newbrook, C.H. Kees de Groot, Ruomeng Huang, Machine learning enabled thermoelectric generator modelling and optimisation, The 18th European Conference of Thermoelectric, 2022 (Barcelona, Spain).
4. Yuxiao Zhu, Daniel W. Newbrook, C.H. Kees de Groot, Ruomeng Huang, Machine learning enabled thermoelectric generator modelling and optimisation, Thermoelectric Network UK Meeting 2022, 2022 (Southampton, UK).

Contents

Definitions and Abbreviations

TEG	Thermoelectric generator
ANN	Artificial neural network
GA	Genetic algorithm
FEA	Finite element analysis
$STEG$	Segmented thermoelectric generator
RC	Radiative cooling
PV	Photovoltaic
ZT	Figure of merit
$T-D$	Temperature-dependent
MPP	Maximum power point
Q_{in}	Heat flux density (mW/cm^2)
Q_H	Hot-side heat flux
Q_C	Cold-side heat flux
T_H	Hot-side temperature (K)
T_C	Cold-side temperature (K)
ρ_C	Contact resistivity ($\Omega \cdot m^2$)
H_{TE}	Height of the TEG leg (mm)
H_{IC}	Height of the interconnect (mm)
H_t	Height of the ceramic layer (mm)
FF	Fill factor
W_n	Width of the n-type leg (mm)
W_p	Width of the p-type leg (mm)
A	Surface area (cm^2)
PD_{max}	Power density (mW/cm^2)
σ	Electrical conductivity (S/m)
η	Efficiency
S	Seebeck coefficient ($\mu V/K$)
k	Thermal conductivity ($W/(m \cdot K)$)
α_N	The ratio of n-type high-temperature material height to the leg height
α_P	The ratio of p-type high-temperature material height to the leg height
R^2	Coefficient of determination value
$Conv_T$	Top convection coefficient ($W/(m^2K)$)

$Conv_B$	Bottom convection coefficient ($W/(m^2K)$)
W_{Cooler}	Width of radiative cooling (mm)
$\varepsilon_{8-13\mu m}$	Average emissivity in 8-13 μm
$\varepsilon_{0.3-2.5\mu m}$	Average emissivity in 0.3-2.5 μm
P_{solar}	Solar irradiance (W/m^2)
P_{PV}	Photovoltaic power density (W/m^2)
P_{rad}	Radiative power density (W/m^2)
$P_{non-rad}$	Non-radiative power density (W/m^2)
T_{PV}	Photovoltaic temperature (K)
P_{TEG}	TEG power density (W/m^2)
P_{in}	From PV input heat flux density (W/m^2)
T_{amb}	Ambient temperature (K)
M_{PV}	Photovoltaic morphology
C_{PV}	Photovoltaic coating

Chapter 1

Introduction

1.1 Background

Producing a secure, sustainable, and efficient energy supply that meets the demands of the growing global population while simultaneously reducing the environmental impact of CO_2 emissions is widely recognized as one of the most critical societal challenges for the current generation [1]. According to the report, as of December 2020, global CO_2 emissions were estimated to reach 33 gigatonnes (GT) in 2021. This figure represents only a 1.2% reduction from the levels recorded in 2019, as per the International Energy Agency (IEA) 2021 data [2]. The slight decline in CO_2 emissions in 2021 is attributed to the global economic slowdown caused by the Covid-19 pandemic, which began at the end of 2019. However, this reduction is not expected to be sustainable as the global economy begins to recover. In response to the challenge of controlling carbon emissions, many international organizations have collaborated to develop a road map to manage and reduce CO_2 emissions. According to this road map, CO_2 emissions are projected to increase from 34 gigatonnes (GT) in 2020 to 36 GT in 2030 and are expected to remain around this level until 2050. To achieve this, a significant shift towards renewable energy sources is necessary, with the road map suggesting that renewable energy will need to account for most global energy consumption.

In modern society, electricity is an essential source of energy. To generate electricity, the current efficiency of conventional combustion energy sources, such as coal, natural gas, and oil, is only about 40%, with the majority of this energy being wasted as heat. Recovering just 1% of this wasted energy could yield over 200 TWh of electricity annually, with an estimated market value of around $20 billion, and bring significant associated benefits, including a reduction in CO_2 emissions [3]. Converting this wasted heat into sustainable energy, and thereby into electricity, is a critical challenge that necessitates energy harvesting.

1.2 TEG design

A thermoelectric generator (TEG), capable of harvesting waste heat and converting this thermal energy into electricity, can significantly enhance energy supply efficiency and reduce reliance on fossil fuels [4]. These TEGs are particularly valued for their ability to convert thermal energy directly into electrical energy. However, traditional methods, such as using steam to drive turbines, require substantial thermal energy and space. On the contrary, TEGs based on the Seebeck effect are formed by connecting an n-type semiconductor material electrically in series and thermally in parallel across a temperature gradient to a p-type semiconductor material, allowing current flow between the two [5]. A typical thermoelectric device is shown in Figure 1.1[6]. One n-type and one p-type form the basic structure of a single thermoelectric generator pair. By connecting multiple pairs of these generators, more power can be generated. Unlike traditional energy generators, thermoelectric generators convert heat directly into electricity without the need for moving structures or liquids. They offer a relatively long service life and operate with minimal noise [7]. These advantages are significant for devices that need to function at high temperatures over extended periods. Apart from the basic thermoelectric generator structure, various other thermoelectric configurations have received considerable attention.

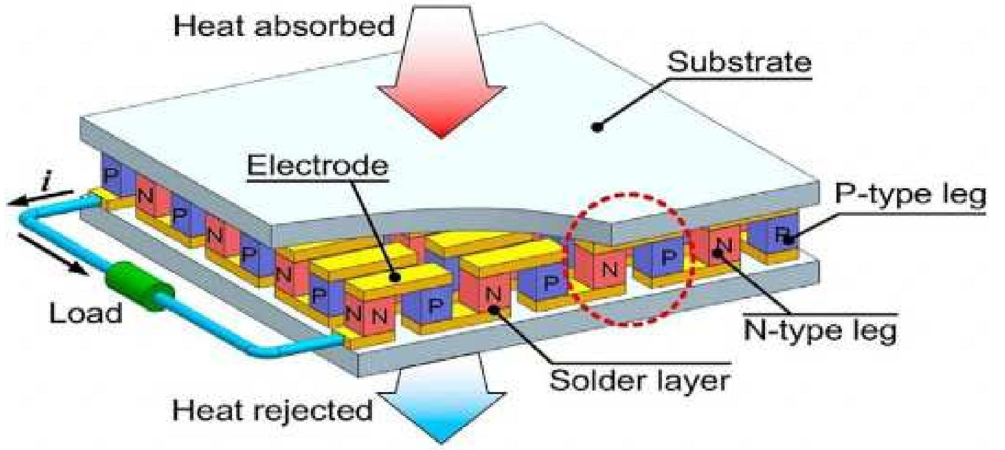

FIGURE 1.1: Schematic overview of the thermoelectric module. Reprinted from [4]

In particular, the segmented TEG (STEG) structure involves combining two thermoelectric materials, one optimized for high temperatures and the other for low temperatures, spliced together. When STEG works in a higher temperature difference, this design can ensure that both materials operate within their most suitable temperature ranges, potentially enhancing the overall efficiency of the TEG system by leveraging the distinct thermal properties of different materials. Thermoelectric generators have applications in areas such as automotive heat recovery [8] and water pipe heat harvesting.

Apart from the standalone TEG structures, TEG can also combined with other devices to form hybrid energy harvesting systems. An essential application of TEG involves their combination with radiative cooling (RC) devices, representing a new sustainable energy source. Radiative cooling is a ubiquitous process by which a surface loses heat through thermal radiation. The significant temperature difference between the earth (around 300 K) and space (2.7 K) can potentially be utilized to cool the earth's surface by emitting thermal infrared radiation to space through the atmosphere [9][10]. The high transmittance window in the atmosphere at a wavelength between 8-13 um coincidentally matches well with the blackbody radiation from a 300 K object, making the concept of radiative cooling possible by avoiding radiation re-absorption. Based on this, RC is a substantial heat source as it can generate continuous temperature differences. Combining RC with TEG can build a device that produces continuous power 24 hours daily.

Furthermore, thermoelectric generators can enhance energy harvesting by integrating with other renewable sources, such as photovoltaic (PV) systems. Among all renewable energy sources [11], the photovoltaic cell has garnered significant attention due to its simple structure and high efficiency. It is a device that converts solar energy into electricity. While considerable progress has been made in PV system development, much work is still needed to enhance overall efficiency and reduce costs [12]. A typical photovoltaic module can convert 5-20% of incident solar radiation into electricity, depending on the type of solar cell and climatic conditions [13]. However, a significant proportion of the remaining incident solar radiation is inadvertently converted into heat. This escalates the operational temperature of PV panels, leading to efficiency degradation, a challenge plaguing the domain of PV systems [14].

Despite the vast demand for renewable energy and the great potential of TEG, the applications of TEGs are relatively limited. The niche application of TEGs is primarily due to their low conversion efficiency. More research is needed to improve efficiency in addressing this. Currently, TEG research focuses on finding new materials, but based on new materials, the potential for enhancing TEG efficiency by studying complex structures based on these materials cannot be ignored.[15].

Developing n-type and p-type semiconductor materials with better thermoelectric performance (evaluated by the figure-of-merit, ZT) is one of the critical requirements to achieve higher TEG power generation performance. In recent years, with further research into thermoelectric generator materials, many state-of-the-art high-quality thermoelectric materials have been developed [16]. Several material engineering strategies such as carrier concentration optimization, nanostructuring, and band engineering have been proposed and materialized in significantly improved ZT values [17] [18] [19]. Materials including SnSe, PbTe-SrTe, and mosaic crystals have all been reported to have ZT larger than 2, showing encouraging prospects for the large-scale application of TEGs. However, even high-quality materials can lead to low output efficiency if the

TEG structure is poorly designed. Many sub-optimal designs prevent thermoelectric generators from utilizing superior materials for higher power generation efficiencies. Thus, an effectively designed thermoelectric generator is essential for superior materials. It is also necessary to study how to create a better TEG.

Furthermore, the same is the case for optimizing thermoelectric generator structures. Even for the simplest thermoelectric generator models, many factors are needed to optimize the design to the best possible level. First, the geometrical parameters include the different leg lengths, the area of the upper and lower surfaces, the spacing between the n-type and p-type legs and the thickness of each layer. Other parameters, such as contact resistance, can also lead to significant variations in efficiency. The parameters are also interrelated, so finding a suitable figure is challenging. In addition, other environmental variables need to be considered, such as ambient temperature, convective heat flux, and the input of heat flux or temperature differences. Changes in these parameters can also alter the optimal structure of the thermoelectric generator. The vast array of parameter variations complicates the design of thermoelectric generators.

An accurate and fast calculated model is essential to design an optimal TEG. Generally, there are two main modelling approaches: theoretical model and mathematical model. The theoretical model is built by simplifying the variables, for example, converting the temperature-dependent variables into constant and then integrating them according to physical equations to obtain the result. However, since the calculation process omits many conditions, the results are not as accurate. Dimensions can categorize mathematical modelling. One-dimensional modelling focuses on calculations along a single dimension. After subdividing, it maintains consistent default parameters for each segment and determines the overall output through integration. This approach allows for the capture of temperature-dependent parameters within the one-dimensional framework. However, its drawback lies in overlooking errors introduced by parameters in other dimensions. In a real-world scenario, temperature and other parameters can vary significantly across different dimensions (e.g., spatial coordinates like x, y, z). A one-dimensional model may fail to capture the effects of such variations. With the development of computer technology, 3-D mathematical models, known as finite element analysis (FEA), can accurately calculate various transient and steady-state physical variables. It can calculate data such as the output power of thermoelectric generators using FEA. Common FEA includes relevant commercial software (COMSOL, ANSYS). This simulation software enables the calculation of a wide range of data for complex conditions. In the case of thermoelectric generators, data such as output power and efficiency can be well simulated.

Nevertheless, with this comes the problem that physical variables in complex environments require many calculations to implement. Even though computers are running at significantly higher speeds than a decade ago, designing and optimizing TEG based on 3-D models still requires significant computational resources, especially when the model is complex. Therefore, since both previously used modelling methods have limitations, a better method that enables accurate and quick prediction of TEG power performance would benefit the TEG design.

Artificial Neural Networks (ANN) have garnered widespread attention globally due to their efficiency in analyzing vast datasets and their revolutionary impact on fields such as computer vision and speech recognition [20][21][22]. Recently, deep learning has been proposed to replace the conventional intuition-based design process in nano-photonics [23][24], providing accurate and efficient design of optical storage [25], meta-surfaces [26][27], and nanostructured colour filters [28]. It has also found application in solid-state systems to discover and predict the performance of new materials due to its outstanding capability of finding optimal solutions from enormous data with much lower demands on computational resources [29][30]. Several pioneering works have also been reported using machine learning to facilitate research on thermoelectric materials [31][32][33]. This data-driven approach aims to predict the results based on approximation without explicitly solving the question. This approach is helpful for modelling systems involving many parameters with complicated relations where analytical methods are not readily available. Before the ANNs can perform the intended forward modelling, a training process needs to occur in which a dataset is required. This dataset, which generally involves many input(s) and output(s) relations, needs to be generated by mathematical simulation. However, this is a one-time investment. No more computational resources will be consumed once the network is trained correctly. One of the essential features of ANNs is that they do not need to know the physical meaning of the data but instead look for patterns directly from the data. This advantage fits well with the dilemma faced by thermoelectric generators. Therefore, ANN meets these requirements and is introduced as a new research tool for modelling thermoelectric generators. The parameters of the thermoelectric generator can then be optimized in a backward method through other machine learning algorithms, such as genetic algorithms that find the maximum value [34].

1.3 Aims and objectives

This PhD project aims to explore the possibility of using ANN as a fast and accurate method in modelling TEG. The aim is to leverage the computational power and adaptability of ANNs to improve the efficiency and accuracy of TEG models, potentially enhancing the design and optimization of these energy systems. The specific objectives are as follows:

- To develop an ANN model that predicts the output power density and efficiency with high accuracy and speed, utilizing specific geometrical parameters and operating conditions.

- To identify and optimize the parameters by integrating a genetic algorithm with the ANN model.
- To model a complicated TEG structure, for example, segmented TEG, using ANN and aims for high accuracy in the modelling process.
- To conduct systematic analyses of the integration of radiative cooling with TEG to evaluate their combined performance and efficiency.
- To model and analyze photovoltaic thermoelectric generator (PV-TEG) systems to assess their performance and efficiency under various conditions.

This report is arranged in the following order. Chapter 1 focuses on the relevant concepts that need to be applied in the latter part of the report and why thermoelectric generators were chosen as the basis for the study. Chapter 2 provides a more detailed description of the structure, materials, and operating principles. Furthermore, a brief literature review of thermoelectric generators includes the architecture of TEG. Some concepts of machine learning and genetic algorithms are also introduced. Chapter 3 describes the research approach used in this report. The corresponding experimental steps and procedures are described in detail. Chapters 4 and 5 show the experimental results and the related analysis of conventional bulk TEG and segmented TEG, respectively. Chapter 6 demonstrates the comprehensive analysis of the radiative cooling thermoelectric generator model. Chapter 7 shows the photovoltaic thermoelectric generator model process and analysis. In the end, Chapter 8 summarises this report's empirical content and results, followed by some perspectives for future work.

Chapter 2

Background and literature review

This chapter comprehensively summarises the principles underlying thermoelectric generators, including their materials and structures. It also includes a literature review of various studies related to thermoelectric generators. Building on this foundation, the chapter then explores the integration of thermoelectric generators with radiative cooling and photovoltaic systems. Finally, it introduces this thesis's important machine learning algorithms, specifically artificial neural networks and genetic algorithms.

2.1 Principle of thermoelectric

Two centuries ago, it was discovered that when a heat source is applied to the junction of two dissimilar metals, a voltage can be detected across the two sides. This phenomenon is known as the Seebeck effect, which forms the basis of thermoelectric generators. With the rapid development of semiconductor materials, thermoelectric generators exhibit various properties that distinguish them from conventional energy generators [35]. A typical thermoelectric generator, as depicted in Figure 2.1, consists of n-type and p-type semiconductors. The red leg represents the n-type material, while the blue is the p-type material. The electrodes, usually made of a metal such as copper, are shown in yellow. The top and bottom sides of the generator are insulated and thermally conductive materials, such as Aluminium Nitride [36] and Silicon Dioxide [37], indicated by the brown part in the picture. Voltage can be detected at the load resistance by maintaining a temperature difference between the top and bottom surfaces. T_H is the hot side that applies heat flux, and the T_C is the cold side that remains at a low temperature. The green arrow is the direction of the current flow.

The working principle of thermoelectric generators is based on the Seebeck effect. When heat flows into the top surface while the bottom surface remains cooler, a temperature

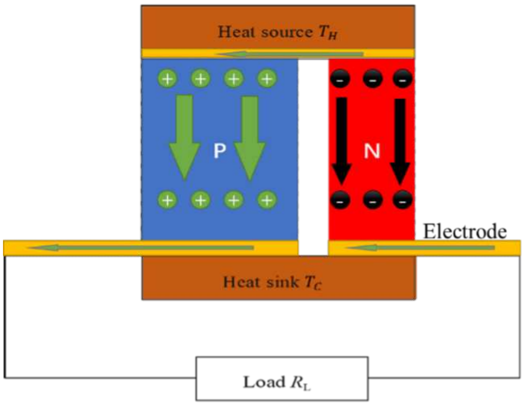

FIGURE 2.1: Schematic of a single-pair thermoelectric generator model.

difference is created between these two surfaces. This temperature difference generates a potential difference, the direction of which depends on the material. In an n-type semiconductor, where electrons are the charge carriers, these electrons move from the high-temperature side to the low-temperature side. This movement equates to an electric current flowing through the n-type semiconductor from the bottom to the top.

Conversely, in p-type semiconductors, the charge carriers are holes, which flow from high to low temperatures according to the Seebeck effect. Consequently, the equivalent current flows from the top to the bottom surface.

2.2 Thermoelectric materials

From a material perspective, the performance of materials in thermoelectric generators (TEGs) can be determined by a key parameter known as the figure of merit (ZT). It is expressed as [38]:

$$ZT = \frac{S^2\sigma}{\kappa}T \tag{2.1}$$

where σ is the electrical conductivity, κ is the thermal conductivity, S is the Seebeck coefficient, and T is the absolute temperature. The Seebeck coefficient is expressed as [39]:

$$S = \frac{\Delta V}{\Delta T} \tag{2.2}$$

where ΔT is a temperature difference, and ΔV is electrostatic potential difference.

The optimization of the materials can be described by Eqs. 2.1 with high Seebeck coefficient S, high electrical conductivity σ and low thermal conductivity κ. The thermal conductivity κ of thermoelectric materials is differentiated between the two main components: electronic thermal conductivity κ_e and lattice (phonon) thermal conductivity κ_l. One of the main challenges in thermoelectric materials is the interdependence of electrical conductivity σ and thermal conductivity κ [40]. To overcome this, researchers employ several strategies: nanostructuring [41], complex crystal structures [42] and doping [43].

Several common materials with notable ZT are summarized in the literature [44], as illustrated in Figure 2.2. According to the figure, a material with ZT around or over 1 represents a relatively good material for TEG design. The diagram shows that bismuth telluride is used for low-temperature applications, effective at just under 200 °C; lead telluride is suitable for medium to low-temperature ranges, operating at 300-600 °C. For high-temperature applications, silicon-germanium is used, functioning effectively at temperatures over 800 °C.

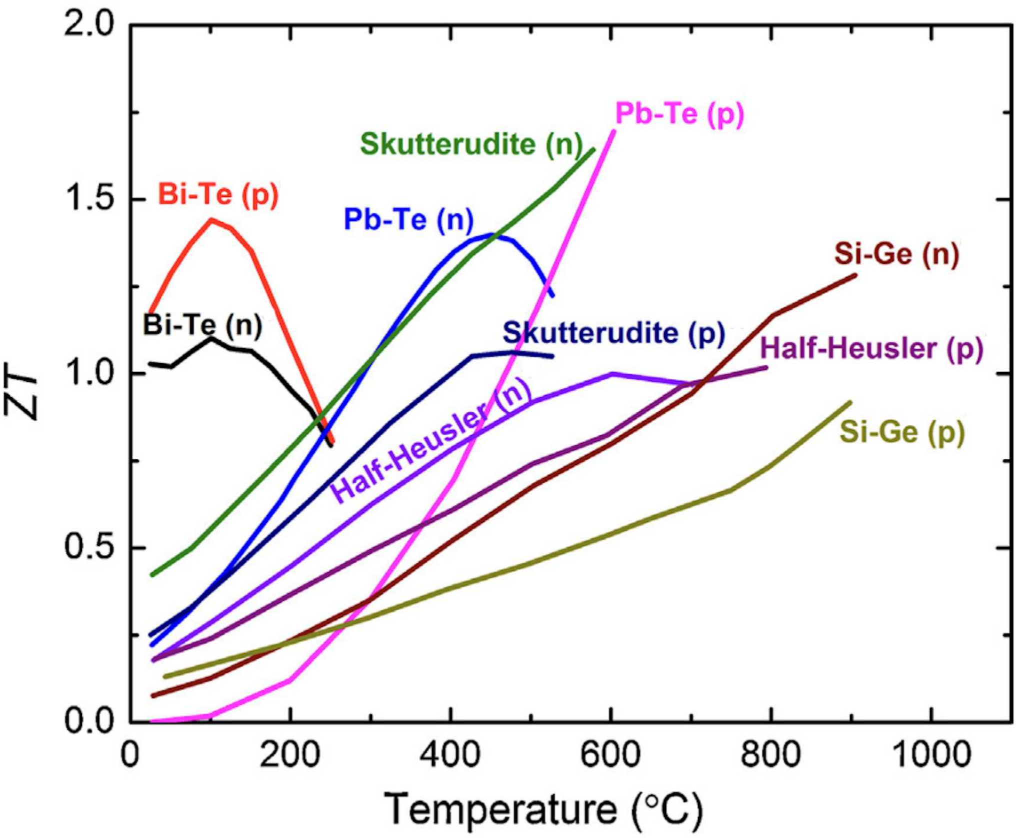

FIGURE 2.2: Overview of ZT vs temperature for different thermoelectric materials. Reprinted from [44].

Most room-temperature thermoelectric materials are based on bismuth. These materials have a very good ZT 1 at low temperatures. Adding different elements can increase their electrical conductivity or decrease their thermal conductivity, thus increasing the ZT. Common materials include bismuth telluride and BiSbTe (ZT=1.4 at 107°C)for room temperature applications [45].

As for high-temperature materials, there are many types, for example, SnSe, which has a high figure of merit (ZT=2.6 at 650°C) through its ultra-low thermal conductivity [15]. Again, many alloys of lead telluride perform well at medium to high temperatures.

Cubic $AgPb_mSbTe_{2+m}$ exhibits a high thermoelectric figure of merit material (ZT=2.2 at 527°C) [46]. PbTe-SrTe is an alloy with a high ZT at medium to high temperatures [47]. In addition to bismuth telluride, some of the other significant bulk thermoelectric materials are skutterudites (ZT=1.43 at 527°C) [48] clathrates and half-Heusler alloys (ZT=1 at 627°C) [49].

2.3 Principle of thermoelectric generator

After a brief introduction to the materials used in thermoelectric generators, it is essential to understand their working principles to optimize the generator's structure. Besides the Seebeck effect, an opposite phenomenon known as the Peltier effect was later discovered. The Peltier effect refers to the phenomenon where heat is absorbed or released at the junction of two different materials when an electric current passes through them. This temperature change depends on the direction of the current flow [50]. The heat flow generated by the Peltier effect can be expressed in terms of Eqs. 2.3 [51],

$$q = SIT \tag{2.3}$$

Analyzed the basic thermoelectric generator structure, the current can be expressed as:

$$I = \frac{\Delta V}{R} = \frac{(S_p - S_n)\Delta T}{R_{in} + R_L} = \frac{(S_p - S_n)(T_H - T_C)}{R_{in} + R_L} \tag{2.4}$$

where S_n and S_p are the n-type and p-type Seebeck coefficient, respectively and R_{in}, R_L is the internal resistance, load respectively. Therefore, the power on the load is:

$$P = I^2R = \{\frac{(S_p - S_n)(T_H - T_C)}{R_{in} + R_L}\}^2 R_L \tag{2.5}$$

The derivative of Eqs. 2.5 indicates that the maximum output power is achieved when the load resistance (R_L) is equal to the internal resistance (R_{in}) of the system. The heat flowing (q_0) from the source needs to balance some of the heat from the Peltier effect and Joule's heat, shown in Eqs. 2.6 [52]:

$$q_0 = (S_p - S_n)IT_H - \frac{1}{2}I^2R + (K_p + K_n)(T_H - T_C) \tag{2.6}$$

where K_n and K_p are the thermal conductance of n-type and p-type material, respectively. The relationship between thermal conductance and thermal conductivity, resistance and electrical conductivity are shown in Eqs. 2.7 [53], Eqs. 2.8 [54]:

$$K = \kappa\frac{A}{L} \tag{2.7}$$

$$R = \frac{L}{\sigma A} \tag{2.8}$$

Thus, by combining Eqs. 2.1, Eqs. 2.7 and Eqs. 2.8, the relationship between the device ZT and thermal conductance and resistance can be derived:

$$ZT = (S_p - S_n)^2 \frac{\frac{L}{AR_{in}}}{\frac{L(K_p+K_n)}{A}} T = \frac{(S_p - S_n)^2}{R_{in}(K_p + K_n)} T \tag{2.9}$$

For thermoelectric generators, the ZT is solely dependent on the material. Therefore, to calculate the maximum efficiency, the ratio of the load resistance to the internal resistance (R_L/R_{in}) is introduced as a parameter M. This allows us to derive an equation for efficiency concerning M. The efficiency is expressed as P/q_0. Combining Eqs. 2.5 and Eqs. 2.6, the efficiency η can be expressed as:

$$\eta = \frac{P}{q_0} = \frac{\{\frac{(S_p-S_n)(T_H-T_C)}{R_{in}+R_L}\}^2 R_L}{(S_p - S_n)IT_H - \frac{1}{2}I^2R_{in} + (K_p + K_n)(T_H - T_C)} \tag{2.10}$$

Combining Eqs. 2.9, Eqs. 2.10, and Eqs. 2.4 while setting the ratio R_L/R_{in} as M, the efficiency can be simplified to the following form:

$$\eta = \frac{M(T_H - T_C)}{T_H(1 + M) - \frac{1}{2}(T_H - T_C) + \frac{(1+M)^2}{Z}} \tag{2.11}$$

The partial derivative of Eqs is taken to determine the maximum efficiency value. 2.11 with respect to M and setting it equal to zero yields Eqs. 2.12:

$$\frac{\partial \eta}{\partial M} = 0 \tag{2.12}$$

The results are shown in Eqs 2.13:

$$M_\eta = \sqrt{1 + ZT_m} \tag{2.13}$$

where T_m is the average temperature $\frac{(T_H+T_c)}{2}$ when the efficiency reaches its peak. Substituting Eqs. 2.13 into Eqs. 2.11 gives the maximum efficiency η_{max}, shown in Eqs. 2.14 [55]:

$$\eta_{max} = \eta_c \frac{M_\eta - 1}{M_\eta + \frac{T_C}{T_H}} \tag{2.14}$$

where the Carnot efficiency η_c is given as [56],

$$\eta_c = \frac{T_H - T_C}{T_H} \tag{2.15}$$

The maximum thermoelectric conversion efficiency is constrained by the Carnot efficiency, the ZT, and the temperatures T_H (hot side) and T_C (cold side). Circuit analysis reveals that under constant temperature difference, maximum power delivery is achieved when the load resistance equals the internal resistance, i.e., $M = 1$. However, the maximum efficiency is reached at $M = M_\eta$, where $M_\eta = \sqrt{1 + ZT_m}$ is greater than

1. Additionally, according to Eqs. 2.14, the larger the ZT, the closer the maximum efficiency (η_{max}) approaches the Carnot efficiency (η_c). This trend shows the necessity of seeking materials with a higher ZT. By theoretically calculating the relevant parameters under ideal conditions, we can identify new directions, materials, and structures that could significantly improve the efficiency of thermoelectric generators. Computational modelling and simulations can further enhance this efficiency. Additionally, experimental research and development are essential to validate these findings and drive further improvements.

2.4 Architectures of thermoelectric generator

In addition to searching for materials with a higher figure of merit, optimizing the use of these materials to achieve high output power and efficiency also requires research into the devices' structures. Over the years, this research has led to the development of many different types of thermoelectric generator structures. However, generally speaking, these structures share several similarities.

2.4.1 Conventional bulk thermoelectric generator

The bulk TEG represents the most fundamental structure of a thermoelectric generator, derived directly from the primary Seebeck effect. Figure 2.3 shows the basic schematic of a single pair conventional bulk TEG. In this design, the n-type and p-type legs are parallel to ensure uniformity at the cold end plane. The top and bottom surfaces serve as the substrate. The primary function of these planes is to facilitate heat transfer while preventing electrical current leakage to other areas. Consequently, the materials chosen for these planes must have high thermal and very low electrical conductivity to fulfil these requirements effectively. The most commonly used materials for this part of thermoelectric generators are ceramics such as SiO_2 (Quartz) with κ $1.4W/(mK)$[57], Al_2O_3 (alumina) with κ $30W/(mK)$ [58], or AlN(aluminium nitride) with κ $130-270W/(mK)$ [59] at room temperature. SiO_2 is used in thermoelectric modules for structural support and insulation due to its stability at high temperatures. Al_2O_3 is often used as a substrate material and in insulation layers within TEGs to provide electrical insulation and mechanical support. AlN is used as substrates and insulators in TEGs due to its ability to efficiently dissipate heat while electrically isolating different parts of the device[60].

Beneath the top ceramic surfaces of the thermoelectric generator, copper electrodes are used to connect the n-type and p-type materials. Copper is chosen for its high electrical and thermal conductivity. The most basic shape for these connections is a cuboid. This is because cubic or rectangular prismatic shapes are simpler to manufacture compared to more complex geometries [3]. These shapes can be easily produced using standard

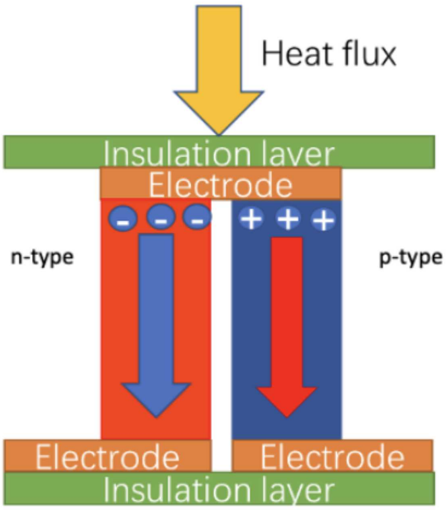

FIGURE 2.3: Schematic of a bulk TEG.

cutting, machining, and shaping techniques, making the manufacturing process more efficient and cost-effective. In addition, the cubic shape allows for a more uniform distribution of heat across the leg's cross-sectional area. This helps maintain a consistent temperature gradient, which is crucial for optimizing the thermoelectric effect. There are also copper electrodes underneath the two legs, but their function differs from those above. Instead of connecting the two legs, the electrode beneath extends outward to connect to an external circuit. This external circuit typically consists of a load resistor in a single-module setup. In the case of large-scale integration, these electrodes connect to subsequent single-pair bulk thermoelectric generators.

The bulk structure of thermoelectric generators is relatively straightforward and has several applications in the industry. For instance, automobile thermoelectric generators (ATEGs) can convert waste heat from vehicles, a common occurrence in everyday life, into electricity [61]. Although incorporating a thermoelectric generator adds weight to a car, research, such as that by F. Stablers [62] has shown that the vehicle's overall efficiency can still improve despite the added weight. In ATEGs, the hot end is connected to the engine, which generates significant heat, while the cold end is linked to the cooling fluid or directly exposed to the outside air. An optimized thermoelectric generator can maintain a temperature difference of several hundred Kelvin between the hot and cold ends, potentially achieving an output power of around 1000 W [63]. In addition to ATEGs, solar thermoelectric generators are another widely used application.

2.4.2 Segmented thermoelectric generator

Figure 2.4 illustrates the schematic of a single pair of segmented TEG. Based on the operating principle of TEGs, the temperature along the TEG legs decreases from the top to the bottom. Additionally, these materials' figure-of-merit (ZT) is temperature-dependent (TD). Therefore, in situations with a large temperature difference, neither the TEG leg's top nor bottom will exhibit an optimal ZT.

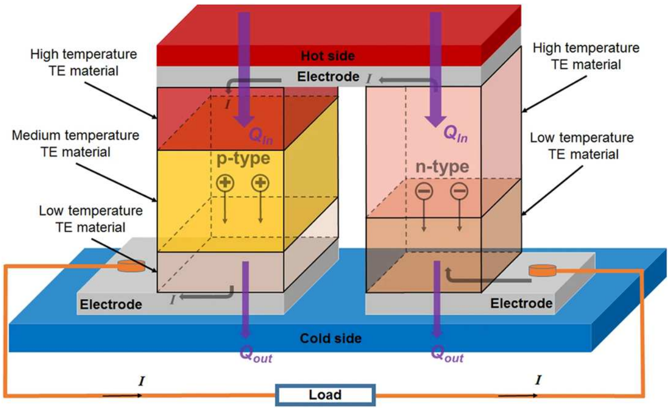

FIGURE 2.4: Schematic of segmented TEG. Reprinted from [64]

Segmented TEGs (STEGs) represent a crucial innovation to enhance efficiency when operating under significant temperature differences [65]. This approach involves combining materials that are highly efficient at high temperatures with those that are highly efficient at low temperatures. Under ideal conditions, each material operates within its most efficient temperature range, thereby improving the system's overall performance [66]. For instance, Flueiral et al. proposed a new STEG design that achieved a conversion efficiency of 15% under a temperature difference of 675K, which is 20% higher than previous designs [67]. Since ZT is a highly temperature-dependent parameter and each thermoelectric material typically performs optimally over a relatively narrow temperature range, the development of STEGs that combine two or more materials with different operating temperatures in series within the TEG legs has proven to be an effective strategy for enhancing TEG efficiency [68]. Notably, Zhang et al. demonstrated a record-high efficiency of up to 12% using segmented TEG modules composed of Bi_2Te_3-based alloys and $CoSb_3$-based filled skutterudites [69].

2.4.3 Other thermoelectric generator structures

As previously mentioned, the n-type and p-type legs in a standard bulk thermoelectric generator are typically cubic. However, recent studies have explored the idea of altering the shape of these legs, investigating various forms such as pyramidal [70], exponential [71], and quadratic [72] shapes. The non-uniform cross-section of pyramidal shapes can create a more favourable temperature gradient within the leg. This can help maintain a high temperature difference between the hot and cold junctions, which is crucial for maximizing the thermoelectric effect. For example, Figure 2.5 illustrates a flat bulk TEG with pyramidal legs [73]. The rationale behind the design of asymmetrical TEGs is to manipulate the thermoelectric resistance of the legs, thereby aiding in the control of the temperature gradient along the leg.

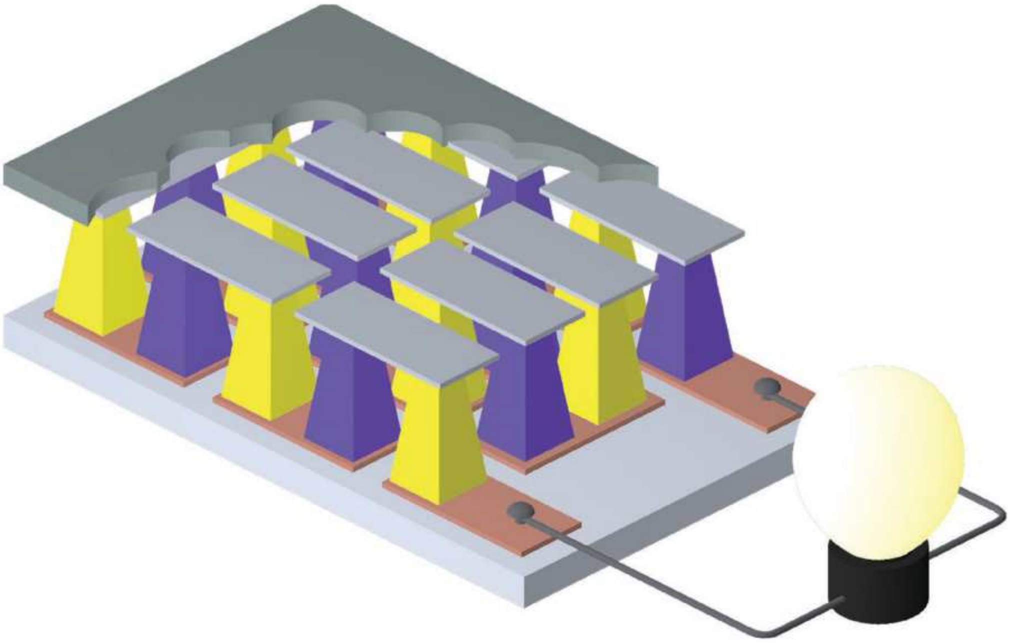

FIGURE 2.5: Flat bulk thermoelectric generator with pyramidal legs. Reprinted from [73]

Moreover, in many settings where waste heat is generated, such as in oil or steam pipelines, this heat is often dissipated through cylindrical ducts. In these scenarios, cylindrical thermoelectric generators are more suited to the environment. One design of such a generator, known as a ring TEG, is depicted in Figure 2.6 [74]. In 2015, a company utilized a similar concept to develop a cylindrical thermoelectric generator aimed at enhancing vehicle efficiency [75]. In an optimized state, this generator can produce an output of 30W in a single module.

Research in thermoelectric generators is ongoing and diverse. In addition to the widely studied bulk TEGs, developments in micro and thin-film thermoelectric generator structures are also occurring. However, this report primarily focuses on bulk TEGs, so thin-film thermoelectric generators will not be discussed in detail here.

2.5 Modelling and optimizations of thermoelectric generator

This section will address the issue of modelling TEGs and optimizing the relevant geometrical parameters and operating conditions once the structure of the TEG model

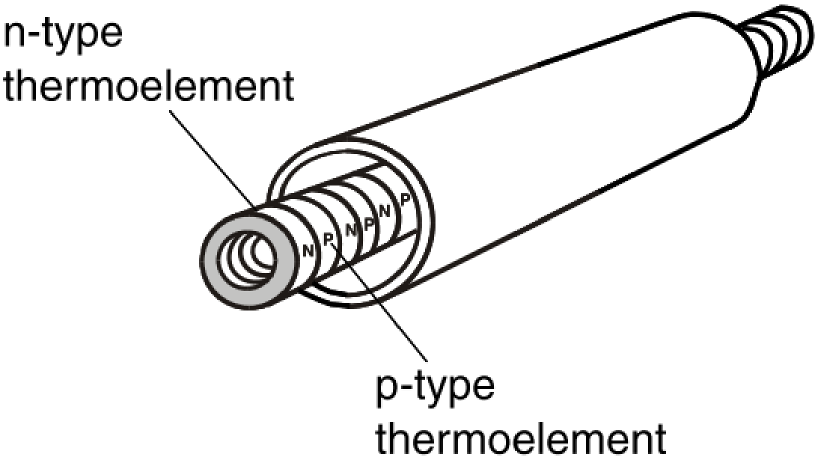

FIGURE 2.6: A thermoelectric module of the ring-structured TEG. Reprinted from [74]

has been established. It is relatively rare for TEGs to fully utilize superior thermoelectric materials. [19]. The main reason is the fact that the output power of a TEG relies not only on the performance of the TE materials but also critically on the TEG design, including its geometrical configuration, contact resistance and its coupling with heat source/sink as well as environmental working conditions, which demands careful and holistic consideration in TEG modelling and optimization [76] [19] [73] [77] [4].

The performance of any of these optimization methods is critically dependent on the coupled TEG model to identify the output of TEGs accurately and efficiently. It is particularly challenging considering the non-linear thermoelectric effects and the intricate inter-dependence of each design parameter [78][79][80]. TEG models can generally be established through theoretical and mathematical approaches. For example, an early theoretical model proposed by Min et al. [81] investigated the effect of thermoelement length on the module's coefficient of performance. Gou et al. [82] developed a theoretical system model for a low-temperature waste heat thermoelectric generator setup. Newbrook et al. [83] built a simplified theoretical model for a thin film-based TEG performance optimization. Although these theoretical models enable quick estimation of the TEG performance, the accuracy is limited by their grossly simplified thermoelectric parameters (e.g. temperature-dependent parameters) [84]. Besides the theoretical model, mathematical model-based simulation also prevails due to its superiority in solving differential equations and ease of use [78]. Suter et al. [85] implemented a heat transfer model coupling one-dimensional (1-D) conduction through the thermoelement legs to study a thermoelectric stack. A similar 1-D model was also adopted by Shen et al. [84] to analyze the TEG performance with the temperature dependence of TE materials considered. Zhu et al. also used a similar model to investigate and optimize the performance of a segmented TEG [86]. Using Figure 2.7 as an example, Zhu views the entire TEG as 1-dimensional. By default, the various properties of the material in the transverse direction are kept consistent. On this basis, the whole TEG is divided into multiple smaller pieces. When the division is sufficiently small, i.e., the Seebeck coefficient, thermal conductivity, electrical conductivity, and other parameters of this part can be defaulted to constant in this area. The relevant parameters can then be calculated using the formulae and accumulated to approximate results.

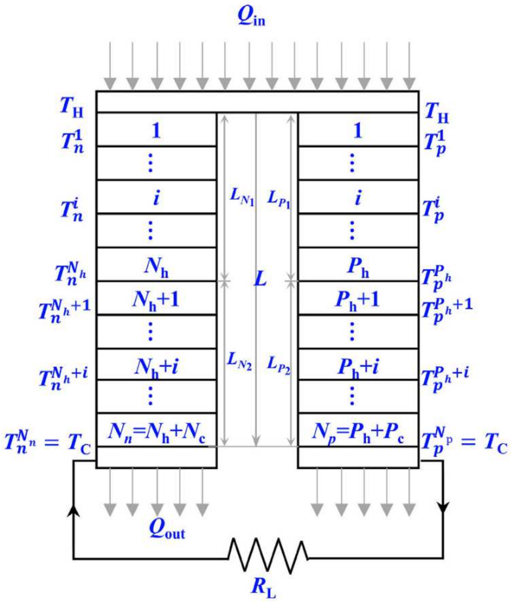

FIGURE 2.7: Schematic of the mathematical model of the TEG. Reprinted from [86]

Nonetheless, a 1-D mathematical model ignores the effects in the other two dimensions, increasing the potential for error. Three-dimensional (3-D) modelling techniques, also known as finite element analysis (FEA), are available on commercial software (e.g. COMSOL and ANSYS), which enables simultaneous incorporation of all thermoelectric factors and can provide high prediction accuracy for TEG optimization [80]. For example, a 3-D ANSYS TEG model was coupled with the multi-objective genetic algorithm (MOGA) in both works reported by Chen et al. [87][88], demonstrating outstanding agreements with experimental results. Meng et al. [89] build up a TEG model in COMSOL as the direct problem solver to facilitate the multi-objective optimization of a thermoelectric energy conversion-utilization system. The simplified conjugate-gradient method proposed by Liu et al. [90] was also coupled with a COMSOL-based TEG model. These models have superior reliability in calculating TEG power performance by allowing simultaneous coupling of nearly all related TE effects and factors. Ge et al. applied a 3-D COMSOL model in their evolutionary algorithm-based optimization of a segmented TEG [91]. However, such high accuracy for 3-D models comes at the cost of increased computation demand, prohibiting its wide adoption for TEG optimization applications.

After modelling, considering such complexity in TEG design, reliable optimization methods are preferred over the conventional analytical approach to perform optimization. A simplified conjugate-gradient method (SCGM) was proposed by Liu et al. to realize the parametric optimization for both TEG power and efficiency [90]. The widely used Taguchi method was also adopted by Chen et al. in the TEG system to find the optimum conditions for maximizing the performance [92]. He et al. introduced a Hill-climbing algorithm to achieve a maximum power output [78]. Genetic algorithm (GA), a subset of evolutionary computation in artificial intelligence (AI), has been extensively explored for application in TEG design. GA is one derivative-free optimization method that is appealing for solving optimization problems. It uses stochastic and direct-search processes to find reasonable approximate solutions to complex issues with little prior knowledge of the optimization problem. Ge et al. employed a non-dominated sorting genetic algorithm (NSGA-II) to identify the best geometric ratio for a segmented TEG [91]. Chen et al. applied the multi-objective genetic algorithm (MOGA) to determine the optimum leg length and area of thermoelectric elements based on a constant volume [87]. The same group adopted a similar algorithm to maximize the power of a segmented skutterudite TEG under different temperatures [88].

2.6 Hybrid thermoelectric generator system

Besides focusing on the thermoelectric generator, investigating its heat sources and application scenarios also represents crucial directions for research. TEGs pave the way for innovative methods of generating renewable energy and expanding sources of energy recovery. Among these, two primary TEG hybrid systems stand out: the radiative cooling-thermoelectric generator and the photovoltaic-thermoelectric generator. These systems exemplify how TEGs can be integrated with other technologies to enhance energy efficiency and harness energy from diverse sources, further broadening the scope of renewable energy applications.

2.6.1 Radiative cooling thermoelectric generator

Radiative cooling is a natural process where a surface loses heat by emitting infrared radiation [53]. All objects emit thermal radiation according to their temperature. The Earth’s atmosphere is particularly transparent to infrared radiation in the 8-13 μm wavelength range, known as the ”atmospheric window,” allowing thermal radiation to escape into space [93]. By designing materials with high emissivity in the infrared range and low absorptivity in the solar spectrum, radiative cooling can be effectively applied for various applications, offering an energy-efficient, environmentally friendly alternative to traditional cooling methods. This process can be harnessed to passively cool objects, buildings, and electronic devices without requiring external energy input [10].

Recent advances in the field have highlighted radiative cooling as a crucial technology for enhancing energy efficiency and harvesting applications. Initially, the focus of radiative cooling applications was primarily on nighttime scenarios. Several studies have achieved significant cooling effects at night by optimizing materials [94] and coatings [95] on radiative cooling surfaces. However, achieving daytime radiative cooling has been more challenging. This difficulty arises because absorption from the intense solar spectrum (0.3-3.0 µm) often quickly surpasses the cooling energy [96]. A breakthrough occurred in 2014 when Raman et al. achieved daytime radiative cooling for the first time. They developed spectrally selective filters that exhibit high emissivity within the atmospheric window while having deficient solar spectrum absorption [10]. Since this achievement, further advancements have been made in enhancing radiative cooling performance. These improvements involve the selection of specific materials [97] and the design of photonic structures [98]. These developments have enabled new applications, such as building-integrated cooling systems [99] and cooling for solar cell panels [98] [100].

Radiative cooling has been investigated to exploit its temperature difference for energy generation. And thermal energy can be converted into electricity by integrating thermoelectric generators [101][102]. The concept of radiative cooling (RC) powered TEGs has since been developed as a stable, continuous power supply for several different applications. Compared with TEG with solar absorbers [103], integrating it with a radiative cooler has more advantages in continuous power generation. For example, Ramen et al. developed an RC-TEG that can work day and night continuously, generating a power of 25 mW/m^2 [104]. Such power is sufficient for transmitting Bluetooth signals or other IoT work [105]. Zhan et al. enhanced thermoelectric output power via radiative cooling using a novel nanoporous alumina film [106]. Several studies also focused on using radiative cooling in wearable TEGs [107] and achieved a power density of 55 mW/m^2 at 293K [108]. Xia et al. developed a thin film RC-TEG that allowed 24-hour continuous power generation [109]. Mu et al. also studied thin film TEGs in combination with radiative cooling, achieving a constant average 0.18 mV output for 24 hr [110]. In addition, RC-TEG also possesses excellent potential to be implemented as wearable energy harvesting devices [111] and bright windows [112].

Several analytical studies were conducted to model and investigate the performance of RC-TEG. For example, Liu et al. have modelled the RC-TEG device mathematically and examined the effects of different radiative cooling spectra and other relevant parameters on the RC-TE device [113]. A mathematical modelling study of radiative cooling versus thermoelectric refrigerators was carried out by Liao et al. [114]. Zhao et al. also conducted mathematical modelling of the RC-TEG device, focusing on optimizing the TEG parameters [115].

A variety of parameters from both the radiative cooler and the TEG itself determines the performance of an RC-TEG. In addition, as a ubiquitous process, the power output is also highly dependent on its environmental conditions, as the atmospheric window transmittance can be affected by geographical location [116], cloud cover [117], and humidity conditions [118]. Such environmental variations can significantly impact the radiative cooling power and change the RC-TEG performance. However, despite the growing interest in this novel energy harvesting technology, a comprehensive investigation of its performance considering all parameters is lacking, to the best of our knowledge. For example, environmental parameters (e.g. convection, water vapour) should be considered when optimizing the RC-TEG. In addition, parameters in both the radiative cooler and the TEG should be optimized simultaneously [119]. Therefore, a holistic approach should be adopted concerning environmental and device parameters when investigating and optimizing the RC-TEG performance.

2.6.2 Photovoltaic thermoelectric generator

Besides radiative cooling, systems that integrate photovoltaic with thermoelectric generators have also attracted significant attention. Combining TEGs with PV panels offers a promising approach to utilizing excess heat, thereby enhancing the overall efficiency of the photovoltaic system and generating additional electrical power. Numerous studies have shown that general hybrid PV-TEG systems often achieve higher efficiency than standalone PV systems [120][121][122][123]. However, integrating these two modules increases the system's structural design and optimization complexity. Consequently, developing a robust model that enables quick and accurate simulation of the PV-TEG system's performance. Nonetheless, creating such a model presents significant challenges.

Recent scholarly investigations have proposed various models for PV-TEG systems, yet many exhibit inherent flaws, as catalogued in Table 2.1, with ρ_c contact resistivity, C_{PV} PV coating, M_{PV} PV morphology, V_{PV} the PV voltage. For instance, Bjørk et al. developed an analytical model to study the PV-TEG system with different PV materials [124]. However, this work estimates the efficiencies of both PV and TEG through an analytical approach. Apart from material variation, all parameters are held constant, constraining the model's versatility for application.

Fini et al. developed a one-dimensional (1D) PV-TEG mathematical model and verified it through experiments [125]. Similarly, Makki et al. created a one-dimensional mathematical model of a PV-TEG system with a hot pipe [126]. This model's primary variables are limited to ambient temperature, wind speed, and solar radiation, while other essential parameters for the PV and TEG models are kept constant. The limited scope of these variables indicates that the model may lack broad generalizability. Babu

TABLE 2.1: PV-TEG modelling method literature review.

Research	PV model	TEG model	T-D property	ρ_c	C_{PV}, M_{PV}	V_{PV}
[124]	mathematical model	mathematical model	No	No	No	No
[125]	mathematical model	3D FEA	No	Yes	No	No
[126]	mathematical model	mathematical model	No	Yes	No	No
[127]	mathematical model	mathematical model	No	Yes	No	No
[128]	mathematical model	mathematical model	No	Yes	No	No
[129]	mathematical model	mathematical model	No	No	No	No
[130]	mathematical model	3D FEA	Yes	No	No	No
[131]	mathematical model	3D FEA	Yes	No	No	No
[132]	mathematical model	mathematical model	No	No	No	No
[133]	mathematical model	mathematical model	No	No	No	No
[134]	mathematical model	mathematical model	No	Yes	No	No
[135]	mathematical model	mathematical model	Yes	Yes	No	No
[136]	mathematical model	3D FEA	Yes	No	No	No
[137]	mathematical model	3D FEA	No	No	No	No

et al. developed a one-dimensional PV-TEG mathematical model to analyze the system's performance with different PV materials and environmental parameters, achieving an overall improvement of about 6% [127]. Gu et al. developed a one-dimensional mathematical model to analyze the PV-TEG system, gaining an efficiency improvement of 1.24% to 2.85% relative to the PV system alone [128]. Since these models are inherently one-dimensional, neglecting parameters in the other two dimensions compromises both the model's accuracy and comprehensive applicability.

Motiei et al. further investigated the thickness and melting point of phase change materials (PCM) by performing a two-dimensional modelling of the PV-TEG model [129]. This model includes ambient air temperature, wind speed, heat loss and convection, focusing on the impact of different PCMs. In addition, most PV-TEG models adopt a simple equation to estimate PV efficiency [138] while using constant values for the thermoelectric material properties. These simplifications inevitably diminish the accuracy of their respective models. Shittu et al. evaluated the efficiency of the PV-TEG system, both with and without a flat plate heat pipe. Their analysis was underpinned by constructing a 1D mathematical model complemented by a 3D finite element analysis model, specifically utilizing COMSOL [129] [131]. Employing temperature-dependent material parameters in their TEG COMSOL model enhances its precision. While 3D FEA modelling for both yields more precise results, its simulation speed is significantly slower than mathematical modelling. Therefore, a modelling tool that combines the accuracy of 3D finite element analysis with the efficiency of mathematical modelling is essential.

Shittu et al. evaluated the efficiency of the PV-TEG system, both with and without a flat plate heat pipe, using a 1-D mathematical model and a 3-D finite element analysis model in COMSOL [130]. Their use of temperature-dependent material parameters in the COMSOL model for TEG enhances its precision. Nonetheless, the omission of contact thermal and electrical contact resistance in their model may introduce limitations.

Regarding the PV efficiency, most models adopt a simple equation of 2.16 [138],

$$\eta_{PV} = \eta_{ref}[1 - \beta(T_c - T_{ref})] \tag{2.16}$$

η_{PV} is the PV efficiency, and β is the temperature coefficient. Tc is the average temperature of the silicon layer, and T_{ref} is the reference temperature of 298.15K. η_{ref} is the reference efficiency of the polycrystalline silicon solar cell at T_{ref}. This equation results in potentially less accurate outcomes than those calculated through a 3D finite element analysis (FEA) model. While 3D FEA modelling yields more precise results, its simulation speed is significantly slower than mathematical modelling. Therefore, a modelling tool that combines the accuracy of 3D finite element analysis with the efficiency of mathematical modelling is essential.

2.7 Machine learning technology

Machine learning, a core artificial intelligence component, involves studying how computers can simulate or implement human learning behaviour to acquire new knowledge or skills. It focuses on the continuous reorganization and improvement of existing knowledge structures. Machine learning has a long history, dating back centuries. Key developments such as Bayes' theorem, Laplace's derivation of least squares, and Markov chains in the 17th century laid the groundwork for its widespread application. Research approaches and objectives have evolved since the formal study of machine learning began in the 1950s. Initially concentrating on system execution, the field expanded to include concepts like neurons, producing more tangible results. Traditional research directions in machine learning have encompassed decision trees, random forests, artificial neural networks, and Bayesian learning [139].

Bayesian learning represents one of the early research directions in machine learning. This approach is rooted in a specific case of Bayes' theorem, which was proved by the British mathematician Thomas Bayes in 1763. Through the collective efforts of numerous statisticians, Bayesian statistics were gradually established as a fundamental component of the field after the 1950s [140].

Random Forest (RF), a pivotal algorithm in machine learning, is a method that employs multiple tree classifiers for classification and prediction tasks [141]. Recent research on random forest algorithms has seen rapid development, with applications spanning diverse fields such as bioinformatics, ecology, medicine, genetics, remote sensing geography, and applied research [142]. In this thesis, Machine learning only focuses on artificial neural networks and genetic algorithms.

2.7.1 Artificial neural networks

Artificial neural networks (ANNs) are algorithms known for their non-linear adaptive information processing capabilities [143]. ANN is a general-purpose neural network with fully connected layers, suitable for a variety of tasks and data types. They can overcome the limitations of traditional artificial intelligence methods, particularly in areas such as pattern and speech recognition and in processing unstructured information. The concept of artificial neural networks has been around since the 1940s and has seen rapid development. Convolution Neural Networks (CNNs) include convolutional layers that apply convolutional operations to the input data, which helps in capturing spatial hierarchies in images. Therefore CNN are the most commonly used in computer vision and image recognition applications [144].

In recent years, with the advent of concepts like cloud computing and big data, coupled with further improvements in computer performance, data collection has significantly increased. This abundance of data is instrumental in aiding machine learning, dramatically improving its success rate. An artificial neural network is a complex network of interconnected neurons where each unit processes numerical input and output. Before it becomes operational, the network must undergo a learning process based on specific criteria. One of the key strengths of this method is its ability to learn from errors, reducing the likelihood of repeating the same mistakes. This approach is characterized by solid generalization and non-linear mapping capabilities, making it suitable for modelling systems with limited information. From a functional simulation perspective, artificial neural networks exhibit parallelism, enabling them to transfer data at extremely high speeds.

Artificial neural networks (ANNs) can be categorized into two main types: classification networks and regression networks, each with distinct operational characteristics. Regression ANNs, known for their powerful fitting ability, have been utilized in the energy sector for modelling energy consumption, forecasting energy demand [31][32], and predicting electricity consumption [33]. Another example is convolutional neural networks (CNNs), which employ convolutional calculations between layers and are commonly used in image and speech recognition.

ANN technology has been increasingly utilized in energy sectors to analyze and control the energy consumption in buildings [145] and motor drive applications [146]. More recently, ANN has been adopted to facilitate the modelling and design of renewable energy technologies with high fidelity [147] [148]. For example, Rodriguez et al. predicted solar energy generation through ANN [149]. Wang et al. applied an ANN model to model the phase-altering thermoelectric materials-based TEG system [150].

The neuron is the most fundamental component of a neural network, as illustrated in Figure 2.8. In its simplest form, a neuron receives two inputs (X_1, X_2), each multiplied by a corresponding weight (w_1, w_2). A bias is then added to this weighted sum, passing the result through an activation function to produce the output (O_1). Figure 2.8 can also

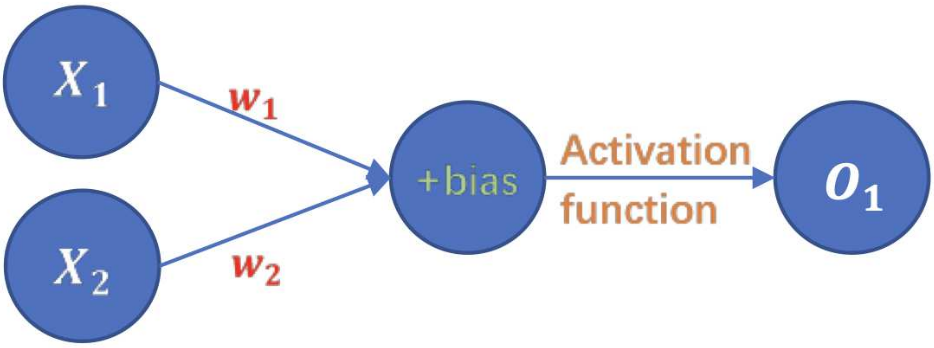

FIGURE 2.8: The structure of a neuron in an artificial neural network.

be represented by Eqs. 2.17 [151],

$$O_1 = f(W^T X + b) \tag{2.17}$$

where W denotes the vector of weights, X is the vector of inputs, and b is the bias. A fully connected neural network is formed by connecting multiple neurons to link each neuron to all the neurons in the preceding and succeeding layers. Figure 2.9 shows a simple structure of an ANN.

In addition to weights and biases, a neuron requires an activation function. Two common activation functions are ReLU (Rectified Linear Unit) and Sigmoid. The plot of two activation function are shown in Figure 2.10

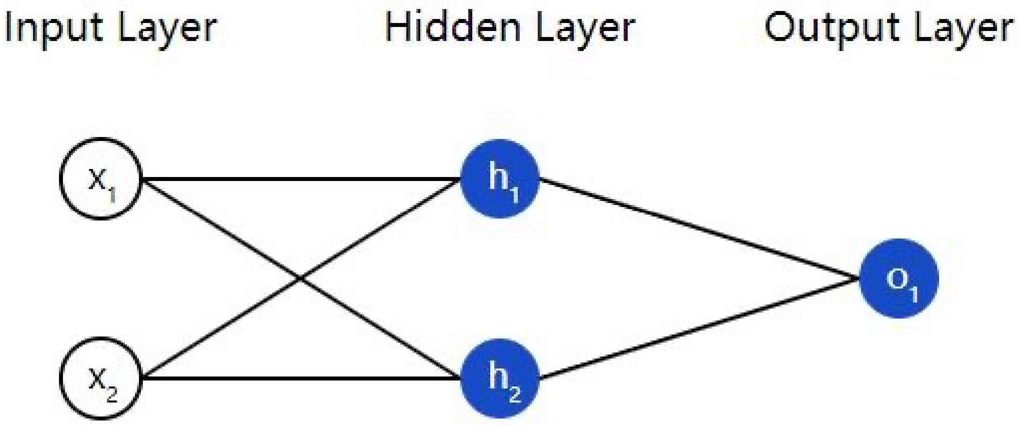

FIGURE 2.9: The schematic of ANN structure.

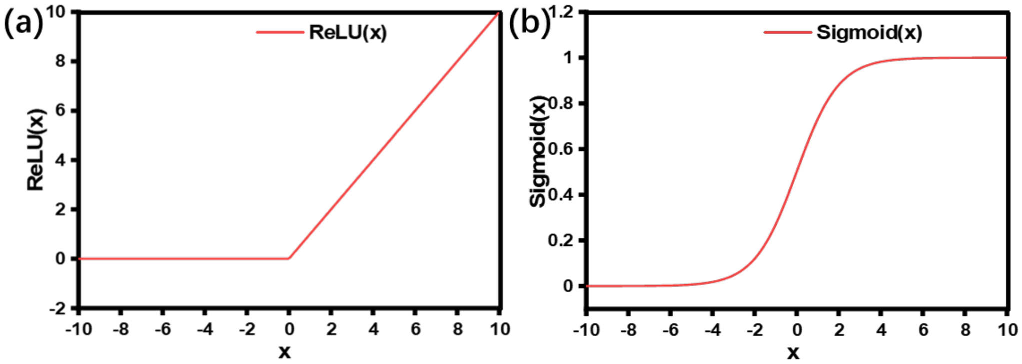

FIGURE 2.10: The plot of (a) ReLU and (b) Sigmoid activation function.

The ReLU function converts values less than 0 to 0, while values greater than 0 remain unchanged, as shown in Eqs. 2.18 [152]:

$$ReLU(x) = max(x, 0) \tag{2.18}$$

The ReLU function simplifies calculations in regression neural networks, especially during partial derivative computations. This is because the derivative of the ReLU function becomes one for positive input values, thereby streamlining the calculation process. The Sigmoid function is shown in Eqs. 2.19 [153],

$$Sigmoid(x) = \frac{1}{1 + e^{-x}} \tag{2.19}$$

The Sigmoid function is characterized by its ability to map values from the entire domain of real numbers to a range between 0 and 1. This feature is highly effective for classification neural networks, which aim to categorize data into a limited number of classes. The data compression into the [0, 1] range can effectively represent the probability of occurrence in a given category, making the Sigmoid function a popular choice for classification tasks.

The next step involves determining the neurons' basic parameters and adjusting the weights and biases to enable the neural network to fit the results as accurately as possible. This process necessitates the use of loss functions and gradient descent.

The loss function, dependent on the weights, guides the optimization process in a neural network. By taking the partial derivative of the loss function concerning these weights, we can determine the direction in which to adjust the weights and biases in the subsequent step. A typical loss function is the mean squared error, as shown in Eqs. 2.20 [154],

$$l^{(i)}(W, b) = \frac{1}{2}(\widehat{O}^{(i)} - O^{(i)})^2 \tag{2.20}$$

where $l^{(i)}$ denotes the loss function of the i^{th} neuron, $\widehat{O}$ denotes the predicted output value, and O represents the actual output value.

The partial derivative of Eqs. 2.20 indicates how the weights or biases should be adjusted. However, knowing the direction of adjustment is insufficient; the step size, or learning rate, must also be determined. New weights and biases are calculated by subtracting the partial derivative of the loss function from the current weights. This process of updating weights and biases to minimize the loss function is known as gradient descent. The weights and biases are updated in each iteration or epoch to bring the predictions closer to the actual results. After undergoing sufficient epochs, the loss function will typically oscillate around a small value. This behaviour indicates that the neural network has reached a local minimum in its optimization process. It generally is a local minimum rather than a global minimum, as finding the global minimum directly through gradient descent is challenging. Optimizing the neural network is to find the most favourable local minimum. The entire process, from the initial gradient descent to finding the minimum value, constitutes the training phase of a neural network. All adjustments to the weights and biases are computed automatically, which epitomizes machine learning.

Each neuron in a complex neural network represents a parameter. Theoretically, with enough parameters, it is possible to fit any function. However, in practice, too complex networks can suffer from overfitting. Overfitting occurs when the neural network is trained to fit the training dataset perfectly but performs poorly on data outside this dataset. This situation is undesirable and should be avoided. Additionally, it is essential to recognize that neural networks with more superficial structures can be prone to underfitting, where the model is too simplistic to capture the underlying patterns in the data effectively.

2.7.2 Iterative training process

As a data-driven approach, the effectiveness of an Artificial Neural Network (ANN) heavily depends on both the quantity and quality of its training dataset, which is traditionally generated through a randomized procedure. During the training process, the network learns by interpolating to fill gaps in the training data. However, this interpolation might not be adequate if the training data contains sharp features or if the network is designed to model specific features [24]. To address this, introducing a new generation of ANNs tailored to a specific dataset can theoretically bias the network towards the accuracy of that particular dataset. This approach, known as iterative training, can be conducted in one or more rounds to enhance accuracy for a specific dataset.

In this thesis, we are especially interested in TEG designs that yield high-power performance. However, these high-performance instances might constitute only a tiny fraction of the overall training dataset in a more complex model, such as a segmented TEG model. If the training data lacks sufficient high-performance instances, the ANN's accuracy for such cases could be compromised. Therefore, through iterative training and optimization of network parameters via gradient descent [155], the ANN model can effectively learn the non-linear relationships between TEG inputs (such as geometrical parameters and operating conditions) and its power performance (including power density and efficiency) within the dataset parameter space.

Nonetheless, it's important to note that a large dataset, particularly one generated by mathematical simulations like Finite Element Analysis (FEA), demands significant computational resources. This requirement can challenge the practical application of ANNs in such scenarios.

2.7.3 Genetic algorithm

A Genetic Algorithm (GA) is a computational approach that mimics the mechanisms of natural selection and genetic processes found in Darwinian biological evolution [156]. It searches for optimal solutions by emulating these natural evolutionary processes. A distinctive feature of GA is its ability to operate directly on structural objects without requiring differentiation and continuity of functions. This characteristic endows genetic algorithms with parallelism and enhanced capabilities for global optimization. Additionally, GA employs a probabilistic approach to optimization, automatically exploring and guiding the search within an optimized space without predefined rules and adaptively adjusting the search direction as needed.

Genetic algorithms consider the entire population of individuals, and randomization techniques are used to search the encoded parameter space efficiently. The core genetic operations in GA are selection, crossover, and mutation. It is important to note that genetic algorithms do not guarantee the optimal result; they often converge to local minima rather than global minima. Figure 2.11 shows the basic schematic of the genetic algorithm [157].

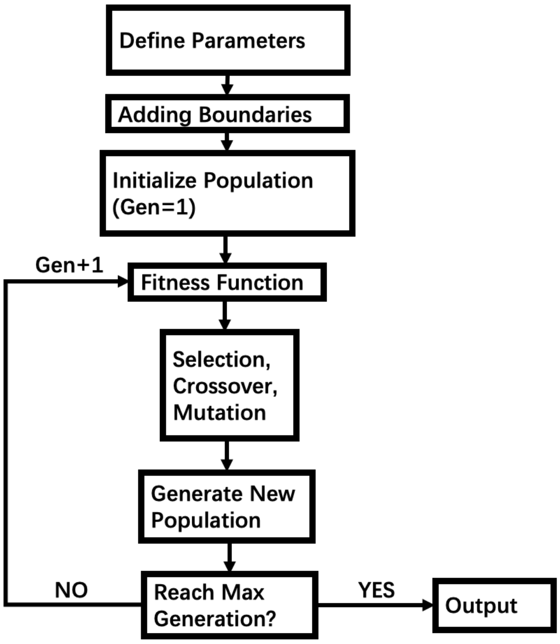

FIGURE 2.11: The flow chart of genetic algorithm.

Genetic algorithms primarily focus on evaluating populations, including potential solution sets. These solution sets are typically identified as maximum or minimum values. Within these populations, each individual is represented by a genetic code analogous to a genome in biological terms, also known as a chromosome. To simulate genetic coding as it occurs in biology, a common approach is to represent individuals using binary codes. This representation is achieved by translating the characteristics of each individual into a binary format through coding.

However, there are various encoding methods, and the choice of encoding can significantly influence the effectiveness of genetic algorithms. Once the coding process is complete, the initial population undergoes evolution based on a meritocratic approach. This involves selecting individuals according to their fitness levels and then applying combinations of crossover and mutation to generate new generations. These evolutionary processes enable the population to evolve and potentially improve over time. The following paragraphs will provide a concise overview of each step involved in the genetic algorithm process.

Several standard encoding methods are commonly used in genetic algorithms, including binary, floating-point, and symbolic encoding. Binary encoding, the simplest method, involves converting decimal numbers into binary format. Its advantages include simplicity in encoding and decoding, ease of understanding, and adherence to the principle of minimum character encoding. However, binary encoding has a notable disadvantage: the exponential growth in the weight of each binary bit can lead to discontinuities near the optimal solution, potentially causing significant deviations and inconsistent results.

On the other hand, floating-point encoding represents each gene value of an individual as a floating-point number within a specified range. This method is more complex than binary encoding but is better suited for genetic algorithms that require high precision.

Symbolic coding is a method where the gene values in an individual's chromosome are represented by symbols from a set, such as A, B, C, which do not have numerical meanings. This encoding type is used when the gene values are categorical or symbolic rather than numerical.

Several standard selection methods are used in genetic algorithms to choose specific individuals from a parent population, typically based on their fitness levels [158]. Individuals with higher fitness are more likely to be selected and passed on to the next generation. The selection method essentially translates the results of the fitness function into selection probabilities. Some typical selection methods include:

1. **Roulette Wheel Selection**: This is a probabilistic sampling method where the chance of an individual being selected for the next generation is proportional to its fitness relative to the total fitness of the population. However, this method can introduce significant errors due to the possibility of not choosing the large fitness functions.
2. **Stochastic Tournament Selection**: In this method, pairs of individuals are chosen randomly and 'compete' based on their fitness. The individual with higher fitness is selected, and this process continues until the desired population size is reached.
3. **Remainder Stochastic Sampling with Replacement**: In this method, individuals with above-average fitness are more likely to be passed on to the next generation, resulting in fewer selection errors.
4. **Optimal Individual Conserving Method**: The individual with the highest fitness in the current population is preserved and does not undergo crossover and mutation. Instead, it replaces the individual with the lowest fitness in the population after these operations.

Crossover is an essential step in genetic algorithms to generate new individuals after the selection process [158]. Common crossover methods for binary or floating-point codes include one-point crossovers, two-point crossovers, uniform crossovers, and arithmetic crossovers.

1. **One-point Crossover**: This method involves setting a single random point in an individual's coding string. Subsequently, parts of the chromosomes from two paired individuals are exchanged at this point.
2. **Two-point Crossover**: Similar to the one-point crossover, but with two random crossover points set in the coding string. A segment of genes between these points is then exchanged between two individuals.
3. **Uniform Crossover**: In this method, the coded genes are exchanged between two paired individuals at each gene position, with an equal possibility of crossover. This results in the creation of two new individuals.
4. **Arithmetic Crossover**: This involves a linear combination of two individuals to produce two new unique individuals. It is typically applied to individuals represented by floating-point codes.

Each of these crossover methods has its advantages and is selected based on the specific requirements and objectives of the genetic algorithm.

After new populations are formed through crossover, mutation is necessary to introduce genetic variation, similar to what occurs in nature [158]. In genetic algorithms, mutation involves altering the value of a gene at a specific locus in an individual's chromosomal coding string, resulting in a new individual. Standard mutation methods for binary and floating-point encoding include Simple Mutation, Uniform Mutation, and Boundary Mutation:

1. **Simple Mutation**: This involves mutating a gene value at a randomly chosen locus in an individual's coding string with a certain probability of variation.
2. **Uniform Mutation**: This method replaces the original gene values at each locus in an individual's coding string with a random number within a uniform distribution range, albeit with a small probability. It is beneficial in the early stages of an algorithm.
3. **Boundary Mutation**: This mutation randomly substitutes one of the two boundary gene values at a locus for the original gene value. It is especially effective for problems where the optimal solution is likely at or near the boundary of the feasible solution space.

2.8 Conclusion

This Chapter provided a comprehensive overview of the principles, materials, and structures relevant to thermoelectric generators. A detailed review of conventional and segmented TEG architectures was presented. The chapter also explored the challenges and limitations of current TEG modelling approaches, including theoretical models, one-dimensional mathematical models, and three-dimensional finite element analysis. In addition, hybrid TEG systems, such as those combined with radiative cooling and photovoltaic technologies, were introduced for their potential to enhance energy harvesting capabilities. Then, the application of artificial neural networks in TEG design and optimization was introduced as a novel approach to address the limitations of traditional modelling methods. Overall, this chapter established a solid foundation for the subsequent exploration of ANN-enabled TEG modelling and optimization.

Chapter 3

Methodology

This chapter will outline the methodologies employed in this thesis, including COMSOL simulations, ANN training, and the implementation of a genetic algorithm. The COMSOL section will discuss the basic simulation process for TEGs. The COMSOL model serves as the baseline in this project, and the exploration focuses on how an ANN can be used as an alternative to the COMSOL model. For the ANN segment, the focus will be on the dataset preparation process and the neural network configuration. Finally, the section on genetic algorithms will explore the specific settings of hyperparameters for two different TEG scenarios.

3.1 COMSOL simulation

COMSOL Multiphysics@ is a commercial simulation software that has become increasingly valuable as computers grow more powerful. It enables the integration and calculation of complex physical quantities that are challenging to compute manually. This software was selected for its robustness and accuracy in calculating parameters associated with the TEG model[159]. In the TEG COMSOL modelling, the relevant physics, Heat Transfer in Solids, Electric Currents, and Electrical Circuits are selected.

In COMSOL, a thermoelectric generator (TEG) model is assembled using various geometric components. These include the ceramic layer on top, the electrodes connecting the legs, the thermoelectric material, and the symmetrical connecting and ceramic layers at the bottom. Figure 3.1 illustrates the basic structure of the TEG model in COMSOL. When constructing the TEG model, it is necessary to define the geometric parameters of each component. These parameters are often represented by variables, allowing for easy modification in subsequent simulations. Additionally, to make the simulation more representative of real-world conditions, factors such as the convection

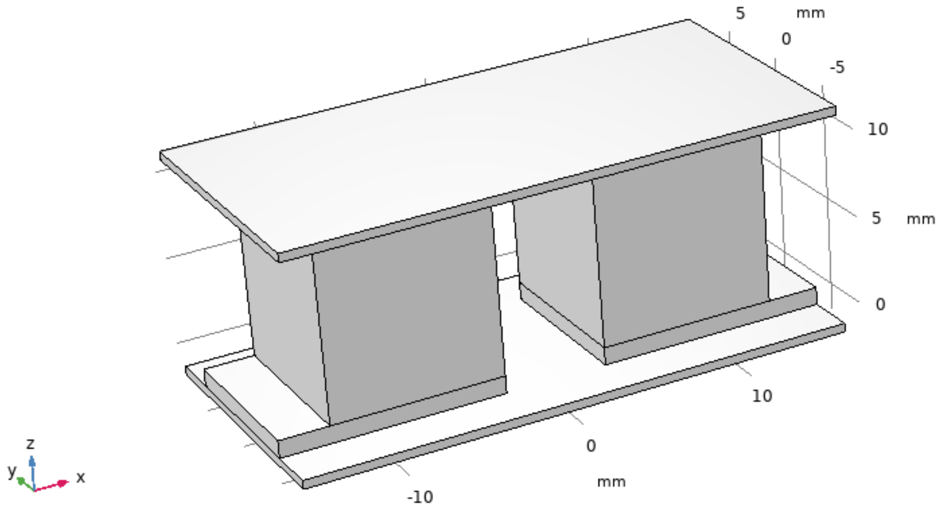

FIGURE 3.1: COMSOL simulation model

effect and the contact resistance between materials must be accurately configured in COMSOL.

The COMSOL simulation aims to calculate maximum power density (PD_{max}) and efficiency (η). The input parameters are Q_{in} and T_H. These represent two input scenarios: a constant heat flux density and a constant temperature. These two input parameters result in inconsistent output parameters. At a constant heat flow density for the input parameter, the efficiency equation is as Eqs. 3.1,

$$\eta = \frac{PD_{max}}{Q_{in}} \tag{3.1}$$

where Q_{in} is the input heat flux. Since Q_{in} is a known input parameter, the efficiency can be directly calculated from the maximum power density (PD_{max}). Therefore, when the heat flux is used as the input, the output is characterized solely by the maximum power density. Furthermore, when the temperature (T_H) is used as the input parameter and the value of heat flux density is unknown, the outputs will simultaneously include both efficiency and maximum power density.

Since the output value of interest is the maximum power density, scanning through different load resistance values during the simulation to identify the resistance at which this maximum value occurs is necessary. The process begins with an initial estimation of the approximate range of resistance derived from the resistance of the n-type and p-type materials. Subsequently, the total internal resistance is calculated based on the geometric parameters used in the modelling, as outlined in Eqs. 3.2,

$$R_{cal} = R_N + R_P + R_{IC} + R_C \tag{3.2}$$

where R_{cal} is the estimated internal resistance. R_N and R_P are the resistances of the n-type and p-type legs, respectively, R_{IC} is the resistance of the electrodes, and R_C is the contact resistance. The maximum output power density is achieved when the load resistance equals the internal resistance. However, in COMSOL models with complex parameters, the resistance of the material varies with temperature. This means the internal resistance changes at different temperatures, making it difficult to directly estimate the internal resistance to ensure the load matches it exactly. Therefore, theoretically, the load resistance value corresponding to the maximum output power density should be close to the estimated value of R_{cal}. By scanning the load resistance as per Eqs. 3.3, it is possible to determine the location of this maximum value approximately.

$$R_L = R_{cal} \times 10^{range(log_{10}0.01,\frac{1}{2},log_{10}100)} \tag{3.3}$$

3.2 COMSOL model validation using theoretical model

Once the COMSOL model of the thermoelectric generator is built, a crucial step is to verify its validity. This is achieved by constructing a theoretical model of the thermoelectric generator and ensuring that the COMSOL model produces consistent results when the same parameters are applied. Since the theoretical model is very difficult to calculate temperature-dependent material parameters, fixed parameter materials were used to maintain consistency in the COMSOL model. However, in subsequent projects, temperature-dependent materials were employed in the COMSOL model.

The structure of the TEG model, as shown in Figure 3.1, includes specific geometric parameters: the n-type and p-type materials are each set to a width and height of 10 mm, the upper and lower ceramics have an area of 500 mm^2, the ceramics have a thickness of 0.5 mm, and the electrodes are 1 mm thick.

To concentrate on verifying the parameters of the thermoelectric material section, the thermal resistance and electrical conductance in the ceramic, as well as the thermal resistance and electrical resistance in the electrode, were ignored. Given that the theoretical model is primarily designed to calculate parameters at constant temperatures, the Seebeck coefficients, thermal conductivities, and electrical conductivities of the thermoelectric materials are set to fixed values to accommodate all temperature variations. The single TE material parameters are $S_n = -0.000375V/K$, $S_p = 0.000375V/K, \sigma_n = \sigma_p = 10^5 S/m, k_n = k_p = 1W/(mK)$. Cold-side temperature (T_C) is fixed at 300K. Contact resistance is ignored in the validation.

In thermoelectric generators, three heat sources are present on both the hot and cold sides: Peltier heat, Joule heat, and heat conduction. Therefore, the power for the hot

(Q_H) and cold (Q_C) surfaces can be respectively expressed as follows:

$$Q_H = SIT_H - \frac{1}{2}I^2R_i + K(T_H - T_C) \tag{3.4}$$

$$Q_C = SIT_C + \frac{1}{2}I^2R_i + K(T_H - T_C) \tag{3.5}$$

Where I is the current, R_i is the inner resistance, and T_H and T_C are the hot-side and cold-side temperatures, respectively. Consider the load resistance of the TEG as R_L and the output power of the TEG as P. Consequently, the expression for P can be formulated as follows:

$$P = I^2R_L \tag{3.6}$$

According to the law of energy conservation, P can also be expressed as:

$$P = Q_H - Q_C \tag{3.7}$$

By integrating Eqs. 3.6 and Eqs. 3.7, we can derive an expression for the current (I):

$$I = \frac{S(T_H - T_C)}{R_i + R_L} \tag{3.8}$$

Therefore, the output power is expressed as:

$$P = \frac{S^2(T_H - T_C)^2R_L}{(R_i + R_L)^2} \tag{3.9}$$

At the constant temperature condition, Eqs. 3.9 can directly calculate the power of TEG.

When the heat flux is constant, T_H is a variable. At this point Q_H is known and Eqs. 3.4 represents the relation between T_H and I. Additionally, combining Eqs. 3.6 and Eqs. 3.7 results in Eqs. 3.10, which is another equation for T_H and I. R_L is a parameter that can be given and is therefore considered fixed.

$$I^2R_L = Q_H - (SIT_C + \frac{1}{2}I^2R_i + K(T_H - T_C)) \tag{3.10}$$

Joining Eqs. 3.4 and 3.10 and substituting T_H yields a system of quadratic equations about I.

As an example, the solution is provided when the load resistance R_L is equal to 0.002 Ω, simplifying the calculation by using specific parameters. Bringing in the specific parameters gives $S = S_p - S_n = 7.5e^{-4}V/K$, $R_i = 0.002\Omega$, $K = K_p + K_n = 0.02W/K$. When $Q_H = 10W$, substituting the above parameters, Eqs. 3.4 becomes:

$$16 = 7.5e^{-4}IT_H - 1e^{-3}I^2 + 2e^{-2}T_H \tag{3.11}$$

And the Eqs. 3.10 becomes:

$$2e^{-3}I^2 = 16 - 0.225I - e^{-3}I^2 - 2e^{-2}T_H \tag{3.12}$$

Joining Eqs. 3.11 and 3.12 by replacing the T_H, the results are

$$1.125e^{-4}I^2 + 12.4375e^{-3}I - 0.375 = 0 \tag{3.13}$$

Solving Eqs. 3.13, eliminating the negative value, the result is $I = 24.653A$. Using Eqs. 3.6, the power is calculated as $P = 1.2155W$, which is very close to the COMSOL result of 1.216W.

The outcomes of both the theoretical and COMSOL models under the specified conditions are depicted in Figure 3.2. In the first case, when the hot-side temperature (T_H) is 450K, the power corresponding to this condition can be calculated from the load resistance, as demonstrated in Eqs. 3.9 and illustrated in Figure 3.2a. When the input heat flux (Q_H) is 10W, the hot-side temperature (T_H) is initially calculated using Eqs. 3.4. Subsequently, this value of T_H is incorporated into Eqs. 3.9 to determine the power at this point, as depicted in Figure 3.2b.

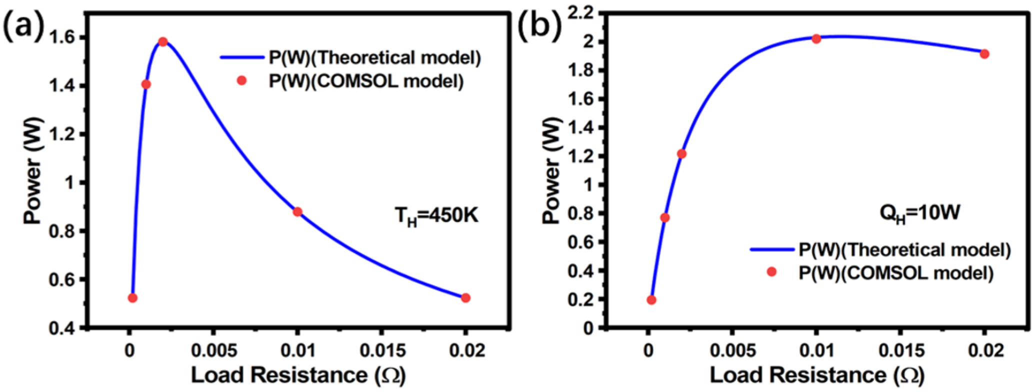

FIGURE 3.2: COMSOL simulation model validation via theoretical model

The results reveal that the COMSOL simulation closely aligns with the theoretical model, demonstrating the effectiveness of the COMSOL modelling approach. However, the theoretical model has certain limitations due to its fewer parameters. It does not account for factors such as the temperature-dependent Seebeck coefficient and neglects contact resistance. Consequently, in this thesis, we utilize a more comprehensive COMSOL model and build an artificial neural network model based on it for greater accuracy. For the more complex COMSOL model, it is currently difficult to verify its validity, and experimentation is necessary for accurate validation. However, the focus of this project is to compare the results between the ANN and COMSOL. The validation of the complex COMSOL model will be addressed in future research.

3.3 Artificial neural networks

All work using the ANN has been written using the Python-based PyTorch module. The code can be found in the appendix. All the training datasets are generated from the COMSOL model. Thousands of random input parameter sets are generated and imported into the COMSOL model to obtain the desired output values. These corresponding input and output parameters are then combined to create the final desired dataset.

Before the training process, it is essential to normalize the generated data. The primary goal of normalization is to ensure that each set of inputs has an equivalent impact on the output. This normalization process should be based on the distribution of the datasets, which typically fall into two main categories: uniform distribution and normal distribution. Therefore, the initial step before normalizing the dataset is ascertaining the input and output distribution type.

For the ANN, the input data are uniformly distributed. This uniformity arises because the data is generated in an averaged manner during the dataset creation process. On the other hand, the output data in this thesis follow a normal or log-normal distribution. Given that most of the input parameters are uniformly distributed, normalization was carried out using the following equations [160]:

$$I' = \frac{I - min(I)}{max(I) - min(I)} \tag{3.14}$$

I' is the normalized value, and I is the original input data. This normalization allows all input data to be between [0, 1]. Similarly, normalization was also performed on the output data to ensure the weights of back propagation were the same as the two outputs. However, as the output data have a relatively large range, the logarithmic scale was adopted for normalization. Eqs 3.15, therefore, performed the normalization of these data [160]:

$$O' = \frac{ln(O) - M}{SD} \tag{3.15}$$

in which O' and O are the normalized and original output values, respectively. M is the mean value, and SD is the standard deviation. The normalization process for data that follows a normal distribution involves omitting the logarithmic calculation from the Eqs. 3.15. More details of normalization can be found in the Appendix code.

After completing the normalization process, the next step involves determining the relevant training hyperparameters, as listed in Table 3.1. The 'Epochs' refers to the number of times the entire dataset undergoes training, while the 'Batch size' is the smallest unit of data processed during training. After processing each batch, gradient descent is performed to update the weights and biases. A standard batch size of 64 was chosen.

The activation function selected is the commonly used ReLU (Rectified Linear Unit), and the loss function is Mean Square Error (MSE). For the optimizer in ANN training, the Adam algorithm was chosen [161]. Adam maintains two moving averages: the mean (first moment) and the uncentered variance (second moment) of the gradients. The parameters are updated using these moving averages, which helps to stabilize the training process. The learning rate, which determines the step size for each training iteration, is a critical parameter. A minimal learning rate can lead to more accurate minima detection but may also result in convergence to local minima. Conversely, a more significant learning rate can avoid many local minima but might cause oscillations around the minima. This thesis employed a learning rate of 0.001, which is normally used in ANN training [161]. The two subsequent reductions at epochs 1800 and 1900, which is called the StepLR, ensure that the final trained network closely approaches the minimum value.

TABLE 3.1: List of hyperparameters for artificial neuron network training

Hyperparameters	**Values**
Epochs	2000
Batch size	64
Activation function	ReLU
Initialization method	Weight: Kaiming uniform; bias: zeros
Loss function	Mean Square Error (MSE)
Optimizer	Adam; learning rate: 0.001
Learning rate scheduler	MultiStepLR; Milestones=[1800,1900]

Kaiming Uniform initialization, also known as He initialization, is a method used to initialize the weights of neural networks, particularly deep learning models [162]. It is designed to keep the scale of the gradients approximately the same in all layers, which helps in mitigating the vanishing/exploding gradient problems commonly encountered in deep networks. The weights are initialized using a uniform distribution within the range:

$$\omega \sim u(-\sqrt{\frac{6}{in}}, \sqrt{\frac{6}{in}}) \tag{3.16}$$

Where ω is the weight. u is the uniform distribution, and in is the number of input units. Once the training hyperparameters for the network have been established, a few more critical decisions regarding the neural network's architecture need to be made, precisely the number of layers and the number of neurons in each layer. Determining the optimal complexity of a network directly from a dataset is challenging before training begins. Therefore, one typically relies on prior experience to decide on an approximate number of layers and neurons. In this experiment, different neuron and layer structures are tested.

The datasets were split into three subsets in the training process: training, validation, and testing. The training data were utilized to optimize the ANN, with the network's weights and biases being updated through back-propagation. The validation data served a dual purpose: to evaluate the network's performance, act as a checkpoint during training, and detect any overfitting or underfitting that might occur. Finally, the test data, which were entirely new to the network, were employed to assess the network's prediction accuracy after the training was completed. The random seeds in Python scripts are fixed during training to ensure reliability on each trial. All the codes can be viewed in the appendix.

3.4 Genetic algorithm

This thesis employs a genetic algorithm (GA) to couple with the ANN or COMSOL model to optimize geometrical parameters. MOGA optimizes structures for two or more objectives simultaneously, building on GA. MOGA optimization seeks to find a set of solutions that offer trade-offs among different objectives. However, for TEG optimization, this report focuses on a single objective, so MOGA was not used. The ANN was trained based on the previous section before the GA was performed. Figure 3.3 presents the flow chart and detailed steps of the genetic algorithm [158]. The specifics of how the genetic algorithm is implemented in this report will be elaborated in the subsequent section.

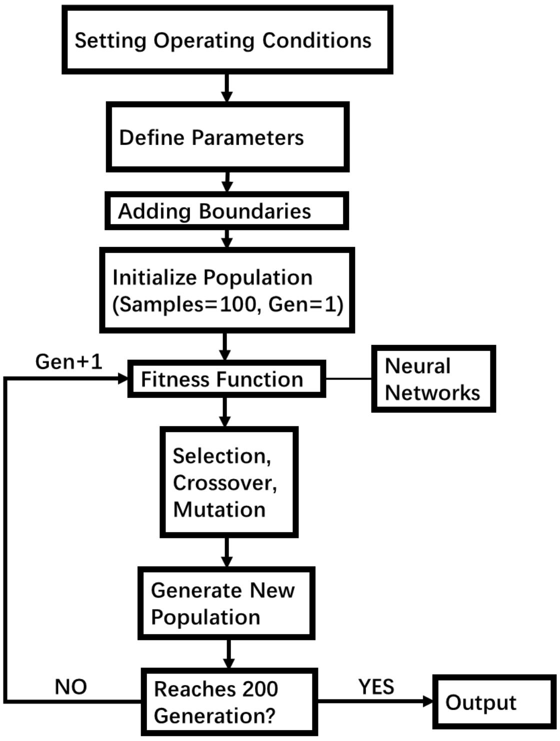

FIGURE 3.3: The flow chart of the GA process for TEG optimization.

Firstly, the operating conditions can be selected to best match practical scenarios. The optimization itself is a meticulous iterative process. In each generation, a specific percentage of the top-performing geometrical parameter sets is preserved. This approach allows the samples to undergo genetic evolution until the predetermined generation time limit is reached.

Before initiating the genetic algorithm, it is essential to determine the size of the population. In this thesis, a population size of 100 candidate designs was chosen. The reason for choosing this population size is that in later experiments, it was observed that the results became stable after 50 cycles. Therefore, selecting a population size of 100 ensures that the optimal results are achieved for each optimization. For each generation within the algorithm, 100 procedures are initially predicted by either the ANN or COMSOL model to yield 100 values. Once the population size is established, the next step is to encode the population. Encoding is a critical aspect of designing genetic algorithms, as it influences the functioning of genetic operators like crossover and mutation and significantly impacts the efficiency of gene evolution. Binary encoding is one of the commonly used methods. Since a binary code sequence of a certain length can represent floating-point numbers with limited precision, it is necessary to determine the resolution of the input parameters.

After determining the encoding method and resolution, the number of bits required for the binary code can be calculated. For instance, consider the parameter W_n with a range of [0.5, 5] and a resolution of 0.01. The total number of discrete values within this range is (5 - 0.5)/0.01 + 1, which equals 451. Since 2^9 equals 512, greater than 451, the number of bits required to encode W_n is 9. This method is applied similarly to calculating the number of bits for the other parameters. The final step involves converting all parameters into binary form using Eqs. 3.17 and Eqs. 3.18 [157].

$$(b_0 b_1 \ldots b_{N-1})_2 = (\Sigma_{i=0}^{N-1} b_i 2^i)_{10} = (BO)_{10} \tag{3.17}$$

$$XO = Lb + BO\frac{Ub - Lb}{2^N - 1} \tag{3.18}$$

Eqs. 3.17 is the formula for converting a binary number to a decimal number (BO). Eqs. 3.17 converts the decimal number (BO) to the original interval [Lb, Ub]. Lb and Ub are the lower and upper bounds for all parameters, respectively. N denotes the number of binary bits, and BO is the decimal number corresponding to the binary number, XO denotes the final output.

After coding all the parameters, a fitness function must be introduced to evaluate which individuals need to be selected. In this thesis, the primary objective of the genetic algorithm is to identify the maximum value, so the fitness function is designed to facilitate this goal. The essence of the fitness function in this investigation is based on the output calculated by either ANN or COMSOL. This is where ANN and COMSOL feed into the

GA process. The output is then processed through the fitness function, as described by specific equations:

$$FitV = FO - min(FO) \tag{3.19}$$

where $FitV$ is the output of the fitness function, and FO is a list of ANN or COMSOL outputs for all populations in one generation. In the fitness function, each data point is subtracted from the minimum value to amplify the differences among the data. After determining the fitness function, the next step is selection. For this thesis, the selection component of the genetic algorithm employs tournament selection.

Tournament selection starts by deciding the number of individuals to be selected at a time. In each selection round, three individuals are randomly chosen from the entire population. Among these, the individual with the highest fitness function is selected. This process is repeated: three individuals are randomly selected from the whole population, and again, the one with the highest fitness value is chosen. This cycle is repeated until the size of the new population equals that of the original population, which, in this thesis, consists of 100 individuals.

After the selection process, creating new populations through chromosome crossover, where binary codes represent chromosomes, is necessary. In a genetic algorithm, crossover involves exchanging segments of two binary codes at a few points to form new binaries. In this thesis, the two-point crossover method was utilized, involving the swapping of segments at two randomly selected points in the chromosome coding strings of the individuals during the crossover process. By selecting two points for crossover, the algorithm can produce a greater variety of offspring compared to single-point crossover. This helps maintain genetic diversity within the population, which is crucial for avoiding premature convergence to local optima. Following the crossover and the formation of new individuals, mutations are introduced to simulate the natural evolutionary process. In this case, each binary-coded gene in the population has a 1% chance of undergoing mutation.

After completing this process, a new generation of populations is entirely generated. This cycle is repeated: new populations are selected based on the fitness function, continuing until the predetermined number of generations is achieved. In this experiment, the population size was set at 100, and the total number of generations was fixed at 200. Regardless of whether the ANN or COMSOL model was utilized to calculate the fitness function, the overall framework of the genetic algorithm remained consistent. All COMSOL simulation and Python scripts run on the Intel 10980xe CPU platform with a Radeon RX 6900XT graphic card. All GA codes can be found in the appendix.

3.5 Conclusion

This section begins with a validation of the COMSOL model and the theoretical model under the same parameters. It also describes the specific training methods for ANNs and the specific algorithms for GA. The methods described in this chapter are applied in later chapters, with only fine-tuning of the parameters. The specific adjustments are described in more detail in the respective chapters. All code and datasets for this thesis can be found in the appendix links.

Chapter 4

Modelling and optimization of conventional bulk TEG by ANN

This chapter delves into modelling a thermoelectric generator (TEG) using artificial neural networks (ANNs). It outlines the process of verifying the model's accuracy and demonstrates how the model can be applied to various parameters. Additionally, it explores integrating the model with genetic algorithms to identify the optimal structure for TEG systems. This approach highlights the potential of combining machine learning techniques with optimization algorithms to enhance thermoelectric generator design accuracy and calculation speed. The complete code of this Chapter can be found in the Appendix.

This chapter has been published as: Yuxiao Zhu, Daniel W. Newbrook, Peng Dai, C.H. Kees de Groot, Ruomeng Huang, Artificial neural network enabled accurate geometrical design and optimisation of thermoelectric generator, Applied Energy, 2022, doi: `10.1016/j.apenergy.2021.117800`. As the first author, my contributions include building the COMSOL model, generating the dataset, building the ANN model, performing the parameter sweep for ANN/COMSOL, GA coding and writing the paper. Daniel provided the thermoelectric material parameters. Peng and Kees reviewed the paper, and Ruomeng reviewed the paper and supervised the project.

4.1 Method

4.1.1 Details of the bulk TEG model

The TEG model investigated in this chapter is shown in Figure 4.1. A 3D model of the thermoelectric generator was constructed in COMSOL, consisting of three main components to initiate the simulation. The top and bottom layers are quartz and designed

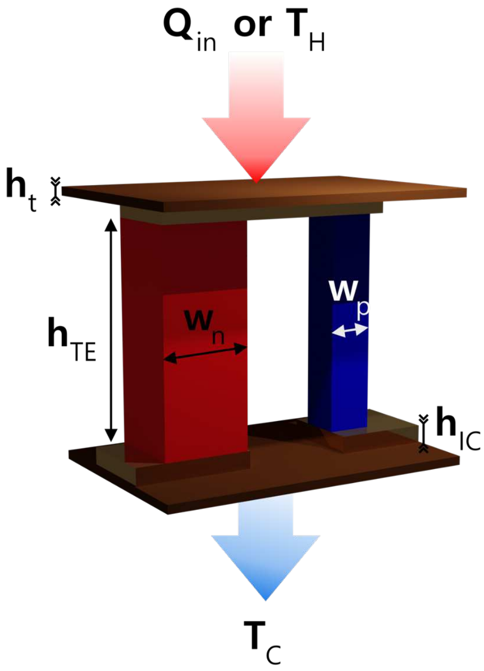

FIGURE 4.1: Conventional single-pair bulk architecture of a thermoelectric generator.

to be insulating yet thermally conductive. The middle section comprises the electrode layer, which connects the n-type and p-type legs. The thickness of the ceramic is fixed at 0.5mm. The thermal boundary conditions are set to a constant cold-side temperature (T_C) of 300 K, and conventional heat flux on all open internal surfaces with a heat transfer coefficient of $1 mW/(cm^2 K)$ and external temperature of 293.15 K to include surface heat convection to air [163]. The specific range and resolution of these parameters are detailed in Table 4.1. For analysis, the parameters have been categorized into two groups: geometric parameters and operating conditions. Once the model has been built, it is necessary to identify the relevant materials. In this chapter, the n-type material is $Bi_2Te_{2.7}Se_{0.3}$ (BiTeSe) [164] and the p-type material is $Bi_{0.5}Sb_{1.5}Te_3$ (BiSbTe) [45]. The COMSOL imports required in the simulation are the Seebeck coefficients, and

TABLE 4.1: Geometrical parameters and operating conditions of TEG.

Geometrical Parameter	**Value Range**	**Resolution**
Height of the TEG leg (H_{TE})	0.5-5 mm	0.01mm
Height of the interconnect (H_{IC})	0.5-3 mm	0.01mm
Filling Factor (FF)	0.05-0.95	0.01
Width of the n-type TEG leg (W_n)	0.5-5 mm	0.01mm
Width of the p-type TEG leg (W_p)	0.5-5 mm	0.01mm
Operating Condition	**Value Range**	**Resolution**
Contact resistivity (ρ_c)	$10^{-9} - 10^{-7}\Omega \cdot m^2$	$10^{-9}\Omega \cdot m^2$
Heat flux (Q_{in})	$100 - 500 mW/cm^2$	$1 mW/cm^2$
Hot-side temperature (T_H)	300-500 K	1 K

thermal and electrical conductivities of the n-type and p-type legs, shown in Figure 4.2. In addition to the parameters mentioned earlier, several specific settings are needed within the COMSOL software and can be found in the Appendix. After constructing the model, the lower two parts of the model must be connected to a voltage and current detection device and a load resistor. This configuration enables the formation of a complete circuit. Using probes, it is possible to measure voltage, current, and power, which allows for the calculation of efficiency.

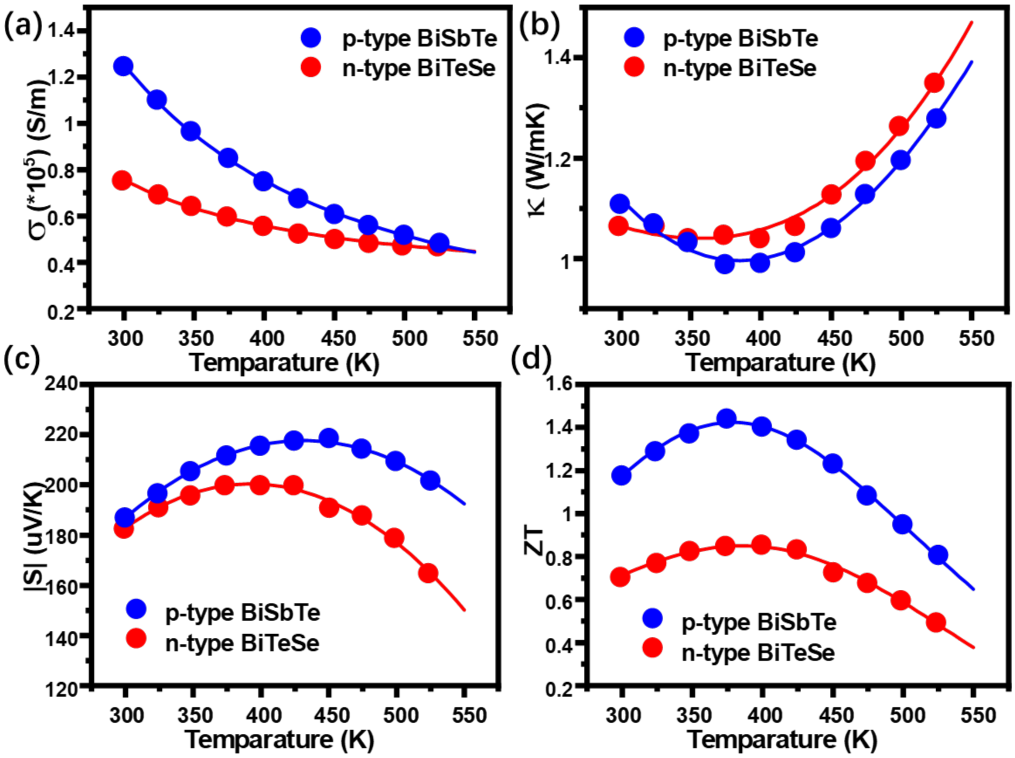

FIGURE 4.2: (a) Electrical conductivity (σ), (b) thermal conductivity (k), (c) Seebeck coefficient (S) and (d) figure of merit (ZT) of the n-type and p-type semiconductors used for the thermoelectric generator.[164][45]

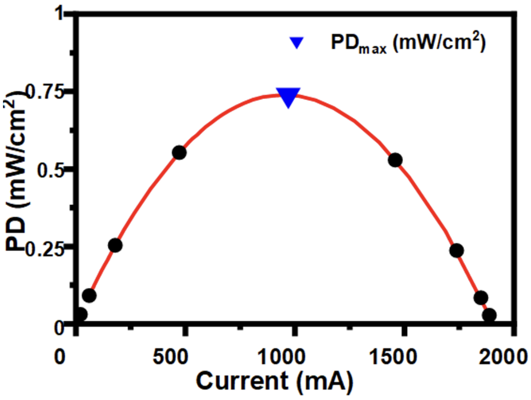

FIGURE 4.3: Power density values for a TEG simulated in COMSOL with different load resistances under constant temperature difference.

For each parameter set, the electrical terminal was connected directly to load resistance and swept from 1/100 to 100 times the internal resistance. The maximum output power was then extracted from a parabolic fit Eqs. 4.1 of the output power against the current out as shown in Figure 4.3, with the goodness of fit 0.999.

$$PD = aI^2 + bI + c \tag{4.1}$$

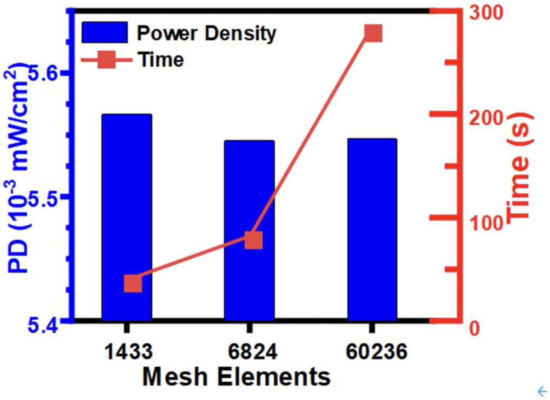

FIGURE 4.4: Power density (blue) and time (red) of the COMSOL simulation performed at different mesh elements.

The impact of mesh sizes on the simulation accuracy was evaluated by simulating the same parameter set with different meshes as shown in Figure 4.4. The results showed that the maximum output power obtained from a "Finer" (6,824 elements) and "Extremely Finer" (60,236 elements) configurations are almost identical with 0.09% difference. Finer mesh configuration was therefore employed to simulate all parameter sets for minimizing computational time while maintaining accuracy. The maximum element size is 0.87mm, and the minimum element size is 0.0632mm. And the maximum element growth rate is 1.4.

4.1.2 ANN configuration and dataset distribution

The configuration of the forward modelling network adopted in this work is shown in Figure 4.5. The network was constructed by fully connecting the input layer of geometrical parameters (FF, H_{TE}, H_{IC}, W_n, W_p) and operating conditions (ρ_C, Q_{in} or T_H) with output layer of power performance (PD_{max} and η) through 2, 3, 4, 5, and 6 hidden layers.

To train the artificial neural network, randomly generating 5000 distinct sets of input data is essential, adhering to the resolution and range specified in Table 4.1. This is generated in a Python script, which saves an Excel file containing 5000 input datasets. As previously mentioned, this chapter utilizes two types of input parameters: a constant heat flux density and a constant temperature difference. Therefore, 5000 sets of input

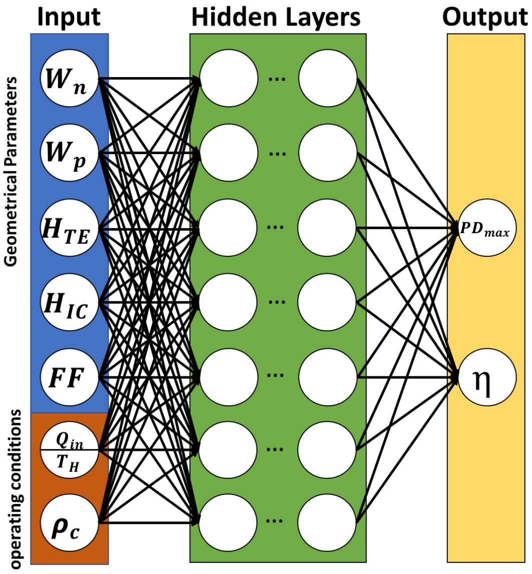

FIGURE 4.5: Architecture of the forward modelling neural network for predicting power performance of the TEG model. The input layer contains geometrical parameters (FF, H_{TE}, H_{IC}, W_n, W_p) and operating conditions (ρ_C, Q_{in} or T_H). The output layer contains power performance values (PD_{max} and η).

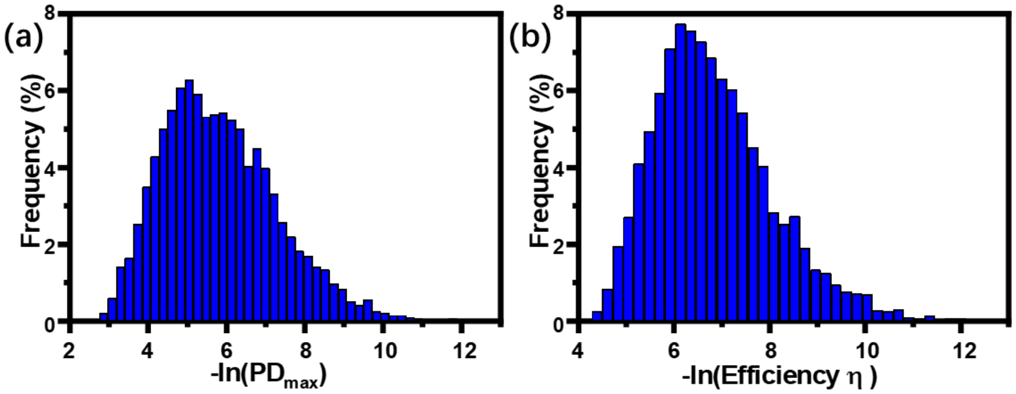

FIGURE 4.6: Distribution of the (a) maximum power density PD_{max}, (b) efficiency η for the dataset under the operating condition of constant temperature difference

data are generated for the simulation for each type of input parameter. Although the two data sets will have other distributions, the general type of distribution is similar. The input Excel file is then imported into COMSOL to simulate the output results. Finally, the complete dataset of 5000 is obtained. Figure 4.6 and Figure 4.7 show the constant temperature difference and heat flux density datasets. The distribution of PD_{max} and efficiency η indicate the reason for normalizing the output dataset in log-normal distribution. All datasets can be found in the link in the code in Appendix.

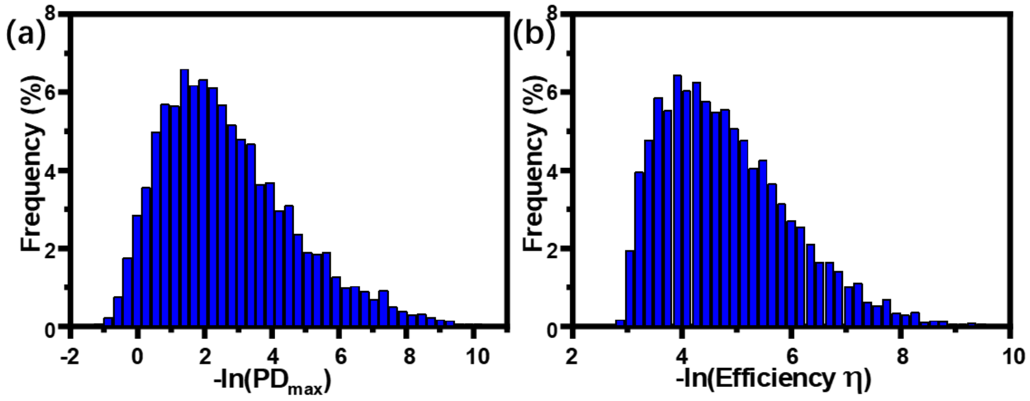

FIGURE 4.7: Distribution of the (a) maximum power density PD_{max}, (b) efficiency η for the dataset under the operating condition of constant heat flux

4.1.3 Genetic algorithm

The genetic algorithm is used in this project to optimize the TEG structure under specific operating conditions. And compare the ANN-GA results with COMSOL-GA results to show the accuracy of ANN. For the conventional bulk TEG, the genetic algorithm begins by setting the operating conditions, with specific parameter settings detailed in Figure 4.8. The dataset of operating conditions are randomly generated by Python script. The algorithm operates with 100 populations in each epoch, and 200 generations are conducted to ensure the population reaches an optimal position. In this chapter, the fitness function of GA is determined based on the results obtained either from the ANN or COMSOL simulations.

4.2 ANN performance under constant temperature difference

4.2.1 ANN hyperparameters optimization

The prediction performance of ANN for TEG operating under constant temperature differences will first be evaluated. A systematic study was first conducted to investigate the impact of the hyperparameters (layer and neuron numbers) for this ANN. Figure 4.9 shows the validation loss curves over epochs for neural networks with different neuron numbers per layer and different hidden layers. Figure 4.9 shows the training process of the neural network. The code of training can be found in the Appendix. The validation dataset is outside the training dataset, so it can effectively check whether the network appears to be overfitting. Nevertheless, the final test dataset is needed to verify the final effect of the neural network. The test dataset is separate from the training dataset and the validation dataset. It is used to simulate the use of the neural network after it has been trained. Therefore, the neural network structure derived from the test dataset is a good representation of the network's performance. Here, a relative

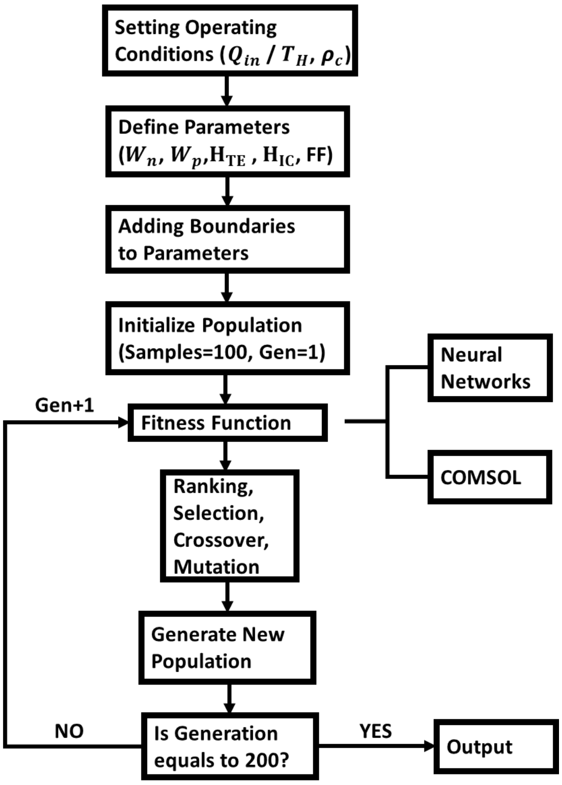

FIGURE 4.8: Flow chart of bulk TEG modelling genetic algorithm

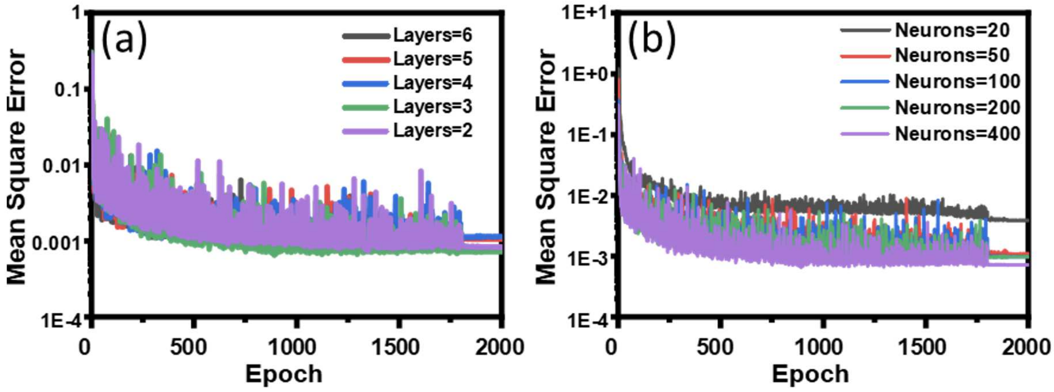

FIGURE 4.9: The neural network training for forwarding modelling TEG power performance under the constant temperature difference operation condition. The validation loss curves of (a) different hidden layers with neurons fixed to 400 and (b) different neurons with hidden layers fixed to 5.

error between the predicted and actual power performance is defined to compare the performance of the ANN:

$$RelativeError = \frac{|P_{true} - P_{predicted}|}{P_{true}} \tag{4.2}$$

Where the P_{true} is output from COMSOL simulation, and $P_{predicted}$ is from the ANN model. The distribution and average of the relative error as a function of layer numbers and neuron numbers are plotted in Figure 4.10. Regarding the different layers, the brown part in Figure 4.10a shows that the percentage of relative error under 0.01 is larger, while the percentage of relative error over 0.05 is the smallest. This contributes to improved accuracy. The average relative error in the test dataset decreases significantly from 0.044 to 0.019 as neurons per layer increase from 20 to 400. The relative error distribution also suggests that most of the errors are within 3%, indicating the network's extremely high prediction accuracy. Therefore, a network of 5 layers and 400 neurons per layer was adopted for this operating condition.

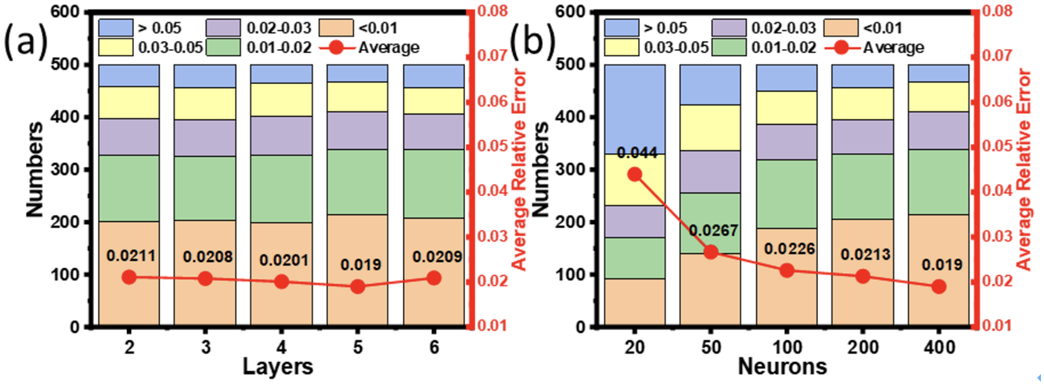

FIGURE 4.10: The test dataset relative error of (a) different hidden layers with neurons fixed to 400 and (b) different neurons with hidden layers fixed to 5 under constant temperature difference.

4.2.2 The GA optimization and analysis of the ANN model

Figure 4.11 plots the comparison between the true (simulated) power performance of PD_{max} and efficiency values in the test dataset with the ones predicted by the ANN. It can be observed that the high prediction accuracy of our ANN prevails over three orders of magnitude, producing a high coefficient of determination value (R^2) of over 0.999 for both PD_{max} and efficiency. This outstanding prediction accuracy over an extensive range is helpful for its application in TEG optimization.

Once the forward TEG model is established, it can be used to perform analytical studies to investigate the impact of different parameters on the performance of TEG. As many parameters can be analyzed, here is one example involving FF and H_{TE}. Comparisons of other parameters can be done using the code provided in the appendix.

Figure 4.12 presents the PD_{max} and η values as a function of H_{TE} and FF while the H_{IC}, W_n and W_p values were fixed at 1.5 mm, 2.5 mm, and 2.5 mm, respectively. Under the

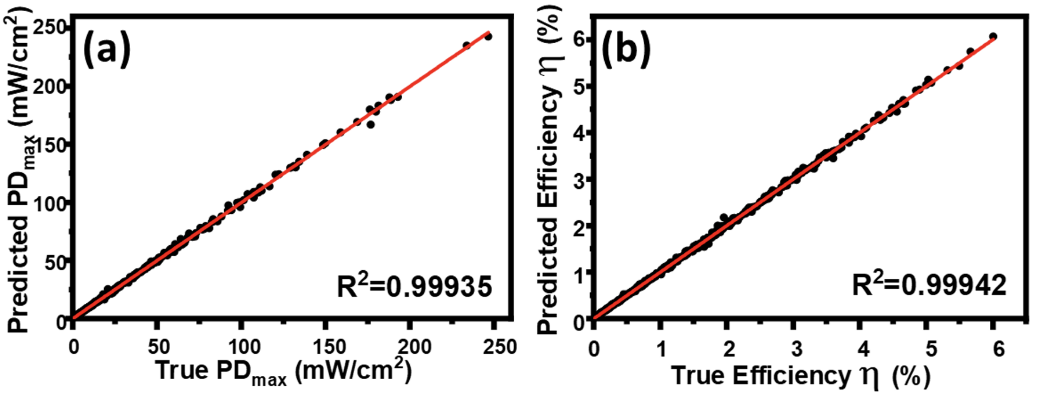

FIGURE 4.11: Scatter plot of the ANN predicted and the true (simulated) (a) PD_{max} and (b) efficiency η under the operating condition of constant temperature difference.

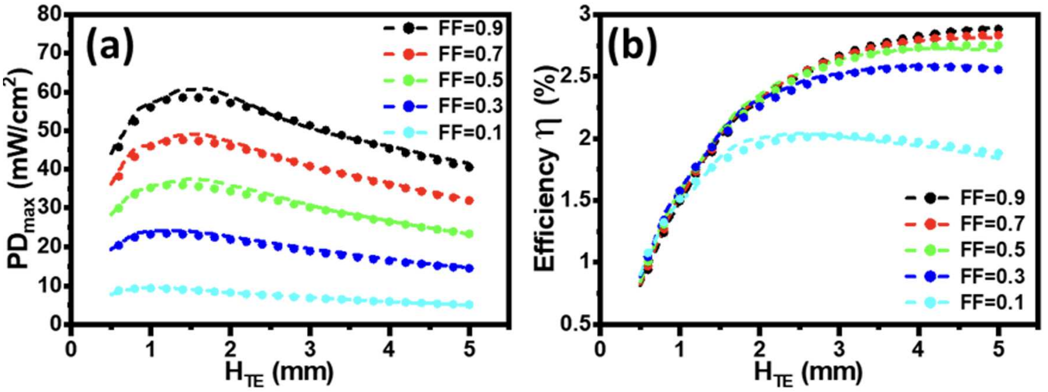

FIGURE 4.12: (a) PD_{max} and (b) efficiency η obtained from ANN (line) and COMSOL simulation (dots) as a function of (c, d) H_{TE} and FF. The operating condition chosen is T_H of 400 K and ρ_C of $10^{-8}\Omega \cdot m^2$. The H_{IC}, W_n and W_p values were fixed at 1.5 mm, 2.5 mm, and 2.5 mm, respectively.

operating condition of T_H=400 K and ρ_C=$10^{-8}\Omega \cdot m^2$, larger FF is favourable for achieving larger PD_{max} as shown in Figure 4.12a. In our model, changing of FF is achieved by varying the total area of the model to ensure the W_n and W_p remain unchanged. A large FF implies a small TEG area increased PD_{max}. The dependence of H_{TE} is more complicated. Small H_{TE} limits the power performance with a small temperature gradient over the TE legs, while large H_{TE} deteriorates the power by increasing the electrical resistance. It results in an optimized H_{TE} for each FF. On the other hand, the efficiency η undergoes different trends with varying H_{TE} and FF as shown in Figure 4.12b. Although a large FF is still advantageous, its benefit decreases at larger FF values due to the concurrently increased Q_{in}. Unlike PD_{max}, higher η can be achieved with larger H_{TE} values except for smaller FF (0.1). COMSOL simulations were also conducted for the same parameter sets. It achieved high consistency with the results generated by ANN, as shown in Figure 4.12. This trend suggests that our ANN can be used to perform an analytical investigation of the TEG with high accuracy.

Once the network is trained and verified, it can be used for design optimization. Two

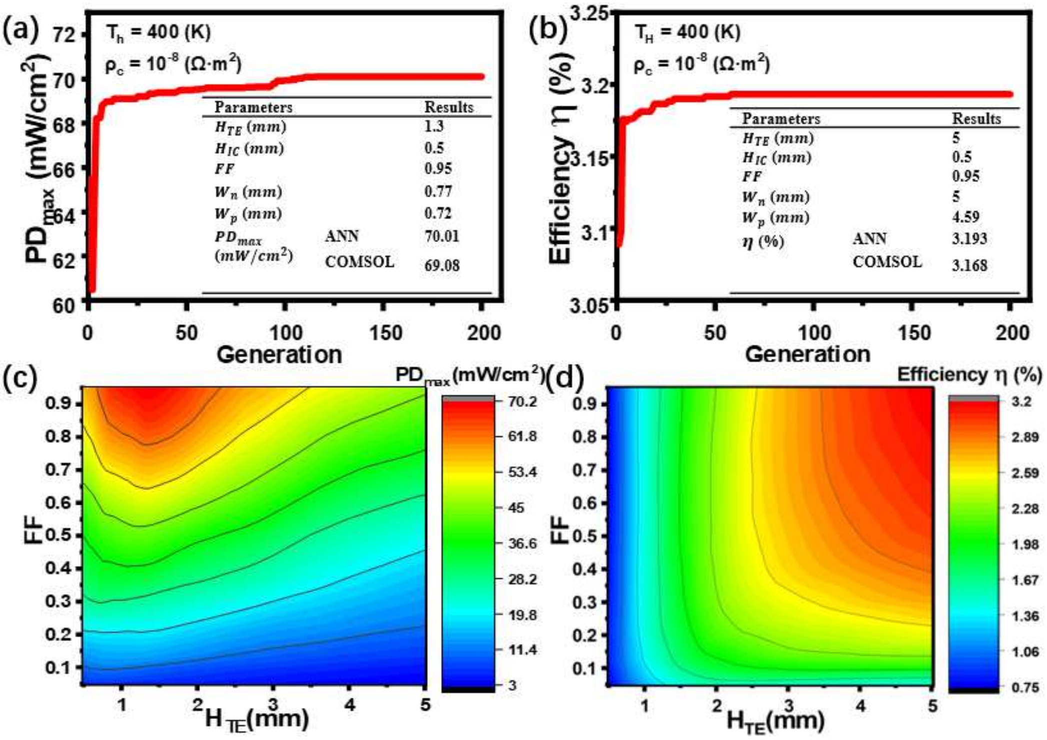

FIGURE 4.13: Convergence curve of genetic algorithm for (a) PD_{max} and (b) η under an operating condition of T_H is 400 K and ρ_C is $10^{-8}\Omega \cdot m^2$. (c) Colour map of PD_{max} and (d) efficiency η obtained from ANN as a function of H_{TE} and FF. The optimized values are listed in the inset table.

separate optimizations have been conducted to maximize power and efficiency, respectively. The operating condition of T_H=400 K and ρ_C=$10^{-8}\Omega \cdot m^2$ were chosen as an example. Figure 4.13a and Figure 4.13b plots the GA convergence curves for power and efficiency optimizations. Both processes converge well after ca. 100 generations. A maximum power density of 70 mW/cm^2 was identified (Figure 4.13a), while the maximum efficiency was 3.2% (Figure 4.13b). The designs (shown in Figure 4.13a and b) reaching those two optimized values are significantly different.

To verify the effectiveness of our GA optimization process, colour maps of both H_{TE} and FF were conducted as shown in Figure 4.13c and d. Under a constant T_H of 400 K, the optimized H_{TE} is 1.3 mm to achieve the largest PD_{max}. This is confirmed by sweeping its value from 0.5 mm to 5 mm by ANN and simulation, as shown in Figure 4.13c. On the other hand, maximum efficiency η requires the optimized H_{TE} to reach the upper limit (5 mm) of the preset range (Figure 4.13d). The discrepancy of the optimized H_{TE} values can be explained by the reducing Q_{in} as H_{TE} increases, leading to higher η but smaller PD_{max}. In both cases, results obtained from ANN are highly consistent with those from COMSOL simulation. The optimization of FF was also investigated. ANN coupled GA has found the largest FF (0.95) in the preset range for best PD_{max}. Increasing FF results in larger PD_{max} (shown in Figure 4.13c), which is mainly due to the reduction of the TEG electrical resistance. Similarly, a considerable FF is also required for high efficiency η (shown in Figure 4.13d) as the PD_{max} increment from larger FF outweighs the increment of Q_{in}.

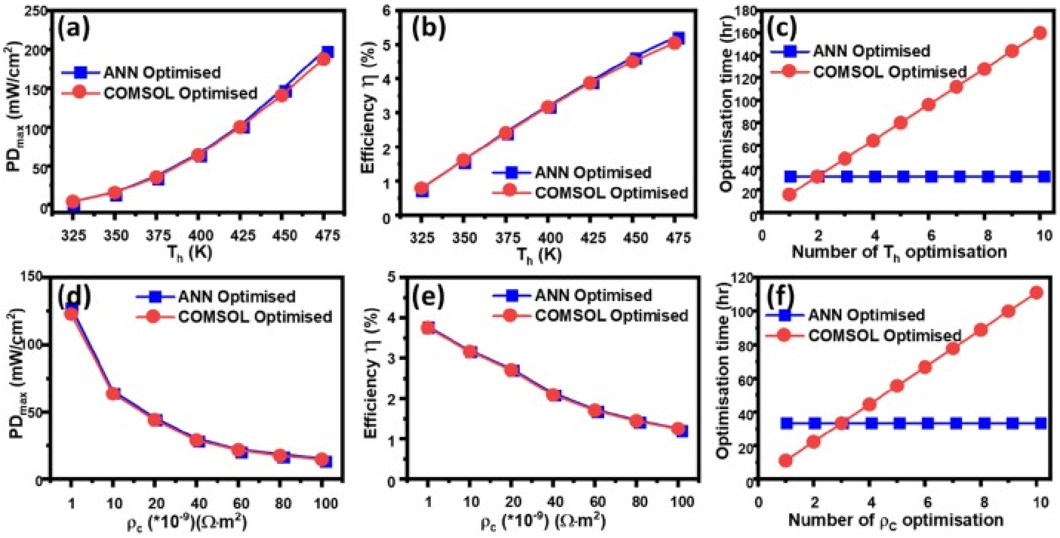

FIGURE 4.14: Optimization of (a) PD_{max} and (b) efficiency η by GA coupled with ANN (blue dots) and COMSOL simulation (red dots) as a function of T_H; (c)required optimization time of both methods for different T_H conditions; optimization of (d) PD_{max} and (e) efficiency η by GA coupled with ANN and COMSOL as a function of ρ_C, (f) required optimization time of both methods for different ρ_C conditions.

The key advantage of the deep learning-aided approach is its high design efficiency. Here, the developed ANN and the COMSOL simulation are compared by coupling both processes with GA to execute the same optimization tasks. Figure 4.14a and Figure 4.14b presents the optimized PD_{max} and efficiency η for different T_H conditions. Both optimized values increase with larger T_H. All optimized values from the two approaches are almost identical, with similar geometrical parameters obtained (listed in Table 4.2). However, the average time for COMSOL simulation coupled optimization was 57,600 s (ca. 16 hrs), while it only took an average of 40 s for ANN to complete one optimization. Although ANN requires a one-time investment for dataset generation (125,106 s, ca. 35 hrs) and network training (248 s), it is a much more cost-effective way if optimizations under multiple T_H conditions are required. Figure 4.14c plots the time required for both methods to perform multiple optimizations. It is clear that the amount of time saved by using ANN easily recovers the up-front computational time for the network when more than 2 optimizations are needed.

Similarly, in Figure 4.14d and Figure 4.14e, optimization against different ρ_C results in good agreements between the ANN and COMSOL simulation coupled optimizations. The ANN approach only requires an average of 35 s while the latter demands 40,000 s (ca. 11 hrs). The amount of time saved by using ANN for optimization quickly recovers the computational time for the dataset generation (125,106 s, ca. 35 hrs) and the network training (248 s). Significant time saving can be achieved if more than 3 optimizations are required as shown in Figure 4.14f. In both cases, an improvement in computational efficiency of over 1,000 times was obtained. This superior design efficiency offered by ANN represents a significant saving of computational time and energy.

However, it can be seen that an increase in error occurs when the PD_{max} is large, which may be due to a reduction in the number of datasets near the boundary. Therefore, before modelling with ANN, the boundaries of the dataset need to be securely defined to ensure that the required data is primarily in the middle range. Additionally, algorithms such as the iterative algorithm mentioned later can be effective in reducing this issue.

TABLE 4.2: List of GA optimized geometrical parameters based on COMSOL simulation (left) and ANN (right) at different hot-side temperatures and contact resistivity values for PD_{max} optimization

T(K)	325		350		375		400		425		450		475	
H_{TE}(mm)	1.56	1.7	1.51	1.33	1.48	1.05	1.45	1.3	1.4	1.34	1.39	1.05	1.38	1
FF	0.95	0.95	0.95	0.95	0.95	0.95	0.95	0.95	0.95	0.95	0.95	0.95	0.95	0.95
H_{IC} (mm)	0.52	0.54	0.57	1.44	0.55	0.5	0.59	0.5	0.51	1.03	0.54	0.55	0.51	0.5
W_n/W_p	1.14	1.02	1.15	1.14	1.15	1.14	1.16	1.07	1.15	1.12	1.15	1.05	1.13	1.1
$\rho_C(\Omega\cdot m^2)$	10^{-9}		10^{-8}		$2*10^{-8}$		$4*10^{-8}$		$6*10^{-8}$		$8*10^{-8}$		10^{-7}	
H_{TE} (mm)	0.73	0.73	1.45	1.3	1.91	1.9	2.49	3.31	3.05	3.11	3.46	3.71	3.92	4.1
FF	0.95	0.95	0.95	0.95	0.95	0.95	0.95	0.95	0.95	0.95	0.95	0.95	0.95	0.95
H_{IC} (mm)	0.74	1.75	0.59	0.5	0.53	0.55	0.52	0.5	0.51	1.24	0.5	0.81	0.52	0.5
W_n/W_p	1.27	1.09	1.16	1.07	1.12	1.05	1.08	1.14	1.07	1.04	1.06	1	1.05	1

TABLE 4.3: List of GA optimized geometrical parameters based on COMSOL simulation (left) and ANN (right) at different hot-side temperatures and contact resistivity values for efficiency.

T(K)	325		350		375		400		425		450		475	
H_{TE} (mm)	5	5	5	5	5	5	5	5	5	5	5	5	5	5
FF	0.95	0.95	0.95	0.95	0.95	0.95	0.95	0.95	0.95	0.95	0.95	0.95	0.95	0.95
H_{IC} (mm)	0.5	0.5	0.5	0.5	0.5	0.5	0.5	0.5	0.5	0.5	0.5	0.5	0.5	0.5
W_n/W_p	1.12	1.1	1.12	1.11	1.12	1.1	1.12	1.09	1.11	1.09	1.1	1	1.09	1
$\rho_C(\Omega\cdot m^2)$	10^{-9}		10^{-8}		$2*10^{-8}$		$4*10^{-8}$		$6*10^{-8}$		$8*10^{-8}$		10^{-7}	
H_{TE} (mm)	5	5	5	5	5	5	5	5	5	5	5	5	5	5
FF	0.95	0.95	0.95	0.95	0.95	0.95	0.95	0.95	0.95	0.95	0.95	0.95	0.95	0.95
H_{IC} (mm)	0.5	0.5	0.5	0.5	0.5	0.5	0.5	0.5	0.5	0.5	0.5	0.5	0.5	0.5
W_n/W_p	1.14	1.09	1.12	1.09	1.08	1.09	1.06	1.05	1	1.03	1.04	1	1.04	1.04

The data are relatively similar in most cases, as seen from the two tables, Table 4.2 and Table 4.3. However, in many cases, parameters such as H_{TE} are close to the boundary values. This suggests that those parameters are not necessary for optimization and can be fixed to a reasonable value in future studies. Different W_n/W_p can also lead to changes in H_{TE}, and significant data differences can occur occasionally. However, even with substantial differences in geometrical parameters, the final COMSOL simulation results obtained similarly, as shown in Table. 4.2 and Table. 4.3.

4.3 ANN performance under constant heat flux

4.3.1 ANN hyperparameters optimization

The focus now shifts to the operating condition of constant heat flux. The operation is essentially the same for data sets with constant heat flux. However, since the efficiency of the constant heat flux can be calculated directly from the power density, the neural network's output in this part is only the maximum power density. Again, the number of layers and neurons of the neural network was scanned to compare the results. The training results for a validation dataset at constant heat flux are shown in Figure 4.15.

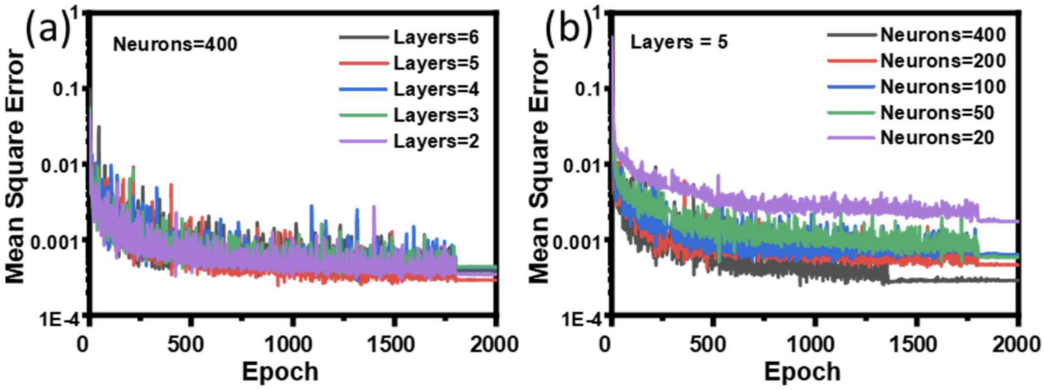

FIGURE 4.15: The validation loss curves of (a) different hidden layers with neurons fixed to 400 and (b) different neurons with hidden layers fixed to 5.

As shown in Figure 4.15, the stabilized validation loss is minor for the network with most neurons per layer of 400 and with layers 5. Furthermore, as a test dataset for comparing the effectiveness of neural networks, Figure 4.16 shows the relative errors at different numbers of layers and neurons. Like the previous condition, the relative error decreased from 0.0424 to 0.0177, with neurons per layer increasing from 20 to 400, as shown in Figure 4.16b. This 5-layer and 400 neurons per layer network with a prediction accuracy of over 98% was adopted for this condition.

Now that the network structure has been optimized, all that remains is to start training the neural network and analyzing the results.

4.3.2 The GA optimization and analysis of the ANN model

As the efficiency can be directly converted from power output, only PD_{max} will be presented and discussed in this section. Similarly, the above analysis has shown the final chosen neural network structure for the constant heat flux ANN, with five layers and 400 neurons per layer. Figure 4.17 compares the maximum power output PD_{max}

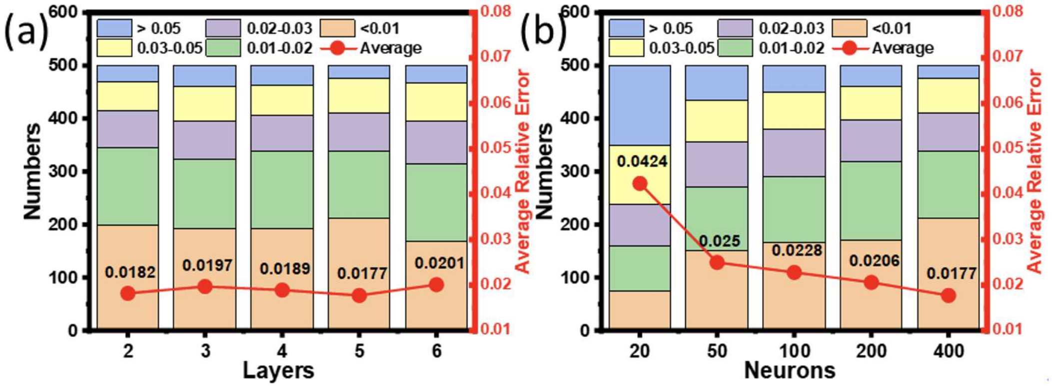

FIGURE 4.16: The test dataset relative error of (a) different hidden layers with neurons fixed to 400 and (b) different neurons with hidden layers fixed to 5 under constant heat flux.

from the ANN with the true (COMSOL simulated) values in the test dataset. Again, high consistency can be observed between the true and ANN predicted values with a high coefficient of determination (R^2) of 0.99943, showing great prediction accuracy over the entire power range.

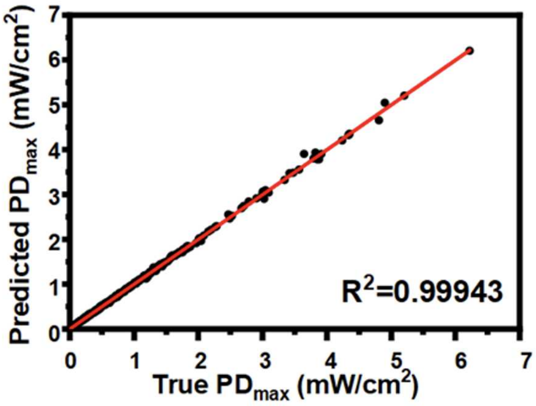

FIGURE 4.17: Scatter plot of the ANN predicted and the true (simulated) maximum power density (PD_{max}) under the operating condition of constant heat flux.

The analytical study under the constant heat flux condition was also conducted using this network to investigate the impact of H_{TE} and FF. The operating condition was chosen to be $Q_{in} = 300mW/cm^2$ and ρ_C=$10^{-8}\Omega \cdot m^2$ while the H_{IC}, W_n and W_p values were fixed at 1.5 mm, 2.5 mm, and 2.5 mm, respectively. Figure 4.18 presents the PD_{max} and η values as a function of H_{TE} and FF. Both values increase with leg length due to the more significant temperature gradient created. However, the increment rate decreases at higher H_{TE} values due to the adverse impact of more considerable electrical resistance. On the other hand, smaller FF is preferred to achieve high power performance. A smaller FF implies a larger TEG area, leading to an enormous temperature difference and PD_{max}. The low efficiency shown in the Figure 4.18 is due to the low input power. While increasing the FF increases the input power, it also increases the area, making it difficult for the TEG to fully utilize the input heat flow over the entire surface. Meanwhile, the reason for not seeing a curve of slowly decreasing power with increasing H_{TE} is that the internal resistance is not large enough. This issue arises from the irrational scope of the dataset selection, making it difficult to obtain data for the latter part. In all cases, the simulation results show high consistency with the results generated by ANN.

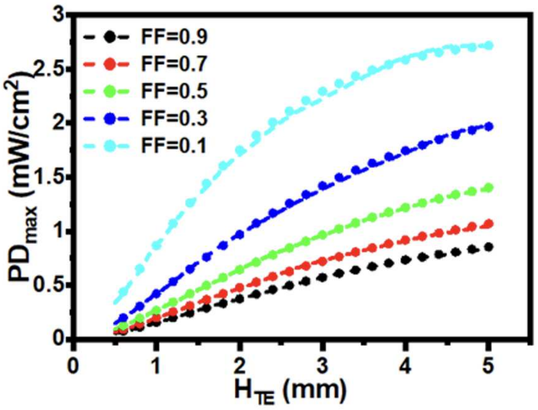

FIGURE 4.18: PD_{max} obtained from ANN (line) and COMSOL simulation (dots) as a function of H_{TE} and FF. The operating condition chosen is Q_{in} of 300 mW/cm^2 and ρ_C of $10^{-8}\Omega \cdot m^2$. The H_{IC}, W_n and W_p values were fixed at 1.5 mm, 2.5 mm, and 2.5 mm, respectively.

After establishing the prediction accuracy of the network, the application of the ANN in TEG optimization will now be evaluated by coupling it with GA. The similar operating condition of $Q_{in} = 300mW/cm^2$ and ρ_C=$10^{-8}\Omega \cdot m^2$ was chosen as an example for optimization. Figure 4.19a shows the convergence curve of GA for PD_{max} which converges after 200 generations. The optimized geometrical parameters are listed in the inset table. Sweepings of H_{TE} and FF were subsequently performed to verify the optimized values. Figure 4.19b displays the colour map of H_{TE} and FF. A shorter leg could lead to a beneficially smaller electrical resistance and an adversely decreased temperature difference under this operating condition. It can be observed that our GA has correctly identified the optimized value of 4.81 mm. A large FF implies a smaller TEG area, leading to a smaller temperature difference and maximum power output.

On the other hand, a very small FF could induce significant interconnect resistance that also deteriorates the power. An optimized FF of 0.11 was identified and verified by sweeping using both ANN and simulation. In addition, COMSOL simulations were also conducted using the same parameter sets. The simulated results (dots) match with the predicted results from ANN (line), further confirming the high accuracy of our network.

TABLE 4.4: List of GA optimized geometrical parameters based on COMSOL simulation (left) and ANN (right) at different heat flux density and contact resistivity values for PD_{max} optimization.

T(K)	325		350		375		400		425		450		475	
$Q_{in}(mW/cm^2)$	150		250		350		450		425		450		475	
H_{TE}(mm)	5	5	5	4.87	5	5	5	4.81	5	5	5	5	5	5
FF	0.08	0.11	0.09	0.11	0.09	0.11	0.09	0.11	0.1	0.12	0.1	0.13	0.1	0.12
H_{IC} (mm)	0.5	0.5	0.5	0.5	0.5	0.5	0.5	0.5	0.5	0.5	0.5	0.5	0.5	0.5
W_n/W_p	1.12	1.19	1.14	1.02	1.11	1.1	1.1	1.01	1.12	0.99	1.1	1.12	1.1	1.01
$\rho_C(\Omega \cdot m^2)$	10^{-9}		10^{-8}		$2*10^{-8}$		$4*10^{-8}$		$6*10^{-8}$		$8*10^{-8}$		10^{-7}	
H_{TE} (mm)	3.22	2.99	5	4.81	5	5	5	5	5	5	5	5	5	5
FF	0.06	0.06	0.09	0.11	0.09	0.11	0.09	0.12	0.09	0.11	0.1	0.13	0.09	0.13
H_{IC} (mm)	0.5	0.5	0.5	0.5	0.5	0.5	0.5	0.5	0.5	0.5	0.5	0.5	0.5	0.5
W_n/W_p	1.14	1.14	1.1	1.01	1.09	1.11	1.04	1.01	1.05	1.07	1.06	1.01	1.05	1.02

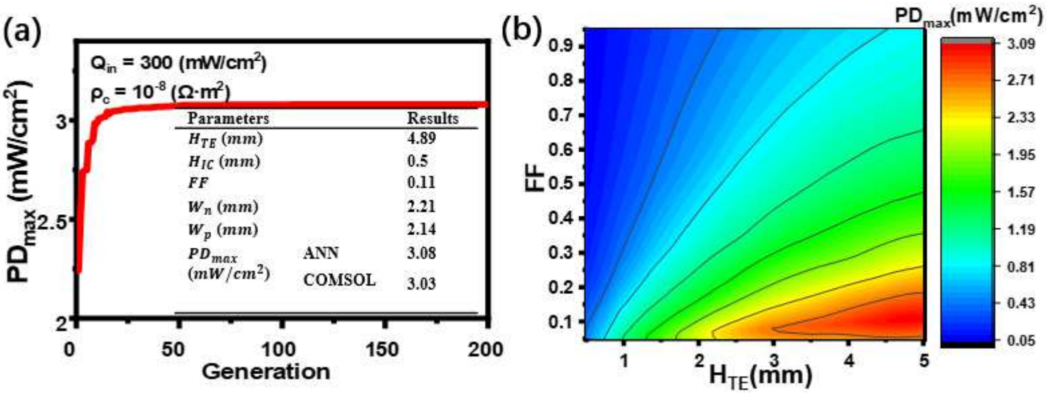

FIGURE 4.19: (a) Convergence curve of genetic algorithm for maximum power output under an operating condition of Q_{in} is 300 mW/cm^2 and ρ_C is $10^{-8}\Omega \cdot m^2$. (b) Colour map of PD_{max} obtained from ANN as a function of H_{TE} and FF. The optimized values are listed in the inset table and labelled by the red dots.

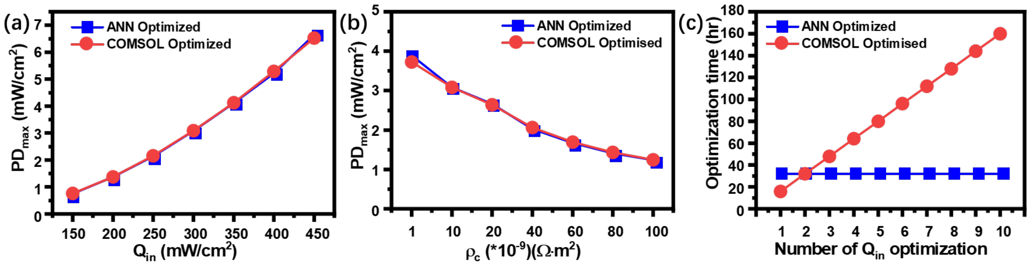

FIGURE 4.20: PD_{max} optimized by GA coupled with ANN (blue dots) and COMSOL simulation (red dots) as a function of (a) Q_{in} and (b) ρ_C; (c)required optimization time of both methods for different number of Q_{in} conditions;

An efficiency comparison between the developed ANN and the conventional simulation was conducted under constant heat flux conditions. Figure 4.20a and Figure 4.20b presents the optimized PD_{max} under different Q_{in} and ρ_C values. As expected, larger Q_{in} and smaller ρ_C can produce larger optimized PD_{max}. The ANN and COMSOL simulation approaches obtained highly consistent, optimized values. The average optimization time for ANN-coupled GA is 40 s. 60,000 s (ca. 16 hrs) for COMSOL coupled

GA, saving computational time and resources over 1,000 times. This indicates significant time-savings when more than 2 optimizations are required (shown in Figure 4.20c).

As only the maximum value of PD_{max} needs to be measured, there is only one table to present the data. As can be seen from Table. 4.4, the H_{IC} data is as small as possible, and the H_{TE} is often close to the boundary value. The difference in FF is sometimes more prominent, but this varies with W_n/W_p. From Figure 4.20, the final PD_{max} results from the COMSOL simulation data are similar.

4.4 Conclusion

In this chapter, the first application of deep learning techniques in forward modelling of the power performance of a TEG is demonstrated. After training using a dataset from 3-D COMSOL simulations, the ANNs demonstrated extremely high prediction accuracy of over 98%. They can operate under constant temperature difference and heat flux conditions while considering the contact electrical resistance, surface heat transfer and other thermoelectric effects. Analytical studies using the developed networks have been successfully conducted to investigate the impact of different parameters on the TEG performance, and the results have shown high consistency with those generated from COMSOL simulation.

The excellent performance of the networks is further verified by coupling with GA to perform design optimization. With almost identical optimized values obtained, our ANNs demonstrated superior optimization efficiencies that are, on average, over 1,000 times better than the COMSOL simulation coupled GA optimization.

Chapter 5

Modelling and optimization of segmented TEG by ANN

The preceding chapter introduced the concept of modelling primary bulk thermoelectric generators (TEGs) using artificial neural networks (ANNs). Building on this, the current chapter extends the exploration to TEGs with more complex structures, focusing specifically on segmented thermoelectric generators. Due to their intricate designs and materials, these generators present a more significant challenge for ANN modelling, particularly in maintaining high accuracy, given the increased complexity of input parameters. To address these challenges, this chapter introduces a novel training approach—iterative training—for segmented thermoelectric generators. This method aims to enhance the accuracy of the neural network model by refining the training process to better account for the complexities inherent in segmented TEGs. A comparative analysis between the traditional and iterative training methods is presented to highlight the improvements in modelling accuracy.

Furthermore, the chapter explores the application of the model across various parameters, demonstrating its versatility. It also investigates how the model can be integrated with genetic algorithms to identify the optimal structure for segmented TEGs. This approach showcases the potential of combining ANN modelling with optimization techniques. It underscores the importance of innovative training methodologies in overcoming the challenges posed by more complex thermoelectric generator designs.

This chapter has been published by Yuxiao Zhu, Daniel Newbrook, Peng Dai, Jian Liu, Kees de Groot, and Ruomeng Huang, Segmented thermoelectric generator modelling and optimisation using artificial neural networks by iterative training, Energy & AI, vol. 12, no. December 2022, doi: `10.1016/j.egyai.2022.100225`. As the first author, I came up with the idea of the iterative algorithm, built the COMSOL model, generated the dataset, and wrote the code for the ANN model. I also scanned the trained ANN for parametric analysis, handled the GA-related work, and wrote the paper. Daniel provided the room temperature TE material parameters, Peng discussed the algorithm-related content, Jian and Kees reviewed the paper, and Ruomeng reviewed the paper and guided the direction of the project.

5.1 Method

5.1.1 Details of the segmented TEG model

Figure 5.1 shows the segmented thermoelectric generator (STEG) model built in this chapter. This model was chosen to discuss the case of fixed heat flux mainly because achieving a fixed temperature difference is difficult in practical situations, and there are many scenarios involving fixed heat flux. Therefore, heat flux is used as a parameter for modelling and analysis in this example. The top and bottom brown insulating layers in Figure 5.1 are aluminium nitride ceramics with high thermal conductivity. Immediately adjacent to the insulation is the top electrode made of copper. Both thermoelectric legs are made of a high-temperature thermoelectric material (top) and a low-temperature thermoelectric material (bottom).

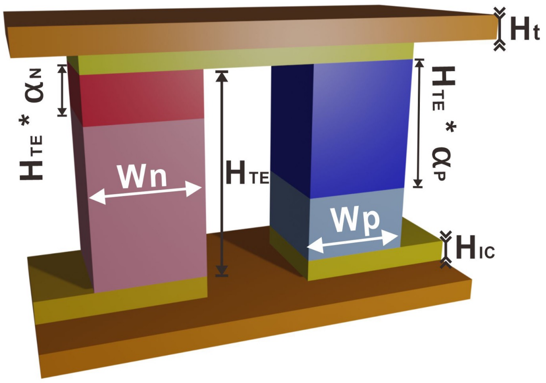

FIGURE 5.1: Schematic of the singe-pair segmented thermoelectric generator modelled in this study.

Thermoelectric materials developed from past studies are selected, and their associated ZT values are shown in Figure 5.2. For the n-type leg, $PbTe_{0.998}I_{0.002} - 3\%Sb$ [165] was selected as the high-temperature thermoelectric material (dark red), and $Bi_2Te_{2.7}Se_{0.3}$ [164] was selected as low-temperature thermoelectric material (light red). For the p-type leg, $K_{0.02}Pb_{0.98}Te_{0.15}Se_{0.8}$ (dark blue) [166] and $Bi_{0.5}Sb_{1.5}Te_3$ (light blue) [45] were selected as high and low-temperature materials, respectively. The temperature-dependent thermoelectric properties, including the Seebeck coefficient (S) and electrical (σ) and thermal conductivities (k), are shown in Figure 5.2.

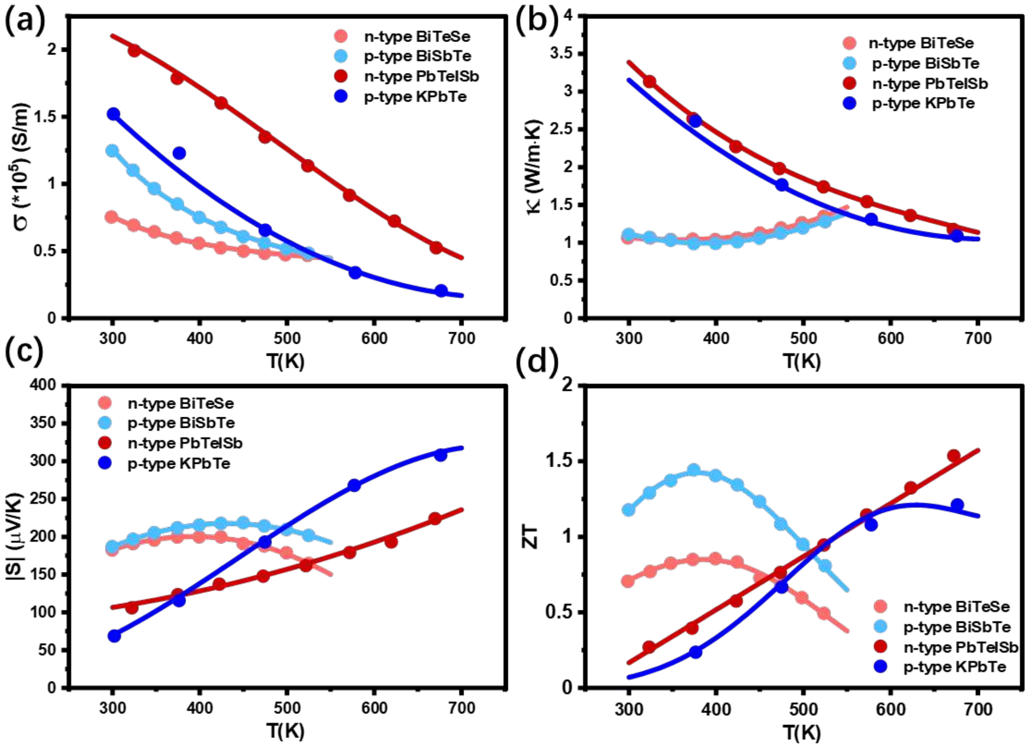

FIGURE 5.2: Temperature-dependent. (a) Electrical conductivity (σ), (b) thermal conductivity (k), (c) Seebeck coefficient (S), and (d) figure of merit (ZT) of the n-type and p-type semiconductors used for the thermoelectric generator[45] [165] [164] [166].

The model variables are divided into geometrical parameters and operating conditions. Geometrical parameters include the height (H_{TE}) and width (W_{TE}) of the n-type and p-type legs. In this chapter, the widths of the two legs are kept the same and can be defined by the fill factor (FF), which is the ratio between the cross-sectional areas of the two legs ($W_n^2 + W_p^2$) and the entire device (A_{TEG}). For segmented TEG, two additional geometrical parameters, α_N and α_P, need to be defined to model the ratio of the n-type and p-type high-temperature material height to the overall leg height (H_{TE}). The operating conditions involve the density of heat flux into the thermoelectric generator (Q_{in}) and the electrical contact resistivities at the interface of the electrode and thermoelectric materials. Electrical contact resistivities between the top and bottom interfaces (ρ_{ct} and ρ_{cb}) are also included in the model as the operating conditions. In addition, several parameters are kept constant in the model. The insulation thickness (H_t) and the electrode thickness (H_{IC}) are both fixed at 0.5 mm. The entire device area (A_{TEG}) is fixed at 1 cm^2, and only one thermocouple is investigated. In addition, the cold side temperature T_c fixed at 293.15K and convectional heat flux on all concave internal surfaces with a heat transfer coefficient of 1 $mW/(cm^2 \cdot K)$ and external temperature of 293.15 K to include surface heat convection air. The next step is determining the parameters after deciding on the materials in STEG. The specific parameter ranges and resolutions for all variables are tabulated in Table 5.1.

TABLE 5.1: Ranges and resolutions of the parameters used in segmented TEG.

Geometrical Parameter	**Value Range**	**Resolution**
Height of the TEG leg (H_{TE})	0.5-5 mm	0.01mm
Filling Factor (FF)	0.05-0.95	0.01
High temperature n-type height ratio (α_N)	0.05-0.95	0.01
High temperature p-type height ratio (α_P)	0.05-0.95	0.01
Operating Condition	**Value Range**	**Resolution**
Top side contact resistivity (ρ_{ct})	$10^{-9} - 10^{-7}\Omega \cdot m^2$	$10^{-9}\Omega \cdot m^2$
Bottom side contact resistivity (ρ_{cb})	$10^{-9} - 10^{-7}\Omega \cdot m^2$	$10^{-9}\Omega \cdot m^2$
Heat flux (Q_{in})	$100 - 2000mW/cm^2$	$1mW/cm^2$

The electrical terminal was connected directly to a load resistance for each simulation and swept from 1/100 to 100 times the estimated internal resistance shown in Figure 5.3. The output power in all the datasets is the maximum power obtained by fitting the parabola, referred to as PD_{max}.

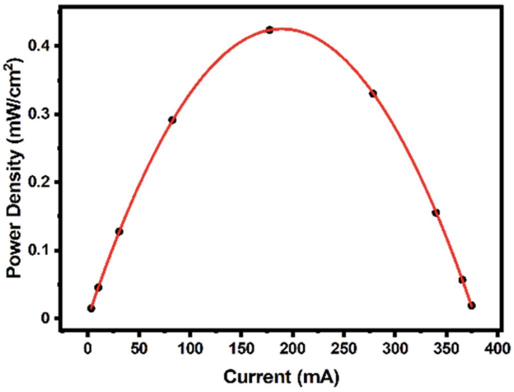

FIGURE 5.3: Power density values from COMSOL simulation (dots) and parabolic fitting (line) of a typical TEG as a function of currents by varying the load resistance under constant heat flux.

The impact of mesh sizes in the STEG model on the simulation accuracy was evaluated by simulating the same parameter set with different meshes, as shown in Figure 5.4. The "Fine" mesh size with 8012 elements has been employed for all simulations in this segmented TEG modelling due to its high accuracy and reasonable computation time shown in Figure 5.4. The maximum element size is 1.13mm, and the minimum element size is 0.141mm. And the maximum element growth rate is 1.45.

5.1.2 ANN configuration and dataset distribution

The structure of the ANN in this work is shown in Figure 5.5. The network contains an input layer that includes four design parameters (H_{TE},FF,α_N,α_P) and three operating

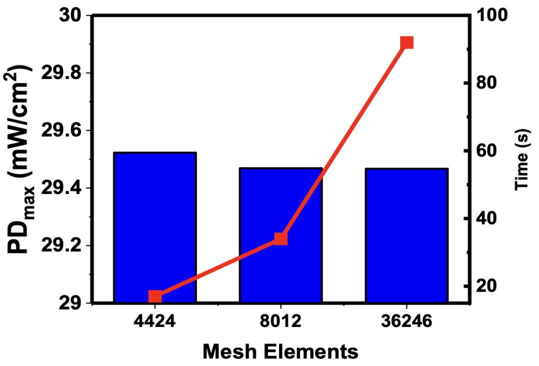

FIGURE 5.4: Power density (blue) and time (red) of the COMSOL simulation performed at different mesh elements

conditions (ρ_{ct},ρ_{cb},Q_{in}), as well as an output layer containing the STEG power performance (PD_{max}). There are five hidden layers between the input and output layers, with 200 neurons per layer. Then, a 3000 dataset for STEG is generated.

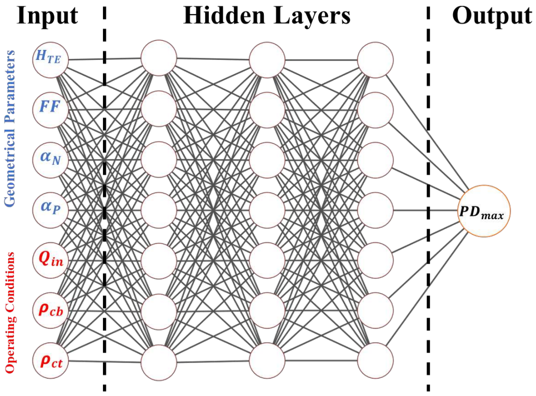

FIGURE 5.5: The architecture of the forward modelling ANN for predicting the power density of the STEG model. The input layer contains design parameters (H_{TE},FF,α_N,α_P) and operating conditions (ρ_{ct},ρ_{cb},Q_{in}). The output layer contains power performance values (PD_{max})

5.1.3 Genetic algorithm

After generating the dataset following the process described above, the ANN was trained. The method for combining the ANN with the GA will be discussed later. The process of the genetic algorithm is similar to that of conventional bulk TEG. Figure 5.6 shows the flow chart of GA used in this chapter. The operating condition has changed since the parameter is different. Other settings are kept the same. 100 population with 200 generations to calculate the optimized data. Tournament selection is chosen, and 1% of the mutation rate is adopted in the GA. All codes of ANN training and GA can be found in the Appendix.

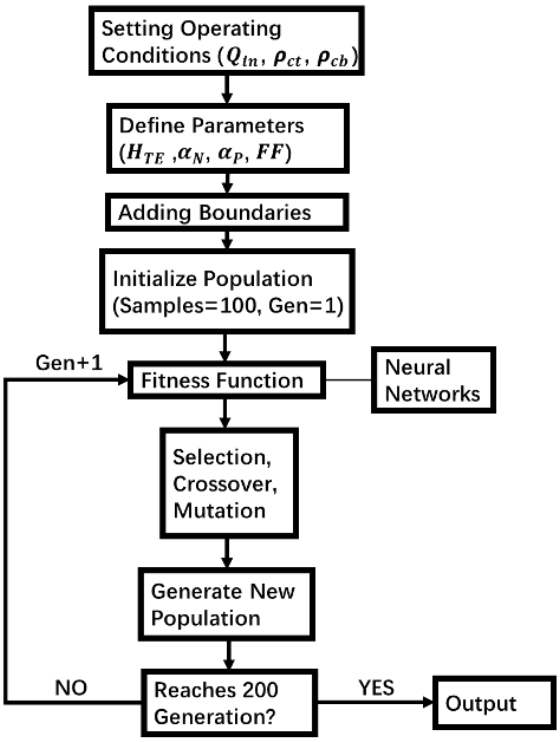

FIGURE 5.6: Flowchart of segmented TEG modelling genetic algorithm.

5.2 Iterative training

The iterative training process in our work is presented in Figure 5.7. An ANN was first trained using a dataset containing 3000 uniformly distributed input data, called Uni_{3000}. The details of the ANN training process are the same as those in the previous chapter. The traditional ANN modelling approach trains a dataset into an ANN. In this chapter, an iterative algorithm is employed, complemented by a conventional algorithm, to serve as a reference for modelling.

The ANN Uni_{3000} was coupled with a genetic algorithm (GA) to identify the high-performing STEG designs at different operating conditions. The corresponding STEG designs with the best performances can be obtained by generating 1000 different operating conditions based on Table 5.1. The 1000 sets of data were first generated by writing Python code to randomly create 1000 sets of operating conditions datasets. Then, Uni_{3000} was combined with GA, using these 1000 datasets to obtain the optimized 1000 sets of geometrical parameters. This provided a complete set of 1000 input datasets. These input parameters were then imported into COMSOL, and the final simulation yielded 1000 output datasets. This set of 1000 datasets is intended to add more optimized results to the overall data.

It is important to note that obtaining the Uni_{3000} network is essential in this iterative training process. It enables fast modelling of the STEG power performance, which significantly reduces the GA optimization time [34]. For example, an average of 40s is required for ANN-assisted GA optimization, while it costs 60000s if COMSOL modelling is used instead as shown in Table 5.2 and Table 5.3.

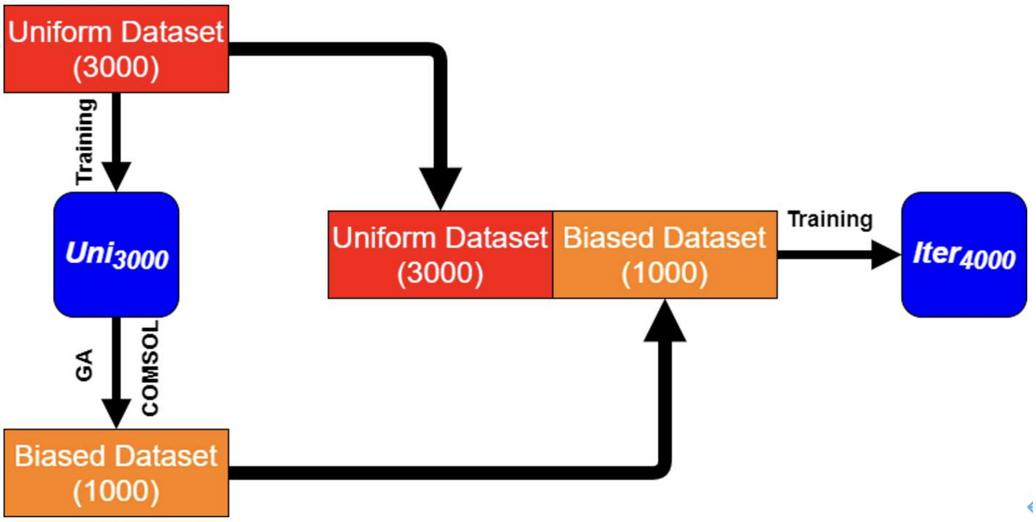

FIGURE 5.7: Iterative ANN training process flowchart.

The dataset generated by the genetic algorithm was found to have unique characteristics. With comparison, a 1000-uniform dataset was generated by first randomly selecting the input parameters (with both operating conditions and geometrical parameters). Then, the input dataset is simulated in the COMSOL for the output. It was not conformed to have a uniform distribution as shown in Figure 5.8 and is therefore referred to as the biased dataset. This different distribution is mainly due to the fact that many structural parameters are not needed in the optimization, especially the share of high-temperature materials in the different material ratios. This is because, even at higher temperatures, room-temperature materials are needed to increase efficiency when the lower surface temperature is fixed at 293.15K. This highly non-uniform dataset represents STEG designs with high power performance. For example, the larger H_{TE} and smaller FF are favourable for achieving high power outputs (Figure 5.8a and b). This trend is likely to be linked to the thermal conductance of the TE legs. Longer and smaller legs can result in a more significant temperature difference across the TE materials under the constant heat flux condition. Similarly, α_N and α_P also demonstrate biased distributions corresponding to the high-power STEG designs. Even though this dataset will include some high-power performance designs that are unusable, adding such a biased dataset will still help increase the proportion of these designs in the dataset.

As mentioned before, the iteration process requires the generation of a biased dataset based on the previous neural network to train a new ANN. After obtaining the biased dataset, a new dataset containing the original 3000 uniform data and this 1000 biased data was produced and used to train the new ANN (referred to as $Iter_{4000}$). To better

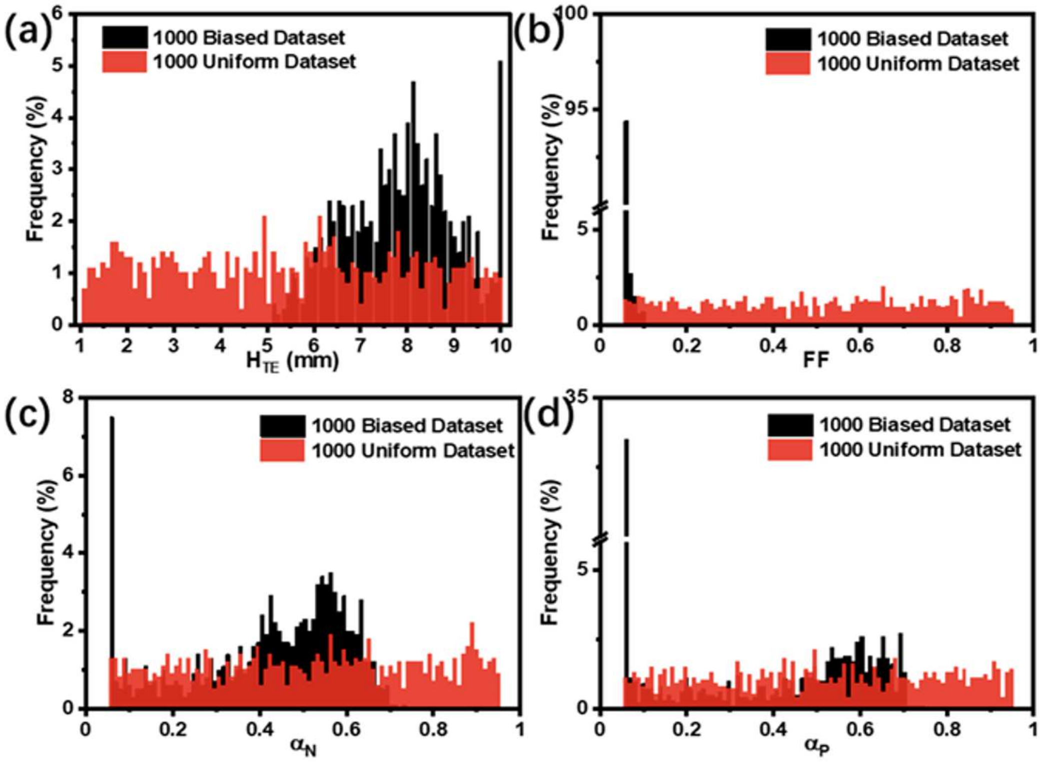

FIGURE 5.8: Distribution of the design parameters (a) H_{TE}, (b) FF, (c) α_N, (d) α_P in the 1000 uniform datasets (red) and biased datasets (black).

evaluate the performance of this $Iter_{4000}$ network, a separate ANN was prepared using a uniform dataset containing the same number of 4000 data (referred to as Uni_{4000}). The validation and test datasets in training two ANNs were the same dataset during the training process.

5.3 Evaluation of two ANN training processes

The prediction performance of the ANNs will first be evaluated using a uniform test dataset and a biased test dataset. The uniform test dataset contains randomly selected operating conditions and STEG designs. Furthermore, a biased test dataset is generated from $Iter_{4000}$ coupled with GA. The uniform and biased test dataset distribution are similar to those in Figure 5.8 and are presented in Figure 5.9.

The relative error was defined for comparison to better demonstrate the prediction performance. The relative error is defined as:

$$RelativeError = \frac{|P_{COMSOL} - P_{ANN}|}{P_{COMSOL}} \tag{5.1}$$

where P_{COMSOL} the true maximum power density obtained from COMSOL simulation while P_{ANN} is that predicted by the ANN. On this basis, the prediction accuracy can be

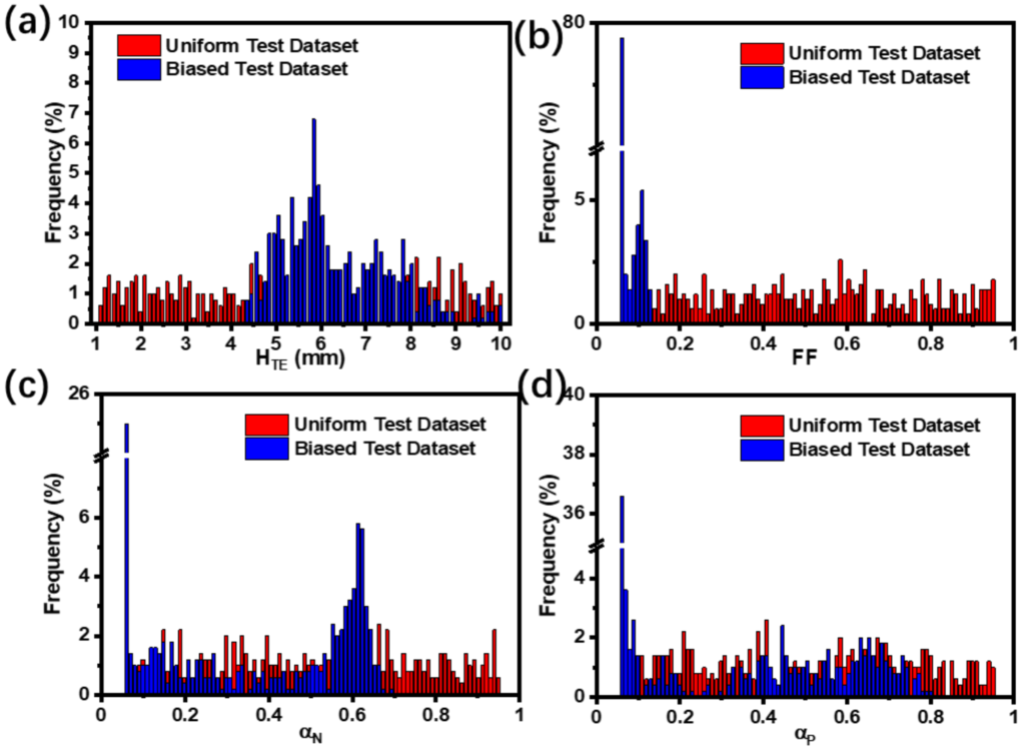

FIGURE 5.9: Comparison of geometric parameters (a) H_{TE}, (b) FF, (c) α_N, (d) α_P distributions for uniform test datasets (red) and bias test datasets (blue).

calculated as:

$$PredictionAccuracy = (1 - RelativeError) \times 100\% \tag{5.2}$$

Figure 5.10 shows the performance of the two ANNs (Uni_{4000} and $Iter_{4000}$) with a uniform test dataset and biased dataset. Figure 5.10a presents the distribution and average relative error for the Uni_{4000} and $Iter_{4000}$ ANNs on the uniform test dataset. Both networks demonstrate a deficient relative error of 0.021 and 0.024, corresponding to a high prediction accuracy of 97.9% for Uni_{4000} and 97.6% for $Iter_{4000}$. It is further confirmed by plotting the true PD_{max} (from simulation) in the uniform test set against the predicted PD_{max} by Uni_{4000} and $Iter_{4000}$, respectively (shown in Figure 5.10b and c). It can be observed that the high prediction accuracy of our ANN prevails over the entire power range, producing a high coefficient of determination value (R^2) of over 0.999 for both networks. The slightly higher accuracy for Uni_{4000} can be explained by the extra 1000 uniform datasets used in its training process. However, such a slight difference suggests our $Iter_{4000}$ ANN can also provide accurate predictions for random STEG designs.

The prediction accuracy of the iterative ANN and the uniform ANN in STEG design optimization will now be evaluated by coupling them with GA. GA optimization with

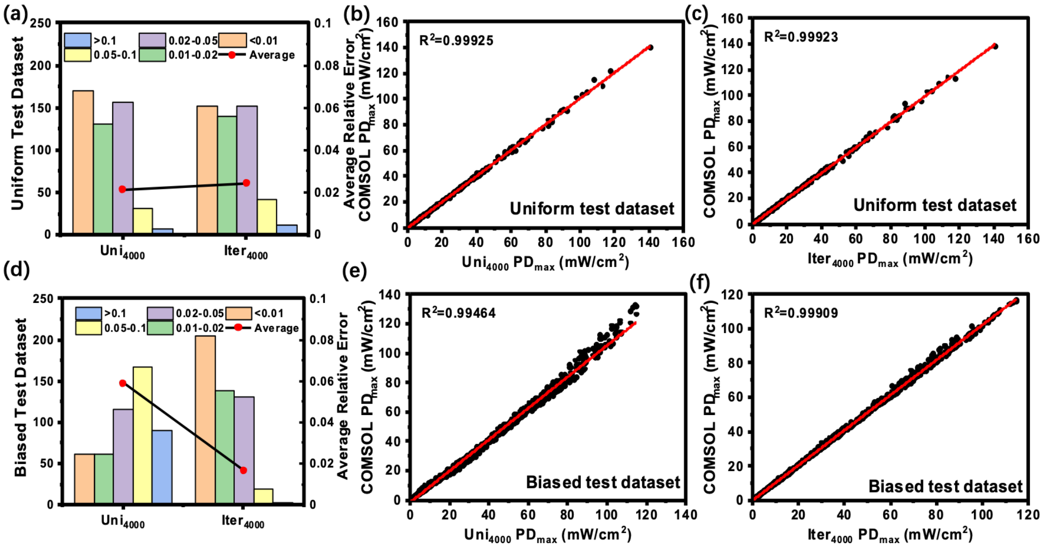

FIGURE 5.10: Comparison of COMSOL output PD_{max} for two different ANNs (a) the histogram of the probability and average relative errors of two ANNs on the uniform test dataset, and (b) Uni_{4000}, (c) $Iter_{4000}$ on the uniform test dataset. Comparison of COMSOL output PD_{max} for two different ANNs (d) the histogram of the probability and average relative errors of two ANNs on the biased test dataset, and (e) Uni_{4000}, (f) $Iter_{4000}$ on the biased test dataset.

COMSOL as the alternative forward modeller is conducted to obtain the genuinely optimized design and power performance as a reference. Figure 5.11a presents the GA optimized PD_{max} under different heat flux conditions by coupling with COMSOL (black), Uni_{4000} (red) and $Iter_{4000}$ (blue). The optimized design parameters from each approach are listed in Table 5.2 and Table 5.3. It can be observed that the $Iter_{4000}$ optimized values are closer to the COMSOL optimized values than the values optimized by Uni_{4000}. The relative errors of the two different ANNs (Uni_{4000}, $Iter_{4000}$) were calculated based on the optimal PD_{max} from the COMSOL simulation-assisted GA optimization.

Figure 5.11b shows the relative errors of the optimized PD_{max} for the Uni_{4000} ANN (red bar) and $Iter_{4000}$ ANN (blue bar). The relative error for Uni_{4000} ANN increases significantly from 0.02 to over 0.1 when the input heat flux increases from $200 mW/cm^2$ to 1500 mW/cm^2. Given that more considerable heat flux is more likely to produce a large PD_{max}, the poor performance of Uni_{4000} ANN is likely due to the limited high-power performance data in the uniform training dataset. On the contrary, the relative error for $Iter_{4000}$ ANN is significantly smaller and remains below 0.02 for all heat flux conditions. Similarly, it also outperforms the Uni_{4000} ANN under various contact resistivity conditions, as shown in Figure 5.11c and Figure 5.11d. Overall, the average relative error for $Iter_{4000}$ ANN over the ten different operating conditions is 0.01, indicating an accuracy of over 99%. This accuracy suggests our $Iter_{4000}$ ANN can sufficiently replace COMSOL simulation for STEG optimization and further confirms the benefit of our iterative ANN approach. However, the average optimization time for ANN-coupled GA is only ca. 6.3 s while over 35,000 s (ca. 10 hours) for COMSOL-coupled GA under the same computational environment. This speed saves computational time and resources over 5,000 times as shown in Table 5.2 and Table 5.3.

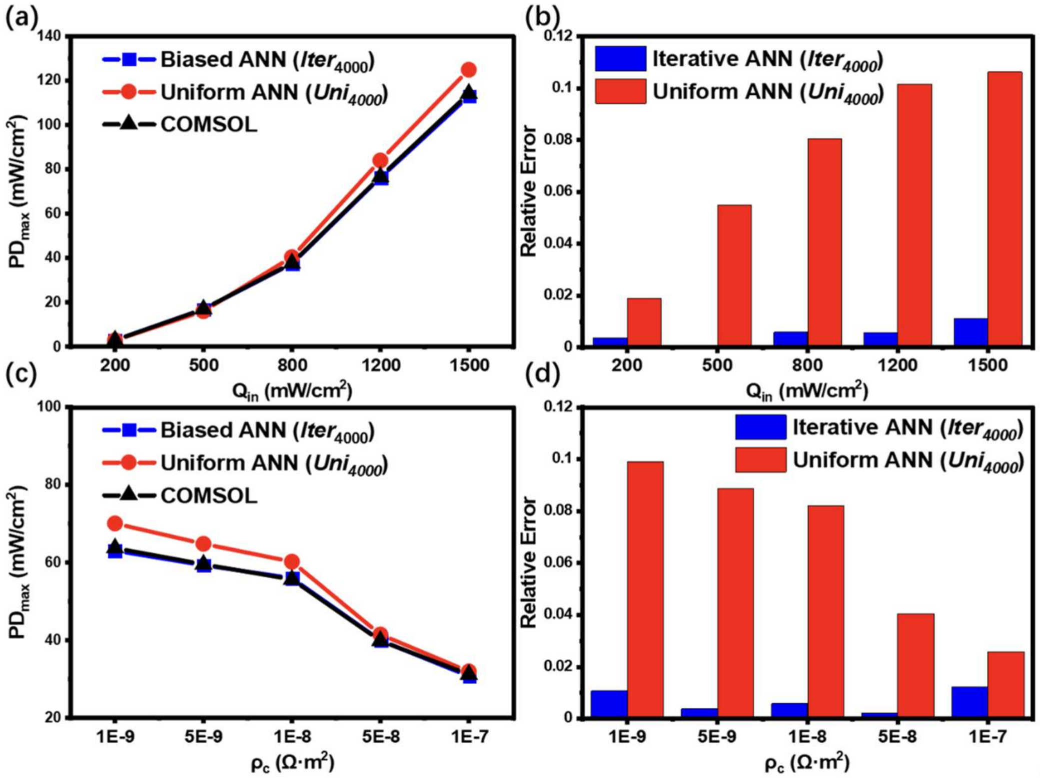

FIGURE 5.11: Genetic algorithm optimized STEG PD_{max} using ANN $Iter_{4000}$ (blue), uniform ANN Uni_{4000} (red), and COMSOL simulation as forwarding modellers (a), and the associated relative errors from $Iter_{4000}$ (blue) and Uni_{4000} (red) compared with the COMSOL (b) as a function of different Q_{in}; Genetic algorithm optimized STEG PD_{max} using ANN $Iter_{4000}$ (blue), uniform ANN Uni_{4000} (red), and COMSOL simulation as forwarding modellers (c), and the associated relative errors from $Iter_{4000}$ (blue) and Uni_{4000} (red) compared with the COMSOL (d) as a function of different ρ_c.

TABLE 5.2: The optimized design parameters from each approach at a different heat flux density

Model	Time (s)	H_{TE} (mm)	FF	α_N	α_P	ρ_c $(\Omega \cdot m^2)$	Q_{in} (mW/cm^2)	PD_{max} (mW/cm^2)
COMSOL	35458.59	5.43	0.05	0.05	0.05	1.00E-08	200	2.86036
$Iter_{4000}$	6.52	5.55	0.05	0.11	0.05	1.00E-08	200	2.84945
Uni_{4000}	6.7	7.18	0.05	0.05	0.05	1.00E-08	200	2.80587
COMSOL	36392.49	4.81	0.05	0.05	0.05	1.00E-08	500	16.86888
$Iter_{4000}$	6.43	5.5	0.05	0.05	0.05	1.00E-08	500	16.8742
Uni_{4000}	6.38	5.34	0.05	0.33	0.16	1.00E-08	500	15.94478
COMSOL	39909.52	5.14	0.05	0.37	0.23	1.00E-08	800	37.35331
$Iter_{4000}$	6.45	5.24	0.05	0.3	0.08	1.00E-08	800	37.57173
Uni_{4000}	6.33	4.79	0.05	0.48	0.15	1.00E-08	800	40.3621
COMSOL	65782.16	5.06	0.05	0.56	0.54	1.00E-08	1200	76.21577
$Iter_{4000}$	6.36	5.37	0.05	0.56	0.55	1.00E-08	1200	76.64584
Uni_{4000}	6.49	6.33	0.05	0.6	0.62	1.00E-08	1200	83.96727
COMSOL	56433.89	6.33	0.05	0.6	0.62	1.00E-08	1500	112.94648
$Iter_{4000}$	6.17	5.81	0.05	0.64	0.65	1.00E-08	1500	114.21274
Uni_{4000}	6.62	5.82	0.05	0.61	0.71	1.00E-08	1500	124.953

TABLE 5.3: The optimized design parameters from each approach at different contact resistivity

Model	Time (s)	H_{TE} (mm)	FF	α_N	α_P	ρ_c ($\Omega \cdot m^2$)	Q_{in} (mW/cm^2)	PD_{max} (mW/cm^2)
COMSOL	41179	4.18	0.05	0.46	0.32	1.00E-09	1000	63.7304
$Iter_{4000}$	6.29	4.34	0.05	0.48	0.33	1.00E-09	1000	63.04789
Uni_{4000}	6.21	5.74	0.05	0.57	0.47	1.00E-09	1000	70.04938
COMSOL	40804.14	4.83	0.05	0.48	0.39	5.00E-09	1000	59.5208
$Iter_{4000}$	6.23	5.11	0.05	0.52	0.39	5.00E-09	1000	59.29213
Uni_{4000}	6.36	5.85	0.05	0.59	0.46	5.00E-09	1000	64.86143
COMSOL	40882.22	5.35	0.05	0.49	0.42	1.00E-08	1000	55.63124
$Iter_{4000}$	6.3	6.26	0.05	0.64	0.34	1.00E-08	1000	55.95702
Uni_{4000}	6.29	5.9	0.05	0.58	0.48	1.00E-08	1000	60.20184
COMSOL	61298.28	8.29	0.06	0.46	0.43	5.00E-08	1000	39.85245
$Iter_{4000}$	6.33	7.6	0.05	0.41	0.49	5.00E-08	1000	39.93462
Uni_{4000}	6.34	9.28	0.05	0.52	0.36	5.00E-08	1000	41.46385
COMSOL	79482.72	10	0.06	0.44	0.43	1.00E-07	1000	31.14841
$Iter_{4000}$	6.22	10	0.05	0.52	0.57	1.00E-07	1000	30.76607
Uni_{4000}	6.27	9.97	0.05	0.43	0.51	1.00E-07	1000	31.95072

5.4 Segmented TEG analysis using iterative ANN

The advantages of STEG modelling through iterative ANN have been established, where its high prediction accuracy and speed ensure fast and accurate design optimization. Such benefits also allow rapid generation of accurate parameter-performance data that are otherwise difficult to obtain through conventional modelling approaches. This large amount of data could contribute to the in-depth study of the STEG and unveil relations that have not been investigated before due to the complexity of the STEG structure. As an example, Figure 5.12a presents the PD_{max} values as a function of H_{TE} and FF, where other parameters and conditions remain constant. The lines are the output of iterative ANN, and the triangles are the corresponding COMSOL simulation results. The PD_{max} increases progressively with increasing H_{TE} and decreasing FF, which could be understood as these leading to the rise of the TE leg thermal resistance and consequently resulting in a more significant temperature difference across the device. The benefit of a more substantial temperature difference outweighs the simultaneously increased electrical resistance, which is likely dominated by the contact resistance.

Figure 5.12b demonstrates the dependence on different heat fluxes. As can be seen in Figure 5.12b, the output PD_{max} increases as FF decreases when Q_{in} is relatively tiny. This is because the temperature difference between the two ends of the STEG is not very significant. Hence, the benefit of the increase in thermal resistance outweighs the loss due to the rise in resistance. When Q_{in}=2000 mW/cm^2, on the other hand, the output increases and decreases with decreasing FF. Since the energy from Q_{in} is so great, the temperature difference between the two ends of the STEG reaches the optimum operating region for high-temperature materials when the FF is reduced to around 0.1. The thermal resistance increase caused by continuing to minimize FF does not exceed the losses caused by the electrical resistance at this point, so the output

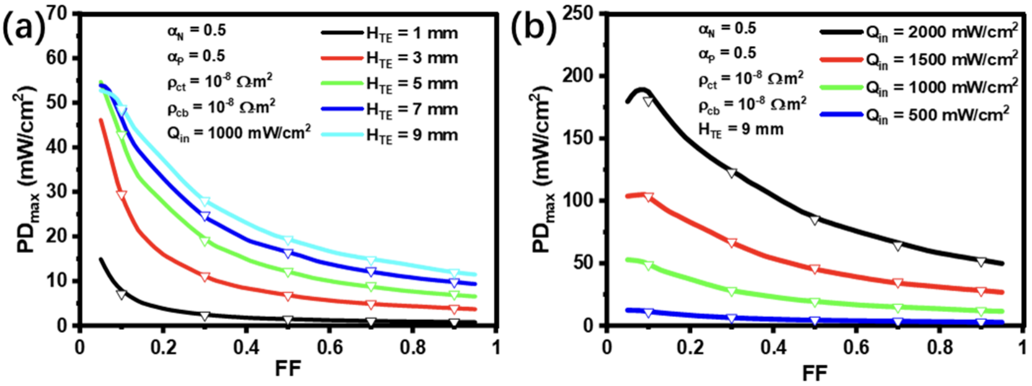

FIGURE 5.12: PD_{max} obtained from iterative ANN (line) and COMSOL simulation (triangles) as a function of (a) H_{TE} and FF, (b) Q_{in}, and FF.

PD_{max} is decreased. The triangles in Figure 5.12 represent the results of the COMSOL simulation, which indicates that the values predicted by the $Iter_{4000}$ are very close to the actual data and further validates the accuracy of the $Iter_{4000}$ model.

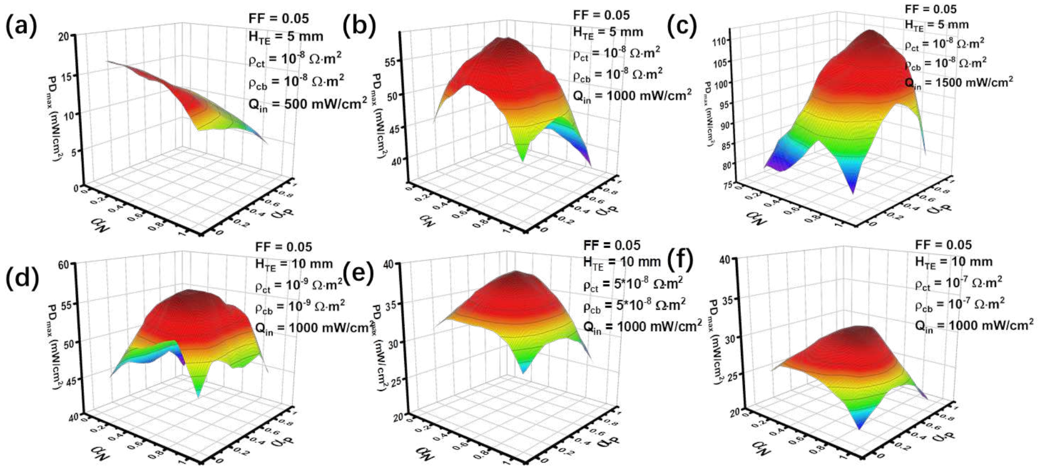

FIGURE 5.13: PD_{max} of iterative ANN obtained by scanning α_N and α_P at different heat flux Q_{in} conditions of (a) 500 mW/cm^2, (b) 1000 mW/cm^2, (c) 1500 mW/cm^2 with other parameters fixed; PD_{max} of iterative ANN obtained by scanning α_N and α_P at different electrical conductivity ($\rho_{ct} = \rho_{cb}$) conditions (d) $10^{-9}\Omega \cdot m^2$, (e)$10^{-8}\Omega \cdot m^2$, (f)$10^{-7}\Omega \cdot m^2$.

The relationships between the design parameters are complex when multiple parameters (e.g., α_N and α_P) vary simultaneously. Taking advantage of the ultra-fast computing speed, the PD_{max} was thoroughly mapped under different α_N and α_P combinations. Figure 5.13 shows the PD_{max} of the biased ANN obtained by scanning α_N and α_P. Figure 5.13a to c present the predicted PD_{max} mapping under the heat flux of 500, 1000, and 1500 mW/cm^2, respectively. It can be observed that when the Q_{in} is increased, the peak PD_{max} will be shifted to larger α_N and α_P values to include more high-temperature material in the STEG design. Similarly, under different contact resistivity conditions, the impact of α_N and α_P values on PD_{max} is similar as shown in Figure 5.13d to f. However, as the contact resistance increases, the output power decreases significantly. As seen from the Figure 5.13, the two parameters α_N and α_P interact with each other, and this non-linearity is easily represented in the ANN model. Additionally, the impact on the output power varies with different parameters. A quick calculation using the ANN makes it easy to compute the bias derivatives of various parameters and to determine the effect of different parameters on the output power under the present conditions. Our iterative ANN can generate similar mappings over other design parameters and operating conditions. Each mapping contains 9216 (96 × 96) modelling results and could take over 500,000 s (6 days) for COMSOL to simulate. Applying our iterative ANN will only take 3s under the same computational environment, representing over 100,000 times efficiency improvement. Even adding the dataset preparation time it is also 2 times faster than COMSOL simulation. Moreover, this advantage will increase with more frequent use of the ANN.

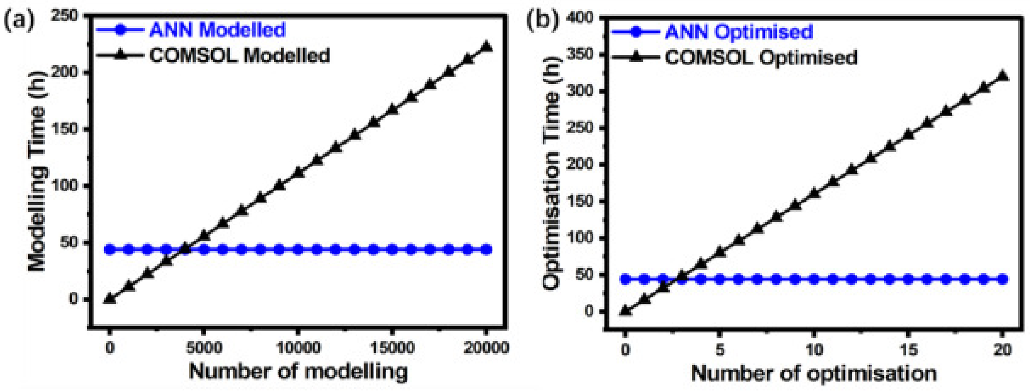

FIGURE 5.14: The required computational time as a function of (a) the number of modelling and (b) the number of optimization for ANN (blue) and COMSOL (black).

Figure 5.14 shows the time required for both methods to perform multiple modelling and GA optimizations under the same computation conditions. The training time of the ANN is considered in this comparison. The amount of time saved by using ANN easily recovers the up-front computational time for the network when more than 4000 modelling is required (Figure 5.14a) or more than 2 GA optimizations are needed (Figure 5.14b). This manifests the extremely high computational efficiency of our ANN approach.

5.5 Conclusion

In this chapter, an artificial neural network is used to report the forward power performance modelling for the segmented thermoelectric generator. After training using a dataset from 3-D COMSOL simulations, the neural network can predict the power performance under varying heat flux conditions from different design parameters. Moreover, the electrical contact resistance, surface heat transfer, and other thermoelectric effects can still be considered. An iterative training strategy was implemented to improve the prediction accuracy of the high-power performance STEG designs without increasing the training dataset size. This prediction accuracy of the iterative trained artificial neural network increases from 94% to over 98% without requiring a larger dataset. This high accuracy is essential to ensure the correct STEG design optimization results.

In addition to superior accuracy, the neural network demonstrates extremely high efficiency, which is beneficial for fast design optimization and parameter dependence analysis. Coupled with a genetic algorithm, the network can achieve one design optimization for 6.3 s, 5000 times faster than COMSOL, but with almost identical optimized values as shown in Table 5.2 and Table 5.3. Large parameter scans have also revealed the relationship between the STEG power output and the segment material ratios. Only 3 s is required for the network to conduct a parametric scan containing 9216 data points, representing over 100,000 times of efficiency improvement.

Chapter 6

Radiative Cooling Coupled TEG modelling

While the previous chapters focused on the thermoelectric generator alone, this chapter shifts the focus to the hybrid thermoelectric generator system with radiative cooling. The aim is to investigate the performance of the system when radiative cooling is used as a cold end for the thermoelectric generator. This chapter presents an in-depth analysis of the performance of radiative cooling thermoelectric generators (RC-TEG) utilizing a 3D finite element analysis (FEA) modelling approach. The 3D FEA method allows for more accurate modelling by incorporating various factors, including RC performance, TEG design, and environmental aspects such as atmospheric emissivity and air convection. These parameters are systematically examined to provide a comprehensive understanding of RC-TEG performance. Additionally, the power generation capabilities of the RC-TEG are assessed using real-time solar irradiance and ambient temperature data from different cities, enabling an evaluation of its effectiveness in various geographic regions.

This chapter has been published as Yuxiao Zhu, Daniel W. Newbrook, C.H. Kees de Groot, Ruomeng Huang, Comprehensive analysis of radiative cooling enabled thermoelectric energy harvesting, JPhys Photonics, vol. 5, 2023, doi: `10.1088/2515-7647/accac1`. As the first author, my contributions include building the COMSOL model, performing the parameter sweep for COMSOL and writing the paper. Daniel provided the thermoelectric material parameters. Kees reviewed the paper, and Ruomeng reviewed the paper and supervised the project.

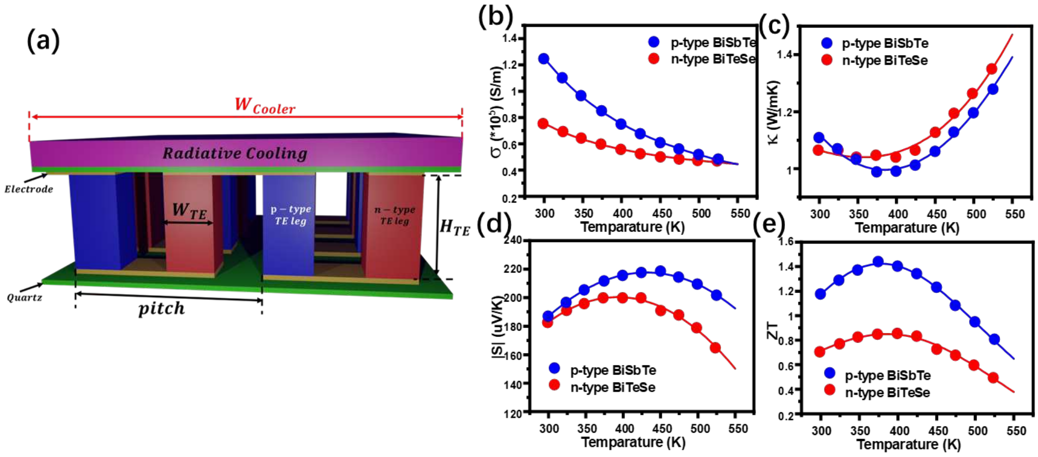

FIGURE 6.1: Schematic and temperature-dependent material properties of the n-type and p-type thermoelectric materials used in our RC-TEG model. (a) schematic, (b) Electrical conductivity (σ), (c) Thermal conductivity (k), (d) Seebeck coefficient (S), and (e) figure of merit (ZT)[45] [164].

6.1 Details of the RC-TEG model

Figure 6.1a shows the model of the RC-TEG developed in COMSOL in this work. A square radiative cooler with a width of W_{Cooler} is integrated on the top surface of the TEG model. It is exposed to the sky directly in the simulation. An insulating layer (quartz glass) of the same size is sandwiched between the radiative cooler and TEG. The bulk TEG model contains eight N/P-leg pairs where the width and height of both legs are kept the same as W_{TE} and H_{TE}, respectively, in this chapter. The N/P legs are connected in series by copper interconnects. The electrical contact resistance is also considered in the model by including a $10^{-8}\Omega \cdot m^2$ contact resistivity at each copper/TE leg interface. The top and bottom convection coefficient is defined as $Conv_T$ and $Conv_B$, respectively. The specific modelling files can be found in the Appendix links.

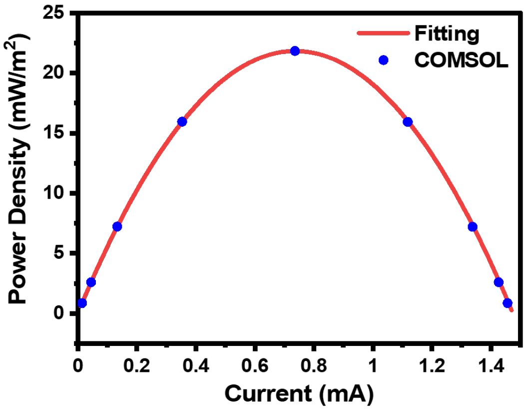

FIGURE 6.2: Power density values from COMSOL simulation (dots) and parabolic fitting (line) of a typical TEG as a function of currents by varying the load resistance.

The thermoelectric materials used in this work are $Bi_2Te_{2.7}Se_{0.3}$ for the n-type leg and $Bi_{0.5}Sb_{1.5}Te_3$ for the p-type leg. The detailed thermoelectric properties, such as the Seebeck coefficient, electrical and thermal conductivities, and ZT values of both materials, are adopted from past studies [45] [164] and presented in Figure 6.1b-e. The ambient temperature is set at 293.15K as default in all simulations unless otherwise specified. During simulation, the TEG is virtually connected with an external load to form a circuit. The inlet and outlet of the copper interconnect serve as a terminal (variable V) and the ground (V = 0 V) for the model. The resistance of the external load is swept to reach the maximum power density (PD_{max}), as exemplified in Figure 6.2. The specific parameters are shown in Table 6.1. The different ranges for the top and bottom surfaces in the table are based on theoretical analyses. For the cooled top surface, convection needs to be minimized to lower the temperature. For the bottom surface, the aim is to keep it as close as possible to the ambient temperature to allow the TEG to achieve the maximum temperature difference.

TABLE 6.1: Ranges and resolutions of the parameters used in segmented TEG.

TEG Parameter	**Value Range**	**Resolution**
Width of the TEG leg (W_{TE})	1-10 mm	1 mm
Height of the TEG leg (H_{TE})	1-30 mm	1 mm
Width of the radiative cooling (W_{Cooler})	20-200 mm	1 mm
Pitch	2-30 mm	1 mm
Top surface convection ($Conv_T$)	0-10 $W/(m^2K)$	1 $W/(m^2K)$
Bottom surface convection ($Conv_B$)	10-100 $W/(m^2K)$	5 $W/(m^2K)$
Radiative Cooling Parameter	**Value Range**	**Resolution**
Average emissivity of 8-13 μm ($\varepsilon_{8-13\mu m}$)	0-1	0.05
Average emissivity of 0.3-2.5 μm ($\varepsilon_{0.3-2.5\mu m}$)	0-1	0.05

This chapter will focus mainly on the emissivity in the solar band ($0.3-2.5\mu m$) and the radiation band ($8-13\mu m$). The emissivity of the band ($2.5-8\mu m$) is fixed at 0 unless otherwise specified. The solar irradiance is set to $1000W/m^2$ in the simulation unless otherwise specified. In practice, it is possible to accurately calculate the emissivity of each band using a multilayer structure to achieve the assumed data.

When exposing the radiative cooler to the sky, the temperature of the top surface will drop, creating a temperature difference ΔT between the top and bottom surfaces. However, the temperature is not uniformly distributed on both surfaces due to the direct contact with the TEG. For example, Figure 6.3 presents the temperature profiles on both surfaces under one simulation condition. It is clear that the temperature directly on top of a TEG leg is slightly higher on the top (cold) surface than the surrounding areas (Figure 6.3a). On the contrary, the temperature directly below a TEG is slightly colder on the bottom (hot) surface than its surroundings (Figure 6.3b).

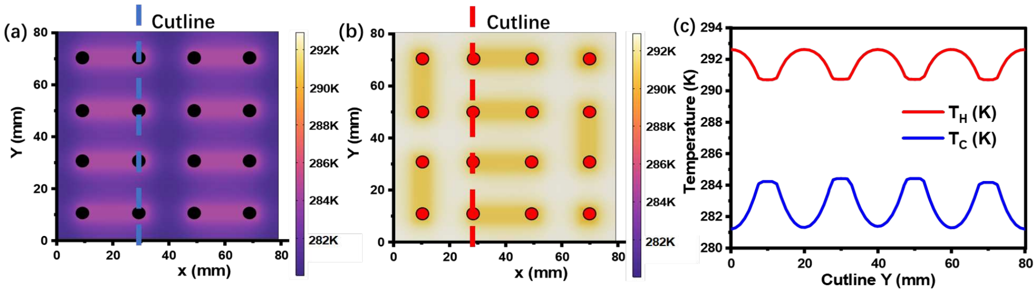

FIGURE 6.3: Temperature profile of the RC-TEG under typical working conditions. (a) exposed radiative surface (b) shielded counter surface. The dots represent the locations where the average temperature readings are used to define T_C and T_H. (c) The temperature distribution at the cutlines in (a) and (b).

In this chapter, we define the top side (hot) temperature T_H as the average temperature of the 16 points above the TEG legs and the bottom (cold) side temperature T_C as the average temperature of the 16 points below the TEG legs. The temperature difference is ΔT, defined as $\Delta T = T_H - T_C$. This provides us with a better understanding of the actual temperature gradients over the TEG as the distribution of the temperature is not uniform across the surfaces (Figure 6.3c). The non-uniformity is caused by the limited thermal conductivity of the insulating layer of quartz glass used between the cooler and the TEG used in this chapter.

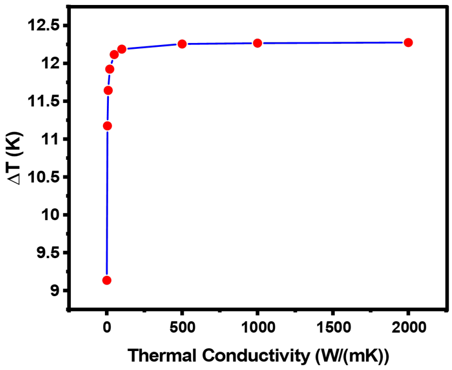

FIGURE 6.4: Temperature difference (ΔT) of RC-TEG as a function of the thermal conductivity of insulator.

We have conducted simulations concerning the impact of different thermal conductivity of the insulating material. Figure 6.4 is obtained by setting the thermal conductivity of ceramic materials as variables and then performing a parametric sweep. As shown in Figure 6.4, increasing the thermal conductivity results in higher ΔT. This increment saturates when the thermal conductivity reaches ca. $500 W/(mK)$. This suggests the uneven temperature distribution can be mitigated by adopting insulating layers with higher thermal conductivity, leading to a more uniform temperature profile and higher ΔT. In addition to the thermal conduction, the heat exchange of RC-TEG with the environment is also considered by defining the convection coefficient for both the top surface ($Conv_T$) and bottom surface ($Conv_B$). All simulations are carried out on the COMSOL platform with the thermal transfer process set as a steady-state condition.

6.2 RC-TEG performance under different convection

An RC-TEG functions when radiative cooling generates a temperature difference between the top and bottom surfaces. Heat exchange with the atmosphere through convection plays an essential role in the temperature profile of the RC-TEG.

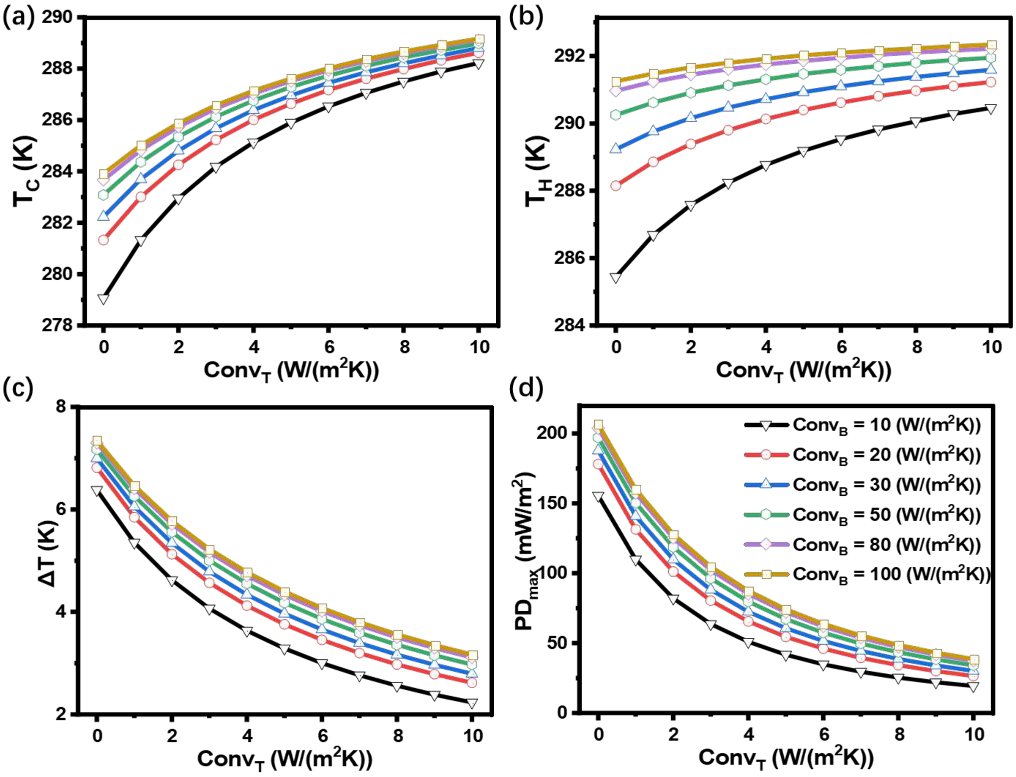

Figure 6.5: COMSOL simulation performance of RC-TEG under various top surface convection ($Conv_T$) and bottom surface convection ($Conv_B$) conditions. (a) Top (T_C) and (b) bottom (T_H) surface temperature, (c) The temperature difference between the top and bottom surface (ΔT), (d) the power density (PD_{max}),. Other simulation parameters were fixed at W_{Cooler} = 80 mm, W_{TE} = 5 mm, H_{TE} = 10 mm, and Pitch = 40 mm.

Figure 6.5a and b illustrate the variation of both T_C and T_H under different convection conditions. Both T_C and Th increase with increasing convection at both surfaces. This is unsurprising as the environmental temperature is set as 293.15K in this work. Higher convection will facilitate the heat exchange between the RC-TEG and the atmosphere, leading to higher temperatures close to the environment. Achieving a more significant ΔT, therefore, requires different convection conditions for each surface, as shown in Figure 6.5c. Convection at the top surface should be minimised to retain the low temperature generated by radiative cooling while the convection at the bottom surface should be promoted. In this set of simulations, the largest ΔT of 7.3K is obtained when $Conv_T$ is as low as 1 $W/(m^2K)$ while $Conv_B$ is 100 $W/(m^2K)$. It is also evident that the impact of $Conv_T$ is much more significant than $Conv_B$, with ΔT quickly deteriorating to 3.5 K when $Conv_T$ increases to 10 $W/(m^2K)$. The associated power performance of RC-TEG is shown in Figure 6.5d. As expected, the higher power output takes place at the largest ΔT, reaching over 200 mW/m^2. However, such high power output would be halved if the $Conv_T$ increases from 1 $W/(m^2K)$ to 4 $W/(m^2K)$. At a $Conv_T$ of 10 $W/(m^2K)$, the output power will drop to below 50 mW/m^2. It is, therefore, key for RC-TEG to keep good thermal insulation to the environment to minimise heat exchange. Several experimental RC-TEG works to achieve that by enclosing the radiative cooler within a vacuum chamber [167]. In the following simulations, we will set $Conv_T$ and $Conv_B$ to 1 $W/(m^2K)$ and 50 $W/(m^2K)$, respectively. It should be noted that the convection parameters on the bottom surface require forced convection or more complex cooling structures in practice to achieve this.

6.3 RC-TEG performance under different atmosphere emissivity

We will now investigate the impact of atmospheric emissivity on RC-TEG performance. The atmospheric emissivity depends on the concentration of water vapour, CO_2, CO and other gas in the air [168]. In particular, water vapour absorption dominates the atmospheric absorption within the atmospheric window; the transparency of the sky is sensitive to precipitable water vapour concentration, which is correlated with relative humidity and ground temperature, and thus varies geographically [169].

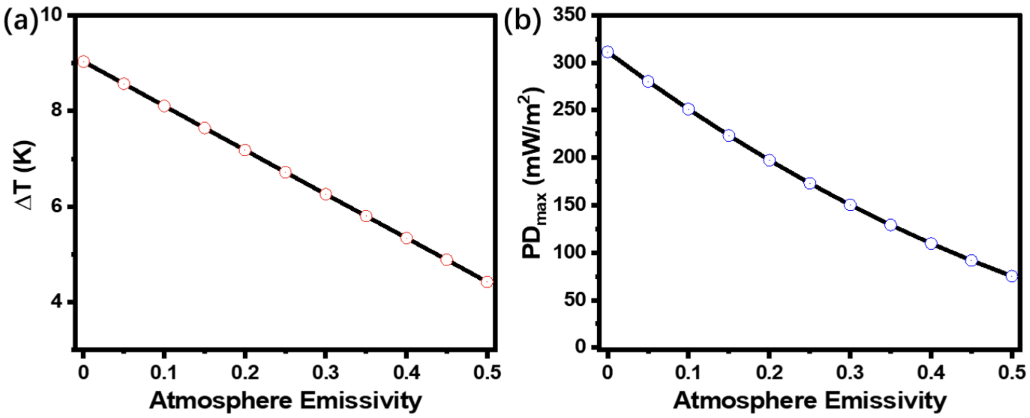

FIGURE 6.6: Performance of RC-TEG obtained in COMSOL simulation as a function of atmosphere emissivity (a) Temperature difference (ΔT) and (b) Power density (PD_{max}). Other simulation parameters were fixed at W_{Cooler} = 80 mm, W_{TE} = 5 mm, H_{TE} = 10 mm, and Pitch = 40 mm.

Higher humidity in the air could lead to high atmosphere emissivity in the 8-13 μm band, which directly affects RC-TEG performance. Figure 6.6 demonstrates the effect of atmospheric emissivity on the performance of RC-TEG. As the atmospheric emissivity increases from 0 to 0.5, the ΔT decreases by about 5 degrees. Such decrement is because more power is absorbed by the atmosphere rather than radiated to the colder outer space, leading to inferior power generation from the RC-TEG model. This trend proves that the RC-TEG performance is strongly dependent on the weather. Under a clear sky and dry atmosphere where the atmospheric emissivity is low (< 0.3), the RC-TEG model is capable of producing a continuous power of over 150 mW/m^2. However, this drops very quickly to below 100 mW/m^2 when the sky is overcast with high humidity. In subsequent model simulations, the atmospheric emissivity was maintained at 0.3 for all 8-13 μm and 1 for the other bands 0.3-8 μm and 13-25 μm.

6.4 RC-TEG performance under different radiative cooler emissivity

As an essential part of the RC-TEG, the emissivity (ε) of the radiative cooler is crucial to the power performance of the device. In this section, we mainly focused on studying the impact of emissivity in two bands of 0.3-2.5 μm and 8-13 μm. The former band decides how much solar energy is absorbed by the radiative cooler. This is especially important for daytime radiative cooling. The latter band in the atmospheric window of 8-13 μm determines the cooling power achieved by the radiative cooler.

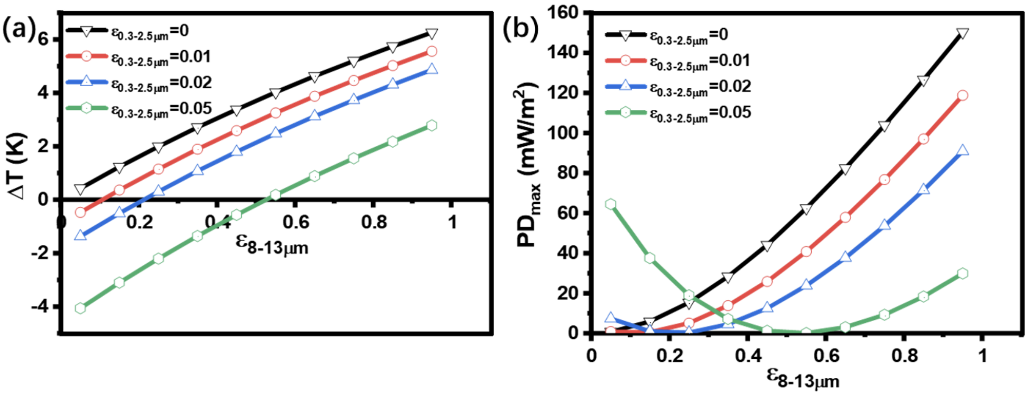

FIGURE 6.7: Performance of RC-TEG as a function of emissivity in the solar and thermal IR spectrum. (a) Temperature difference (ΔT) (b) Power density (PD_{max}) obtained from COMSOL simulation as a function of 8-13 μm ($\varepsilon_{8-13\mu m}$) and 0.3-2.5 μm ($\varepsilon_{0.3-2.5\mu m}$) surface emissivity. Other simulation parameters were fixed at W_{Cooler} = 80mm, W_{TE} = 5mm, H_{TE} = 10mm, and Pitch = 40mm.

Figure 6.7a presents the effect of surface emissivity on the temperature difference ΔT of an RC-TEG device in the daytime. A positive ΔT indicates that the top surface is colder than the bottom surface and that the cooling power dominates the temperature profile of our RC-TEG. A cooler with a larger $\varepsilon_{8-13\mu m}$ can generate more cooling power, leading to larger ΔT. However, positive ΔT only prevails when the $\varepsilon_{0.3-2.5\mu m}$ is maintained at a low level. Increasing $\varepsilon_{0.3-2.5\mu m}$ can result in the top surface being heated up by absorbing solar energy, cancelling out the positive ΔT from radiative cooling. When the heat absorbed from solar irradiation outweighs the heat dissipated via radiative cooling, the temperature difference ΔT becomes negative, and the radiative cooler effectively turns into a heat absorber.

The power performance of the RC-TEG under different surface emissivity scenarios is shown in Figure 6.7b. Under minor $\varepsilon_{0.3-2.5\mu m}$ conditions, the output power increases with increasing $\varepsilon_{8-13\mu m}$ values as the ΔT increases with more cooling power. However, in the case of a large $\varepsilon_{0.3-2.5\mu m}$ (e.g. 0.05), RC-TEG can also generate power even when $\varepsilon_{8-13\mu m}$ is small, except that the device is now operating as a solar-absorber TEG under such conditions. The amount of power attenuates to zero with increasing $\varepsilon_{8-13\mu m}$ value as the cooling power slowly cancels out the solar energy and rises again as the ΔT becomes positive. It is clear that $\varepsilon_{0.3-2.5\mu m}$ of the cooler needs to be as small as possible to avoid the negative influence of solar energy, while the $\varepsilon_{8-13\mu m}$ must be as large as possible to ensure a continuous power supply from RC-TEG.

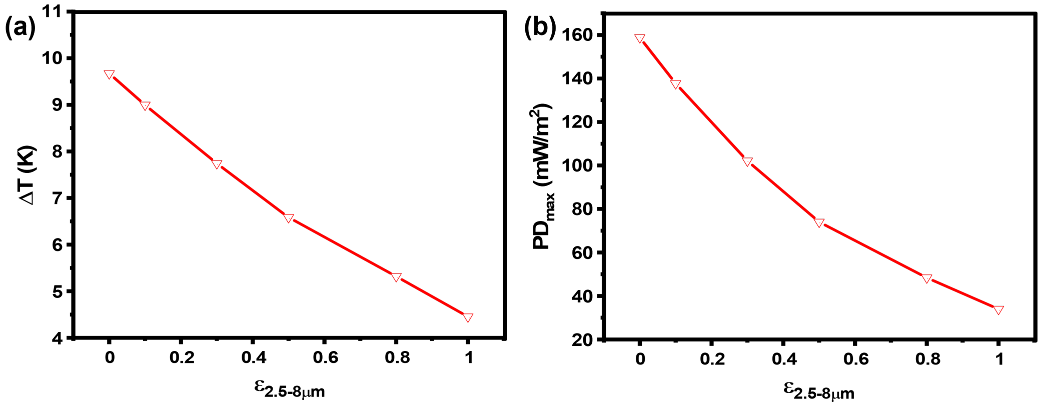

FIGURE 6.8: Performance of RC-TEG obtained in COMSOL simulation as a function of atmosphere emissivity (a) Temperature difference (ΔT) and (b) Power density (PD_{max}). Other simulation parameters were fixed at W_{Cooler} = 80 mm, W_{TE} = 5 mm, H_{TE} = 10 mm, and Pitch = 40 mm.

We also investigate the impact from the band between 2.5 to 8 μm while keeping the $\varepsilon_{8-13\mu m}$ to be 1 and $\varepsilon_{0.3-2.5\mu m}$ to be 0 as shown in Figure 6.8. In this chapter, we assume the temperature of our radiative cooler is always lower than that of the atmosphere. If the RC emissivity in the 2.5-8 μm band is larger than 0, the atmosphere will always radiate energy to the RC (as there is no atmospheric window within this band for the energy to be radiated to the space). This will increase the temperature of the RC and decrease the temperature difference (shown in Figure 6.8a) as well as the power performance of the RC-TEG (shown in Figure 6.8b).

6.5 RC-TEG performance with different TE parameters

The geometrical parameters of the RC-TEG also play a vital role in the power performance. Here we will mainly focus on the impact of the TEG pitch and the width of the radiative cooler W_{Cooler} while keeping the leg width W_{TE} constant.

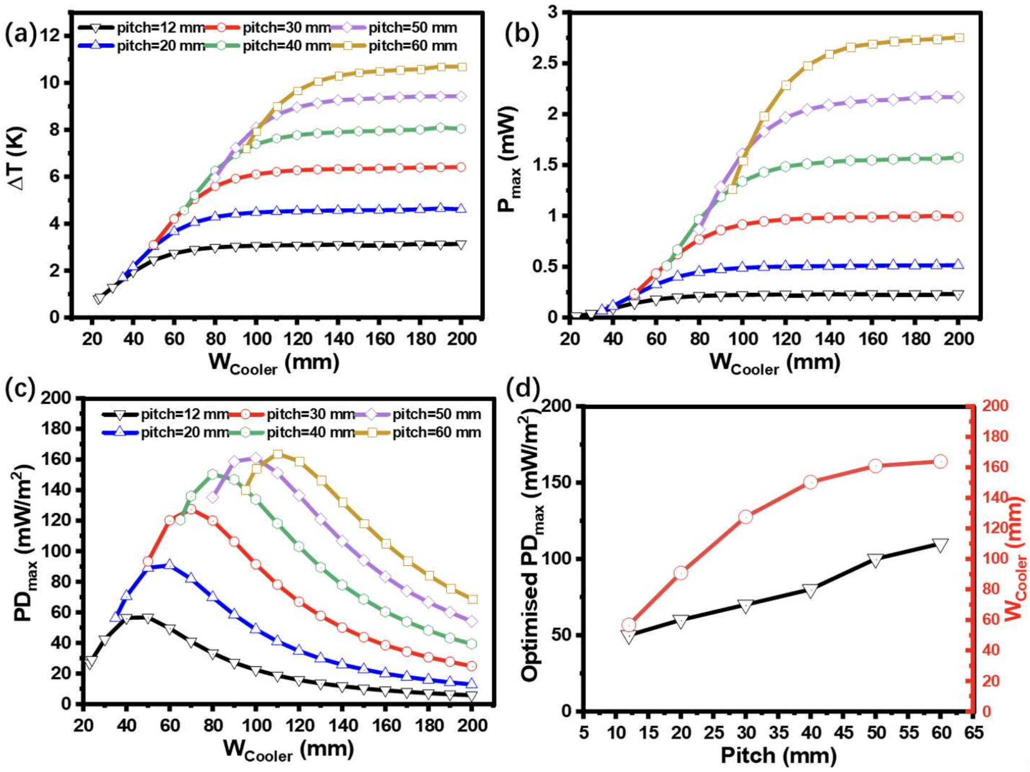

FIGURE 6.9: (a) Temperature difference (ΔT), (b) Power (P_{max}), (c) Power density (PD_{max}) obtained from COMSOL simulation as a function of pitch and W_{Cooler}. (d) optimized power density of W_{Cooler} on different pitches. Other simulation parameters were fixed at W_{TE} = 5 mm and H_{TE} = 10 mm.

Figure 6.9 depicts the effect on RC-TEG performance when both W_{Cooler} and pitch are varied. It is worth mentioning that the starting point of W_{Cooler} is limited by the pitch size and is, therefore, different in each case. It can be observed in Figure 6.9a that ΔT firstly increases with increasing W_{Cooler}. This is reasonable as larger radiative coolers can generate more cooling power, leading to a colder top surface.

However, such an increase quickly saturates at a larger W_{Cooler} if the TEG pitch remains unchanged, as the cooling on top of the TEG area is limited by the heat conduction on the radiative cooler (shown in Figure 6.10). A further increase of the cooling power from the radiative cooler cannot further reduce the cold side temperature.

On the other hand, enlarging the TEG footprint under the radiative cooler by increasing its pitch facilitates thermal conduction on the radiative cooler at the TEG leg areas (shown in Figure 6.11), leading to improved ΔT and TEG output power, as shown in

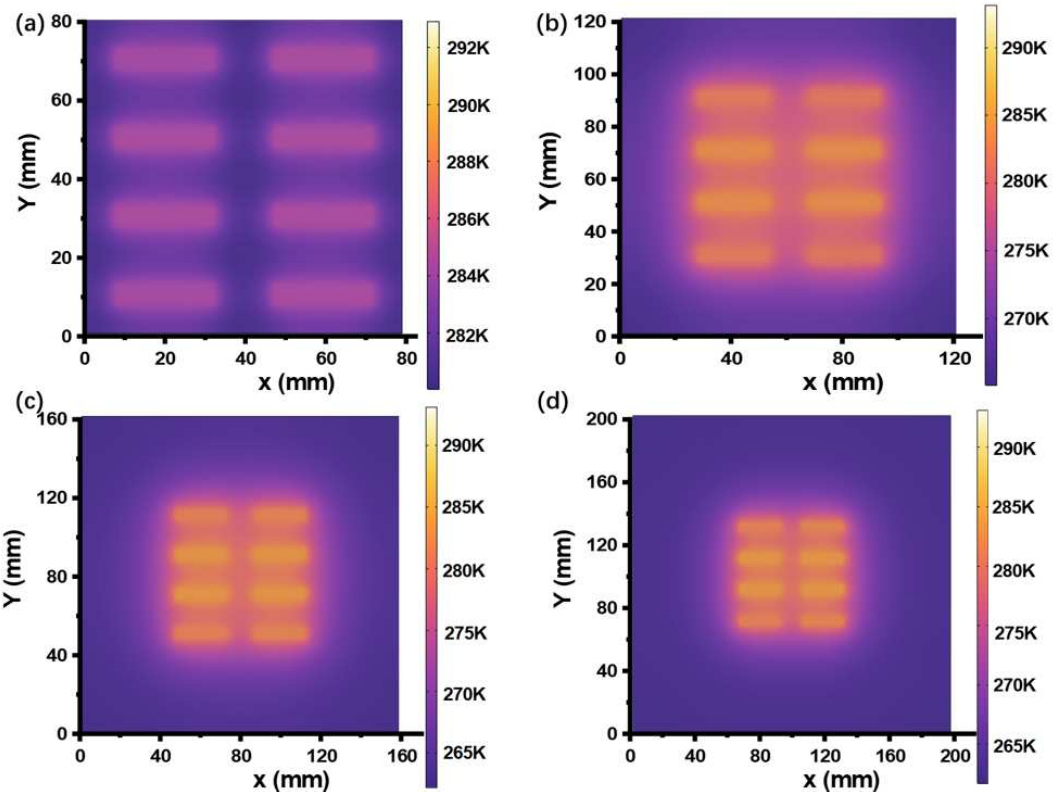

FIGURE 6.10: Temperature mapping for the case of (a) W_{Cooler}=80 mm, (b) W_{Cooler}=120 mm, (c) W_{Cooler}=160 mm, (d) W_{Cooler}=200 mm. $\varepsilon_{0.3-2.5\mu m}$ and $\varepsilon_{8-13\mu m}$ are fixed at 0 and 0.95, respectively. $Conv_T$ and $Conv_B$ is fixed at 1 $W/(m^2K)$ and 50 $W/(m^2K)$, respectively. Other simulation parameters were fixed at W_{TE}=5 mm,H_{TE}=10 mm,Pitch=40 mm.

Figure 6.9a and b. It should be noted here that Figure 6.9b only considers the absolute power output, the change of radiative cooler size also affects the power density (PD_{max}) of the device, which is plotted in Figure 6.9c. As PD_{max} is also a function of the device area, it firstly increases with increasing power and subsequently decreases as the power saturates. Therefore, we can identify the optimized PD_{max} and W_{Cooler} for TEG with different pitch sizes, as shown in Figure 6.9d. It can be observed that the optimized PD_{max} and W_{Cooler} will increase with increasing TEG pitch.

We now focus on the scenario where the size of the radiative cooler is fixed and investigate the performance of RC-TEG under different TEG parameters. Figure 6.12 shows the effect on the RC-TEG of changing W_{TE} and H_{TE} while keeping the W_{Cooler} unchanged. It can be observed that increasing W_{TE} could lead to a decrease of ΔT (Figure 6.12a). This is because when the W_{TE} is increasing, the thermal resistance of TEG will decrease, leading to smaller ΔT across the top and bottom sides. On the other hand, increasing H_{TE} increases the thermal resistance, resulting in larger ΔT. Figure 6.12b shows the results of PD_{max} as a function of W_{TE} and H_{TE}. It can be seen that when the H_{TE} is relatively small ($\leq$15 mm), the PD_{max} decreases as the W_{TE} increases. This is in line with the reduction of ΔT. Whereas at more significant H_{TE} conditions, a

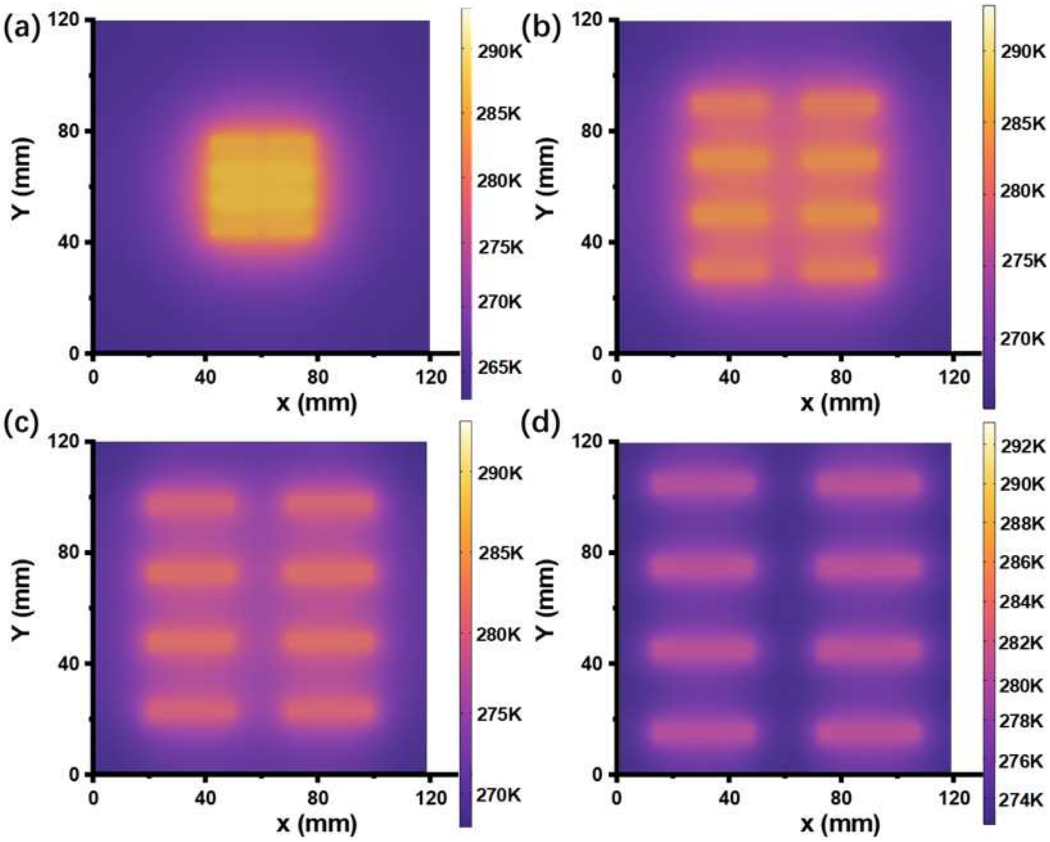

FIGURE 6.11: Temperature mapping for the case of (a) Pitch=20 mm, (b) Pitch=40 mm, (c) Pitch=50 mm, (d) Pitch=60 mm. $\varepsilon_{0.3-2.5\mu m}$ and $\varepsilon_{8-13\mu m}$ are fixed at 0 and 0.95, respectively. $Conv_T$ and $Conv_B$ is fixed at 1 $W/(m^2K)$ and 50 $W/(m^2K)$, respectively. Other simulation parameters were fixed at W_{TE}=5mm,H_{TE}=10mm,W_{Cooler}=120 mm.

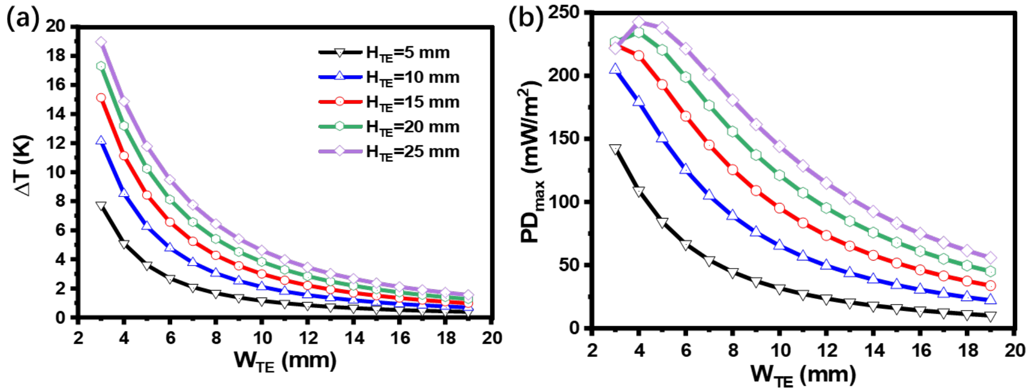

FIGURE 6.12: (a) Temperature difference (ΔT), (b) PD_{max} obtained from COMSOL simulation as a function of H_{TE} and W_{TE}. Other simulation parameters were fixed at W_{Cooler} = 120 mm and Pitch = 40 mm.

slight increase of PD_{max} can be noticed before it falls again with increasing W_{TE}. It is because the negative impact from considerable electrical resistance outweighs the gain from larger ΔT at small W_{TE} and large H_{TE}. An optimized set of TEG parameters can therefore be identified to reach the highest PD_{max}.

6.6 RC-TEG performance under real-time data

One of the key advantages of RC-TEG is its capability to provide a continuous power supply. However, the variation of environmental conditions at different times of day, days of the year, and geographical locations will all affect the power generation of an RC-TEG. Therefore, evaluating the power performance under real-time environmental data is essential.

In this section, we selected London and Singapore as two locations and investigated the full-day RC-TEG performance in summer (July 2021) and winter (January 2021) using real-time data, obtained from Prediction Of Worldwide Energy Resources. It is worth mentioning that all chosen days had similar weather (sunny) to minimise the influence of different atmospheric parameters on the simulation.

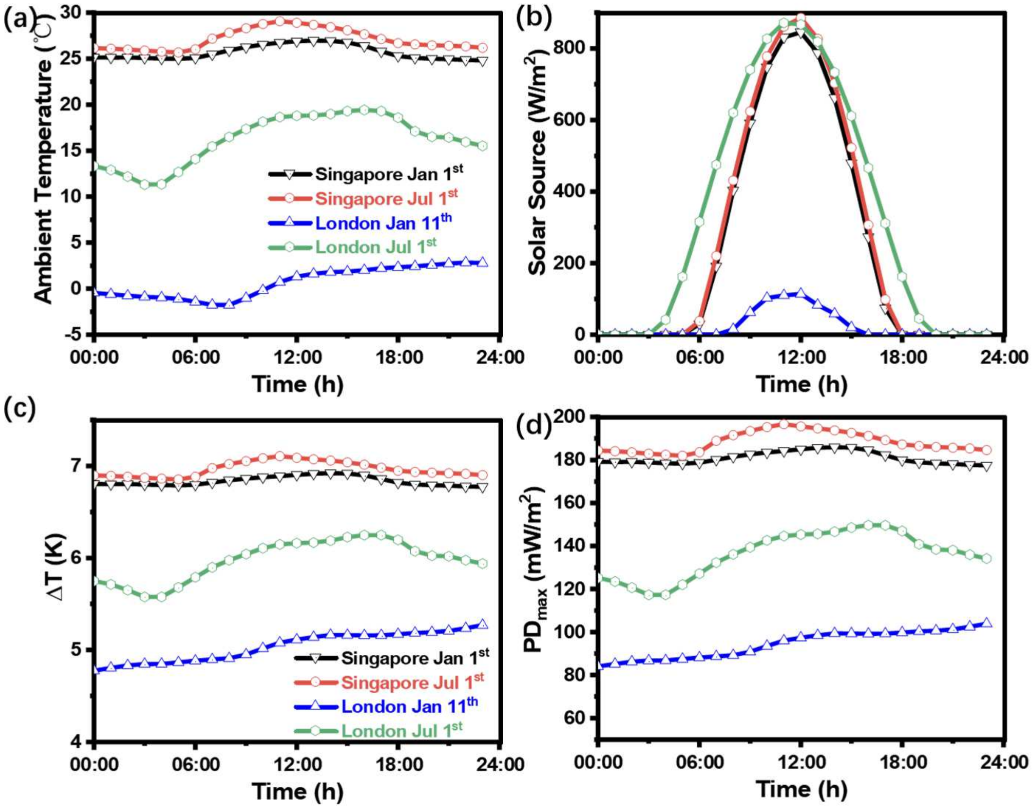

FIGURE 6.13: (a) Temperature difference (ΔT), (b) PD_{max} obtained from COMSOL simulation as a function of H_{TE} and W_{TE}. Other simulation parameters were fixed at W_{Cooler} = 120 mm and Pitch = 40 mm. Data obtained from Prediction Of Worldwide Energy Resources (POWER NASA).

Figure 6.13a shows the real-time temperature on the two days in London and Singapore, where significant differences between different days and locations can be observed. As a place near the equator, the temperatures of those two days in Singapore were similar at over 25°C. On the other hand, temperatures in London were much lower and featured more considerable differences between summer and winter. Similarly, the solar irradiance in Singapore was also very close in those two days. However, they were quite different in the UK, both in the maximum irradiation power and duration.

Figure 6.13c presents the temperature difference ΔT across our RC-TEG under those real-time environmental conditions. A continuous positive ΔT can be achieved in all four conditions, indicating that the radiative cooler can provide unintermittent cooling power to the device throughout the day. The amplitude of the ΔT is strongly related to the real-time temperature as higher ambient temperature could increase the hot (bottom) side temperature of RC-TEG. The power performance of the RC-TEG under these conditions is shown in Figure 6.13d. The device can produce a continuous power supply in all four scenarios. Both days in Singapore feature an average power of over 180 mW/m^2. The summer day in London also produces an average power of ca. 130 mW/m^2. Even on a cold winter day, an average power of over 90 mW/m^2 can be achieved, sufficient enough to power a wide range of IoT and sensory devices [105].

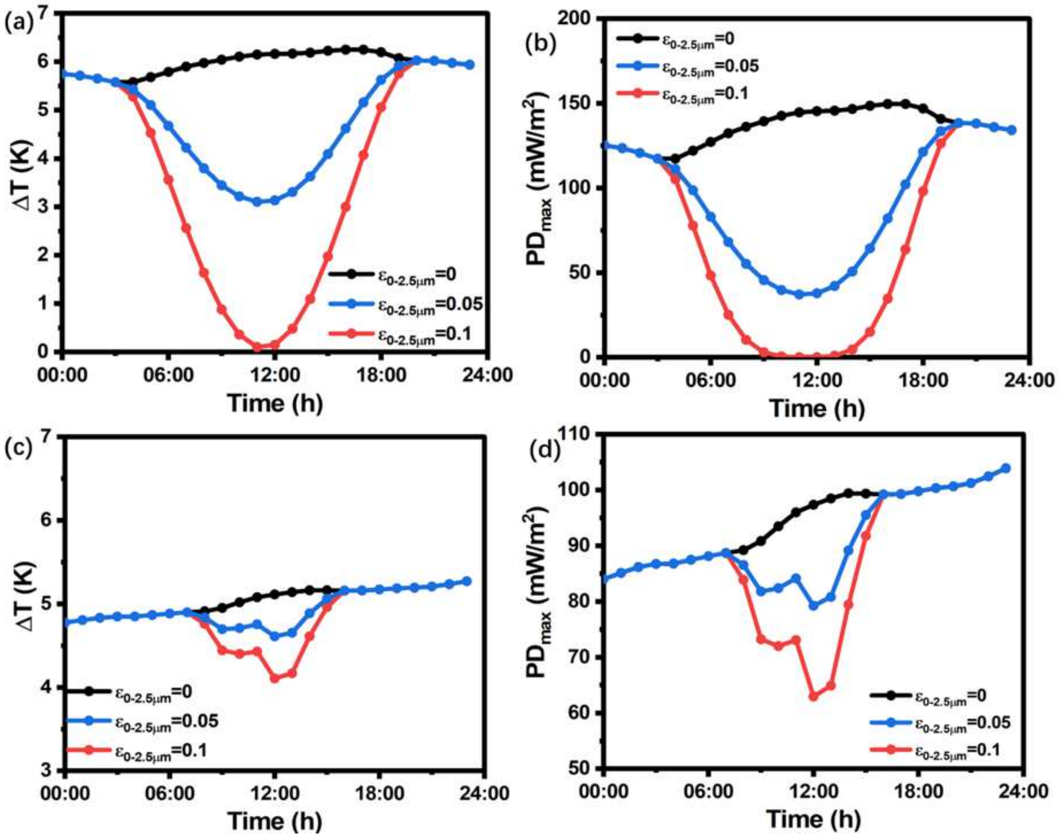

FIGURE 6.14: (a) Temperature difference (ΔT), (b) power density (PD_{max}) obtained from real-time data simulation of RC-TE device on July 1st, 2021, London. (c) Temperature difference (ΔT), (d) power density (PD_{max}) obtained from real-time data simulation of RC-TE device on January 11th, 2021, in London. $\varepsilon_{8-13\mu m}$ is fixed at 0.95. $Conv_T$ and $Conv_B$ is fixed at 1 $W/(m^2K)$ and 50 $W/(m^2K)$, respectively. W_{Cooler}=80 mm, W_{TE}=5mm.

Based on the two sets of data in Figure 6.13, the RC-TE device is simulated for the whole day while varying the $\varepsilon_{0.3-2.5\mu m}$ from 0 to 0.1 on UK data, the results are shown in Figure 6.14.

Figure 6.14a and b is the result of a simulation of July 1st, 2021, UK. The black line in Figure 6.14a is the energy produced by radiative cooling without any solar absorption. Although the output power density fluctuates somewhat with ambient temperature, the overall variation is slight, roughly 150 mW/m^2. Since the solar radiation energy is intense on that day and the daytime hours are 16 hours, eight hours longer than the night. if $\varepsilon_{0.3-2.5\mu m}$ reaches 0.1, the absorbed solar radiation will offset the cooling power at midday.

On the other hand, things were different on January 11th, 2021, UK. Figure 6.14c and d shows a simulation of the data for January 11th, 2021, UK. It can be observed that not only the daytime hours are shorter than on July 1st, but also the reduction in solar energy during the daytime from $\varepsilon_{0.3-2.5\mu m}$ has a smaller impact on the radiative cooling power performance compared to Figure 6.14ab.

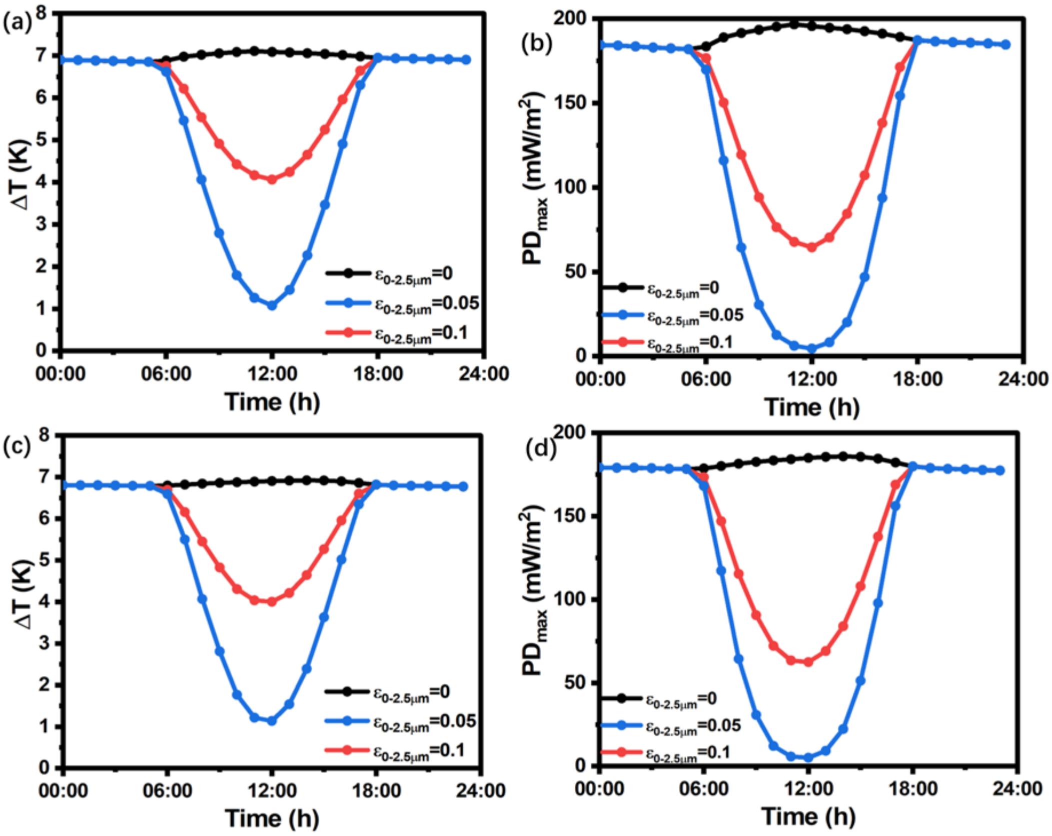

FIGURE 6.15: (a) Temperature difference (ΔT), (b) power density (PD_{max}) obtained from real-time data simulation of RC-TE device on July 1st, 2021, Singapore. (c) Temperature difference (ΔT), (d) power density (PD_{max}) obtained from real-time data simulation of RC-TE device on January 1st, 2021, Singapore. $\varepsilon_{8-13\mu m}$ is fixed at 0.95. $Conv_T$ and $Conv_B$ is fixed at 1 $W/(m^2K)$ and 50 $W/(m^2K)$, respectively. W_{Cooler}=80 mm, W_{TE}=5mm.

In addition, the results were simulated for the whole day while varying the $\varepsilon_{0.3-2.5\mu m}$ from 0 to 0.1 on Singapore data based on the two sets of data in Figure 6.13 are shown in Figure 6.15. Figure 6.15 is the simulation results of real-time data in Singapore. As shown in Figure 6.15a and c, the temperature difference between winter and summer is very close. This result is due to the location of Singapore near the equator, which is hot even in the winter. And from Figure 6.15b and d, when $\varepsilon_{0.3-2.5\mu m}$=0.1, the power density reaches 0 at noon.

6.7 Conclusion

This chapter provides a systematic analysis of TEGs driven by radiation cooling. The impacts from the environmental conditions, radiative cooler properties, as well as the TEG parameters were investigated to provide a complete picture of the performance dependence for RC-TEG devices. It was revealed that a thermally insulating top surface with low convection is crucial for RC-TEG to maintain a decent temperature difference for power generation. The top surface convection should be as insulating as possible, while the bottom surface needs to be a strong heat sink to maximize the power of the RC-TEG. If natural convection is used on the lower surface, it will reduce the power output by about 25%. The atmosphere emissivity, related to the concentration of water vapour and other gases in the air, can also significantly affect the power output. From the perspective of the radiative cooler, whilst a high emissivity within the atmospheric window should be targeted for better power performance, the emissivity within the solar spectrum should be minimised to avoid heat absorption if continuous power generation is required. This can be achieved by a carefully designed multi-layer structure. In addition, we have also revealed that the TEG parameters, including the area ratio between cooler and TEG, and the width and height of the TE legs, should be optimised for improved RC-TEG performance. In addition, the capability of RC-TEG to provide continuous power supply is tested using real-time environmental data from both Singapore and London on two different days of the year, demonstrating continuous power supply in all four scenarios. The RC-TEG can generate over 150 mW/m^2 continuously, providing a long-term power source for some low-power devices such as remote sensors, wearable electronics, and small IoT devices for extended periods.

The RC-TEG model in this chapter is built on COMSOL simulations and does not utilize machine learning methods. The analysis in this chapter demonstrates that the cooling capacity of a radiative cooling device depends exclusively on its parameters and the surrounding environmental conditions, independent of the thermoelectric generator. As a result, radiative cooling can be straightforwardly treated as a heat flux input parameter in the modelling process. This insight simplifies the artificial neural network (ANN) model for the Radiative Cooling Thermoelectric Generator (RC-TEG), allowing it to be approached as a standard TEG ANN model. The methodology for establishing the standard TEG model is identical to that described in Chapter 4. More research will be done on ANN modelling of RC-TEG in future studies.

Chapter 7

Photovoltaic coupled TEG modelling and optimization

The previous chapters have covered the modelling of a thermoelectric generator using an artificial neural network and the system analysis of combining a thermoelectric generator with radiative cooling. This chapter introduces an ANN-based model designed to predict the performance of hybrid PV-TEG systems. Utilizing a cyclic approach, the 3D ANN model incorporates various factors, including PV coating, morphology, TEG geometry, temperature-dependent material properties, and environmental conditions like solar irradiance and convection. The hybrid model allows independent use of PV and TEG components, enhancing its adaptability and generalizability. The chapter further demonstrates how the model can be adapted for a wide range of parameters, showcasing its flexibility and applicability in various scenarios. It also delves into real-time data simulation, illustrating the model's capability to handle dynamic inputs and simulate performance under real-world conditions. This aspect highlights the practical utility of the model in predicting the behaviour of PV-TEG in actual operational environments, making it a valuable tool for researchers and engineers working in the field of renewable energy technologies.

This chapter has been submitted to the journal as Yuxiao Zhu, Daniel W. Newbrook, Peng Dai, Jian Liu, Jichao Li, Chunming Wang, Harold Chong, C.H. Kees de Groot, Ruomeng Huang, Artificial neural network enabled photovoltaic-thermoelectric generator modelling and analysis. The preprint version doi: `10.2139/ssrn.4834580`. As the first author, my contributions include building the PV and TEG COMSOL model, generating the PV and TEG dataset, building the PV and TEG ANN model, performing the parameter sweep for ANN/COMSOL and writing the paper. Daniel provided the thermoelectric material parameters. Peng, Jian, Jichao, Chunming, Harold and Kees reviewed the paper, and Ruomeng reviewed the paper and supervised the project.

7.1 Overview of the hybrid PV-TEG system

Figure 7.1 shows the schematic of the PV-TEG model built in this chapter. The PV cell (pink) is located at the top of the TEG cell which consists of a pair of n-type and p-type thermoelectric legs connected thermally in parallel and electrically in series. A fin-structured heat sink is implemented at the bottom of the TEG cell for heat dissipation. The ceramic and heat sink are AlN in the research. The thermoelectric materials used in this work are $Bi_2Te_{2.7}Se_{0.3}$ for the n-type leg and $Bi_{0.5}Sb_{1.5}Te_3$ for the p-type leg. The detailed thermoelectric properties, such as the Seebeck coefficient, electrical and thermal conductivities, and ZT values of both materials, are adopted from past studies [45] [164] and presented in Figure 6.1b-e. The hybrid PV-TEG system consists of two standalone 3D PV and TEG models, which were constructed first using COMSOL Multiphysics® software for dataset generation and later replaced by ANNs. Both models can work independently to model PV and TEG performance. They can also be connected to model the complex PV-TEG system as shown in Figure 7.2. When solar irradiation arrives at the top surface of the model, the power (P_{solar}) will be converted directly into electricity through the PV cell (P_{PV}). The remaining power will be transformed into heat (P_{rad}) or not absorbed ($P_{non-rad}$), as illustrated in Eqs. 7.1 [124].

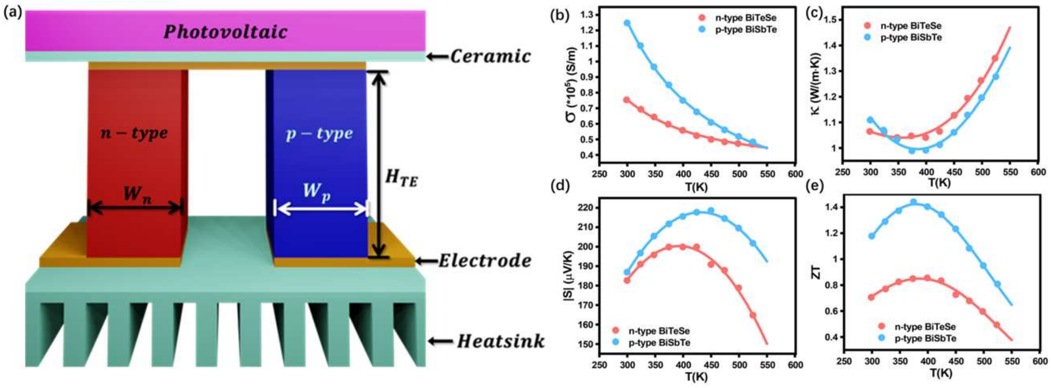

FIGURE 7.1: (a) Schematic of the PV-TEG model (b) Electrical conductivity (σ), (c) thermal conductivity (k), (d) Seebeck coefficient (S), and (e) figure of merit (ZT) of the n-type and p-type semiconductors used for the thermoelectric generator.

$$P_{solar} = P_{PV} + P_{rad} + P_{non-rad} \tag{7.1}$$

Here, $P_{non-rad}$ is intrinsically linked to the material and can be perceived as a fixed fraction of P_{solar}. In this chapter, $P_{non-rad}$ is fixed as 16% of P_{solar} unless otherwise specified [170]. This is the portion of energy in the PV that cannot be converted to heat, including energy that is reflected. Consequently, P_{rad} can be calculated by P_{solar} and P_{PV} and represents the energy to be harvested by the TEG cell in the hybrid system. It should be noted that the actual values of all these powers are temperature-dependent [171]. For a given solar irradiance, a feedback loop needs to be established in the hybrid system to update the temperature of the PV and TEG cells as well as the values of P_{PV}, P_{rad} and $P_{non-rad}$ until an equilibrium is reached in the system. This chapter achieves such a feedback loop by employing a cyclic approach to model the PV-TEG system. Within this framework, a PV model based on a PV cell was developed to calculate the output (P_{PV}) based on the PV temperature (T_{PV}) alongside other influential parameters. Simultaneously, a TEG model, based on a TEG cell, was developed to determine its output (P_{TEG}) as well as the temperature of the PV cell (T_{PV}).

The T_{PV} is assumed to be the same across the PV cell as the temperature difference between the upper and lower surfaces of the PV is very small. As illustrated in Figure 7.2, the initial PV temperature (T_{PV}) aligns with the ambient temperature (T_{amb}). Based on the other operational and geometric parameters (details in the section below), P_{PV} can be calculated. Then, the heat flux Pin into the TEG model is deduced from P_{solar} and P_{PV}. Integrating TEG's operating conditions and geometric parameters, both P_{TEG} and T_{PV} (TEG) are ascertained through the TEG model, and the new T_{PV} will feed back to the PV model to update P_{PV} and P_{rad}, and subsequently update again T_{PV} in the TEG model. This cyclic process will stop when the difference between the previous T_{PV} and the updated T_{PV} falls below a predetermined threshold (ε), which is fixed as 0.01 K in this work. At this time, it is inferred that the PV-TEG system has reached equilibrium, and the results of P_{PV}, P_{TEG}, and T_{PV} will be recorded.

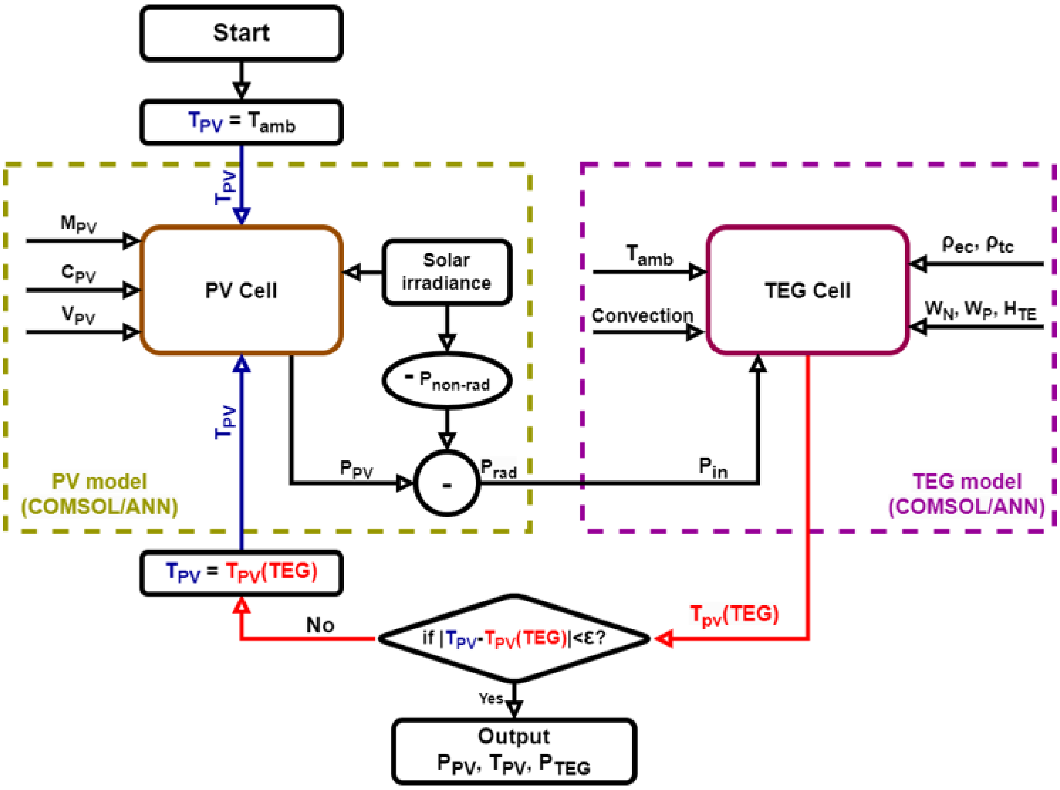

FIGURE 7.2: Flow chart of cyclic PV-TEG model.

7.2 Details of the PV model

The PV cell in the model is made of a 200 µm thick crystalline silicon (c-Si) [172] with the option to include an anti-reflection coating layer which consists of a 65 nm SiN_x film stacking on a 20 nm SiO_2 layer [173][174]. In addition, four different PV morphologies (Planar, Upright pyramids, V grooves, and Spherical caps) were also available in the model. The analytic doping for the PV cell was set to p-type, with an acceptor concentration of 10^{16} $(1/cm^3)$. The donor concentration at the top surface of the PV cell is 10^{19} $(1/cm^3)$. The junction depth is set to be 0.25 µm, and trap-assisted recombination is adopted in the model. The PV cell is connected to a top metal that serves as inlet voltage (V), and the bottom metal serves as ground (0V). Both metals are assumed to be ideal in the model. The performance of the PV cell depends strongly on the specific spectrum of solar irradiance. The spectrum of different solar irradiance in this work was assumed to be proportional to the AM1.5 spectrum. The generation rates of these different PV structures are obtained from the PV lighthouse [175] and shown in Fig. S1. These obtained generation rates were subsequently imported into the PV model to simulate the power outputs of the PV cells. All the input parameters for the PV model are tabulated in Table 7.1.

TABLE 7.1: Ranges and resolutions of parameters used in the PV model.

PV input parameters		Range	Resolution
Geometrical parameters	PV Coating (C_{PV})	[Coating, No Coating]	
	PV Morphology (M_{PV})	[Planar, Upright pyramids, V grooves, Spherical caps]	
Operating conditions	PV Voltage (V)	0-0.65 V	0.01 V
	Solar irradiance (P_{solar})	0-1000 W/m^2	1 W/m^2
	PV Temperature (T_{PV})	263-363 K	0.1 K

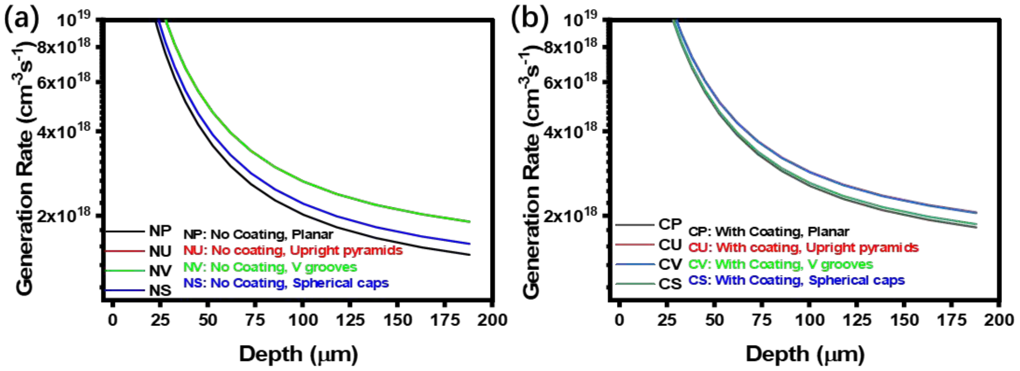

FIGURE 7.3: The Generation rate of (a) no coating and (b) with coating PV structures.

The configuration of the neural network for the PV model is shown in Figure 7.4. The PV-ANN is structured with an input layer of five parameters, leading to a series of 5 hidden layers, each containing 400 neurons. The model ultimately converges to a singular output node of the PV output power (P_{PV}). 3D simulations from COMSOL Multiphysics are used to generate the dataset for neural network training using Semiconductor Module, Electric Current Module and Electrical Circuit Module. The dataset contains 10,000 instances. The input parameters were randomly generated based on their ranges and resolutions in Table 7.1. The 10.000 sets of parameters were then simulated in COMSOL to obtain the P_{PV}, which serves as the output of the dataset. For training purposes, the PV-ANN dataset was grouped into training (8,000 instances), validation (1,000 cases), and testing (1,000 instances) subsets. The specific dataset can be found in the Appendix link. The mean square error (MSE) serves as the designated loss function. Detailed specifications of other ANN-related hyperparameters can be found in the Supplementary Information. The training subset optimized the network by iteratively updating its neuron weights and biases via backpropagation. Concurrently, the validation subset data served the purpose of monitoring overfitting in the training process. Once training was complete, the test data subset, previously unseen by the network, was introduced to assess the network's predictive accuracy.

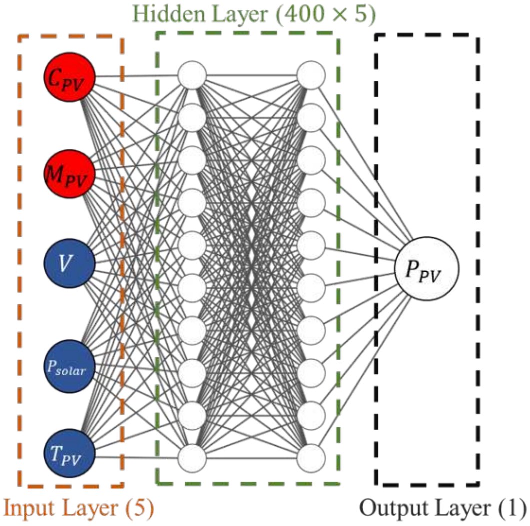

FIGURE 7.4: Architecture of the forward modelling neural network for predicting power performance of the PV model.

Then, the PV model is validated by nominal operating cell temperature (NOCT). The condition includes the model being in the open space with an ambient temperature of 293.15 K, environmental wind speed of 1 m/s and solar irradiance of 800 W/m^2. The nominal operating cell temperature for most of the commercially available polycrystalline silicon photovoltaic models is 45 ± 2°C according to manufacturers' data [176]. In our model, under the same conditions, T_{PV} = 320K (46.85°C), within the NOCT range.

In the experiments of Zhou et al., a PV temperature of 325.23 K was obtained at the ambient temperature of 25 °C, environmental wind speed of 1 m/s, and solar irradiance of 1000 W/m^2 [177]. The PV temperature obtained in our model under the same conditions is 325.56 K, close to Zhou's results.

For a standalone PV model, Eqs. 7.2 can be established to calculate the temperature of the PV when the PV is operating independently:

$$A_{PV}(P_{solar-P_{non-rad}-P_{PV}}) = A_h h(T_{PV} - T_{amb}) \tag{7.2}$$

Where A_{PV} is the PV surface area, A_h is the area with the convection coefficient. In the standalone PV model, $A_h = 2A_{PV}$. A comprehensive flowchart detailing the mechanics of the standalone PV model can be found in Figure 7.5. Figure 7.6 illustrates the power performance of the PV in the time domain. The $P_{non-rad}$ in Figure 7.6 is set to be 0. Figure 7.6a shows the trend of P_{PV} and convection heat flux with time. As observed, P_{PV} experiences a gradual decline over time. This decrease can be attributed to the PV's increased heat absorption, leading to a rise in temperature and a corresponding drop in efficiency. Correspondingly, as the gap between the PV temperature and ambient temperature widens, the convection heat flux increases. Upon reaching the 150-second mark, the system begins to approach equilibrium, with P_{All} stabilizing at 1000 W/m^2, matching the power of the input heat flux. Figure 7.6b illustrates the PV power and temperature independently, further confirming that the observed reduction in PV power is directly due to the increased PV temperature. The equilibrium results in the transient simulation were compared with those from our approach mentioned above in Figure 7.6b (triangles) and demonstrate a perfect match. This confirms the fidelity of our PV model.

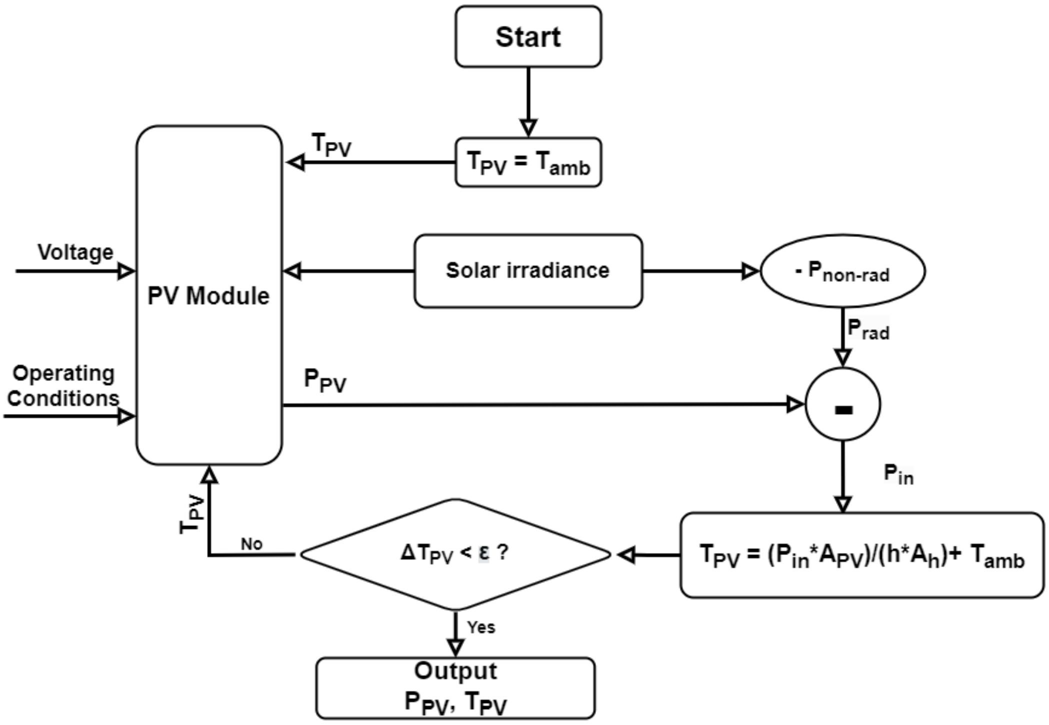

FIGURE 7.5: Flow chart of standalone PV ANN model.

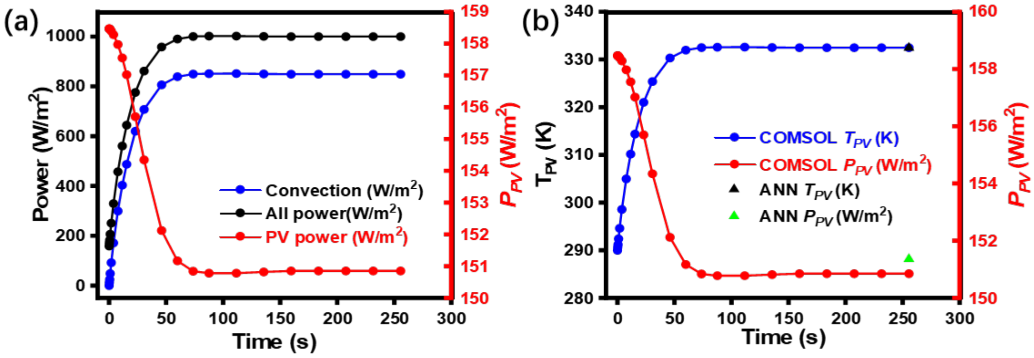

FIGURE 7.6: Time-dependent PV-TEG model analysis. (a) P_{PV}, convection heat flux and total power, (b) P_{PV} and T_{PV} time sweep in COMSOL model.

7.3 Details of the TEG model

The TEG cell has a c-Si layer on the top and a ceramic aluminium nitride layer. The temperature of the c-Si layer is assumed to be the PV temperature. Copper electrode under ceramic connecting the n-type $Bi_2Te_{2.7}Se_{0.3}$ [164] and p-type $Bi_{0.5}Sb_{1.5}Te_3$ [45] thermoelectric materials. Electrical contact resistance [178] and thermal contact resistance [64] have also been suggested as factors for TEG and were therefore included in the model by introducing electrical contact resistivity (ρ_{ec}) and thermal contact resistivity (ρ_{tc}) between the four thermoelectric material and the interconnect interfaces. The height of the ceramic and electrode is 0.5mm. The bottom ceramic is also aluminium nitride, with an extended section of fins as the heat sink, where each has a width of 1 mm, a height of 5 mm, and a depth of 10 mm. During the simulation, convective heat flux (h) is applied to the top PV and bottom ceramic surfaces (including the heat sink) while all other surfaces are thermally insulated. The other surfaces have a convection coefficient of 0 $W/(m^2K)$. The TEG model connects to an external load for electrical boundary conditions to form a circuit. The inlet and outlet of the metal substrate serve as a terminal and the ground (0V) for the model.

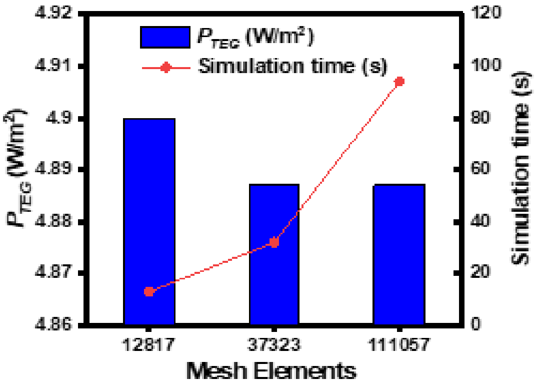

FIGURE 7.7: TEG Power (blue) and time (red) of the COMSOL simulation performed at different mesh elements.

TABLE 7.2: Ranges and resolutions of parameters used in the TEG model.

PV input parameters		Range	Resolution
Geometrical parameters	Width of n-type leg (W_n)	1-9 mm	0.1 mm
	Width of p-type leg (W_p)	1-9 mm	0.1 mm
	Height of the TEG leg (H_{TE})	5-30 mm	1 mm
Operating conditions	Heat flux (P_{in})	0-1000 W/m^2	1 W/m^2
	Convection coefficient (h)	1-25 $W/(m^2K)$	1 $W/(m^2K)$
	Electrical contact resistance (ρ_{ec})	10^{-9}-10^{-7} Ωm^2	10^{-9} Ωm^2
	Thermal contact resistance (ρ_{tc})	$10^{-6} - 10^{-4}$ Km^2/W	10^{-6} Km^2/W
	Ambient temperature (T_{amb})	263-363K	0.1 K

The mesh selection is shown in Figure 7.7. The results showed that the maximum output power obtained from 37323 elements and 111057 elements configurations are almost identical. 37323 mesh elements configuration was therefore employed to simulate all parameter sets for minimizing computational time while maintaining accuracy. The maximum element size is 2mm, and the minimum element size is 1mm. And the maximum element growth rate is 1.45.

Table 7.2 lists the input parameters of the TEG model, which consists of 3 geometric parameters and 5 operating conditions. The geometric parameters include two leg widths (W_n and W_p) and the leg height (H_{TE}). The operating conditions comprise the heat flux injected from the PV cell (P_{in}), surface convection coefficient (h), and ambient temperature (T_{amb}) Electrical contact resistance [178] and thermal contact resistance [64] have also been suggested as crucial factors for TEG and were therefore also included in the model by introducing electrical contact resistivity (ρ_{ec}) and thermal contact resistivity (ρ_{tc}) between the four thermoelectric material and the interconnect interfaces.

Figure 7.8 shows the configuration of our TEG neural network. All 8 input parameters are included in the input layer of the network and connect to hidden layers that consist of 4 layers and 700 neurons in each layer. The outputs of the TEG-ANN are the TEG-generated power (P_{TEG}) and the top surface temperature, which is also the temperature of the PV cell (T_{PV}). 5,000 sets of input parameters were randomly generated based on the resolution range presented in Table 7.2. The dataset can be found in the Appendix link. The power and temperature outputs of these 5,000 parameter sets were simulated in COMSOL to generate a dataset containing 5,000 input-output relations for the ANN training process. During the training process, the TEG dataset was partitioned into three subsets for training (4,000 instances), validation (500 cases), and testing (500 instances). Similar to the PV-ANN training, the loss function was defined as the MSE, which was used to update the weights and bias for the neurons in the backpropagation process to improve prediction accuracy.

Two performance factors, TEG power density (P_{TEG}) and PV temperature (T_{PV}), were extracted from the simulation. The electrical terminal was connected directly to the load resistance for each parameter set and swept from 1/100 to 100 times the internal

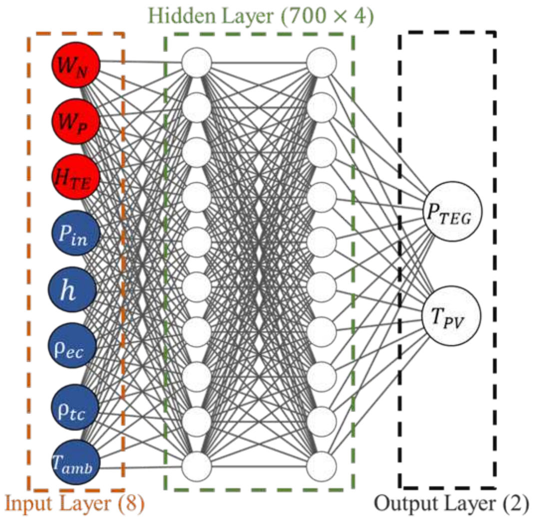

FIGURE 7.8: Architecture of the forward modelling neural network for predicting power performance of the TEG model.

resistance. The maximum output power was then extracted from a parabolic fit of the output power against the current out as shown in Figure 7.9. We determined the load corresponding to the highest output power by fitting a curve to ten data points scanned from the TEG power output. Concurrently, we also fitted the corresponding temperature curve, as illustrated in Figure 7.9b. The load value, calculated from the power output data, was then input into the fitted temperature curve to estimate the temperature at that specific load.

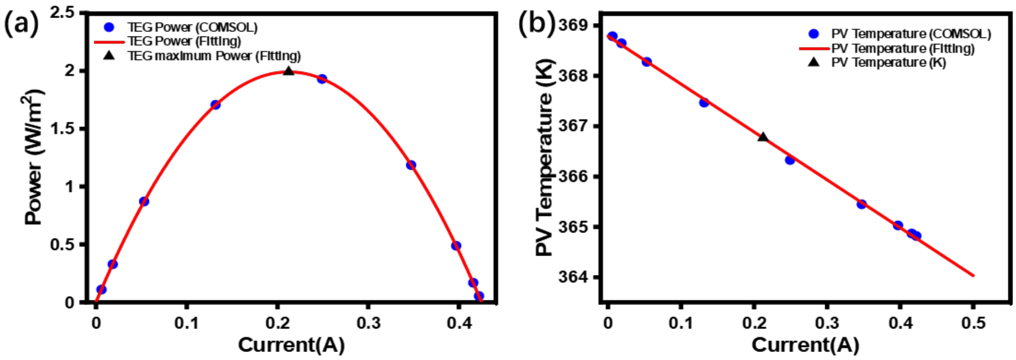

FIGURE 7.9: (a) Power density values and (b) PV temperature from COMSOL simulation (dots) and parabolic fitting (line) of a typical TEG as a function of currents by varying the load resistance.

7.4 PV-TEG ANN model training results

Figure 7.10 shows the test dataset results of PV ANN with fitting curve y=x. The R-square value of 0.9999, being very close to 1, indicates that the ANN model is close to

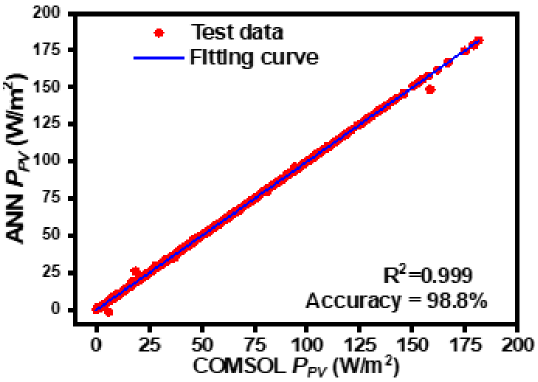

FIGURE 7.10: Scatter plot of the PV ANN predicted PV power density (P_{PV}) and the ground truth (simulated).

the results from COMSOL simulations. We define accuracy as Eqs. 7.3:

$$Accuracy = (1 - \frac{|Prediction - truth|}{truth}) \times 100\% \tag{7.3}$$

Where prediction is the result from ANN, truth is the result from COMSOL. Figure 7.10 shows that the PV ANN model predicts P_{PV} with an accuracy of 98.77%. TEG ANN

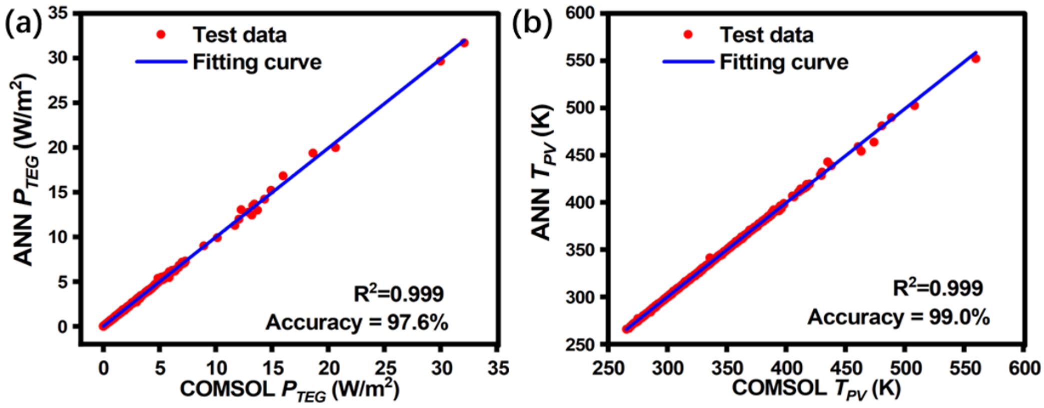

FIGURE 7.11: Scatter plot of the TEG ANN predicted and the ground truth (simulated) (a) TEG power density (P_{TEG}) (b) PV temperature (T_{PV}).

test dataset results are shown in Figure 7.11. The R-squares of two fittings are also very close to 1. From Figure 7.11, the accuracy of P_{TEG} in the TEG ANN model is 97.6%, and the accuracy of predicting T_{PV} is up to 99%. These results demonstrate that ANN is a suitable substitute for the COMSOL model. After training the ANN models for TEG and PV, the PV-TEG model can be built according to the flowchart in Figure 7.2. The specific code for this process can be found in the Appendix.

7.5 PV-TEG model validation

We will now evaluate the performance of the two ANNs in the hybrid PV-TEG model by executing the cyclic approach (approach illustrated in Figure 7.2) to predict the power performance of the hybrid model. Figure 7.12 shows the P_{PV}, P_{TEG} and T_{PV} results in the cyclic ANN model with the final steady-state results of the COMSOL model. Figure 7.12a presents the predicted P_{PV} and P_{TEG} at various stages of the cyclic process while Figure 7.12b plots the associated change of T_{PV}. In the initial stage (cycle 0), the T_{PV} is set to be equal to the ambient temperature, and the power outputs from both PV and TEG models remain 0. As the system begins operating, drastic increases are observed for P_{PV} and P_{TEG} in cycle 1. This is accompanied by the increase in the cell temperature T_{PV}, which subsequently leads to a slight reduction of P_{PV} (cycle 2). After about 3 cycles, the hybrid PV-TEG system reaches an equilibrium state, and all outputs remain stable in the following cycles. The output values from the final 9th cycle are compared with the results from the COMSOL steady-state simulation (triangle marks), showing a perfect match. These results further validate the fidelity of our ANN models and cyclic approach. It is worth noting that, given one PV voltage, despite several cycles required in the approach, the total computational time is only 3 ms, significantly shorter than that required in COMSOL simulation (90 s). From this on, all further analysis in this work will be based on the results from the final equilibrium state. Concerning the PV-TEG model, verifying whether the cyclic state results are consistent with the COMSOL steady state results is necessary. Figure 7.12 shows the P_{PV}, P_{TEG} and T_{PV} results in the cyclic ANN model with the final steady-state results of the COMSOL model.

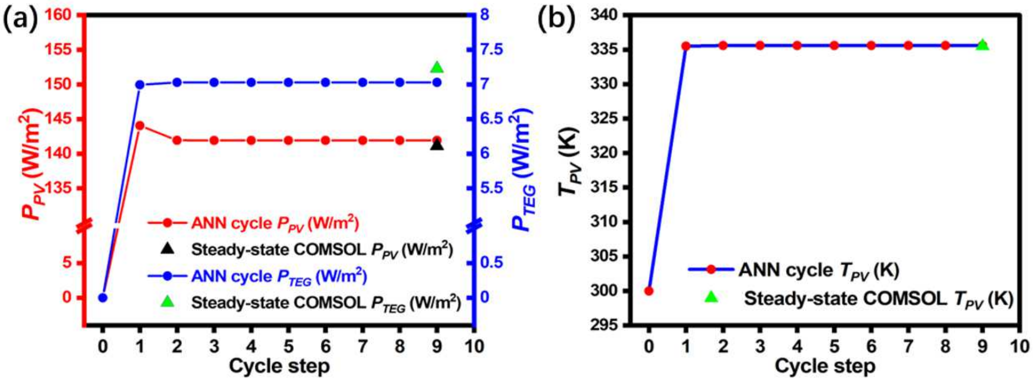

FIGURE 7.12: (a) P_{PV} and P_{TEG} in cycle sweep of ANN model and the corresponding steady-state COMSOL results (b) T_{PV} in cycle sweep of ANN model and the corresponding steady-state COMSOL results. (P_{solar}=1000 W/m^2, h=10 $W/(m^2K)$, W_n=W_p=5 mm, H_{TE}=20 mm, T_{amb}=300K, V_{PV}=0.4 V, $P_{non-rad}$=0 W/m^2).

7.6 Comprehensive PV-TEG system analysis

Having established the accuracy and fidelity of our ANNs and cyclic approach, we now conduct a comprehensive analysis of all parameters and their impact on the performance of the hybrid PV-TEG system.

7.6.1 PV voltage and surface condition

Figure 7.13 illustrates the ANN-predicted performance of the PV-TEG system under varying PV input voltages while keeping other parameters (e.g. geometries, coatings and morphologies) constant. In Figure 7.13a, it is observed that the current density of the PV decreases as the voltage increases. Notably, the rate of decrease becomes significantly pronounced when the voltage exceeds 0.4V. The power output of the PV cell, P_{PV}, which is the product of current and voltage, is shown in Figure 7.13b. Figure 7.13c shows TEG power as a function of the PV voltage. It is observed that P_{TEG} initially decreases but increases with rising PV voltage. This behaviour is predominantly due to the influence of the PV temperature at the upper surface, shown in Figure 7.13d as a function of the PV voltage. This trend is because P_{PV} increases first and decreases with increasing voltage. According to Eqs. 7.1, an increase in P_{PV} leads to a decrease in P_{rad}, and consequently, the heat absorbed by the PV-TEG system decreases, resulting in a lower PV temperature. Subsequently, as P_{PV} decreases, Prad increases, causing the model to absorb more heat, which leads to an increase in the PV temperature. Figure 7.13e illustrates the total output power of the hybrid system P_{All} (comprising P_{PV} and P_{TEG}) in response to increasing voltage levels. Notably, the P_{All} trend follows well with that of P_{PV}. This is not surprising as P_{PV} is still the dominating power contributor in the PV-TEG system. As seen in Figures 7.14b and 7.14c, there is 160 W/m^2 of output power at the peak of the P_{PV}, while the P_{TEG} has an output of 4.2 W/m^2 at this time, accounting for more than 2.5% of the total power.

For comparison, outputs from the COMSOL simulation are also depicted in the blue dots in the figures. The close alignment of the ANN results with those from COMSOL underscores the high accuracy of our ANN model in simulating the performance of PV-TEG systems under varying voltage inputs. It is also worth noting that a voltage sweep for one set of parameters only takes 0.15s using our ANN models, compared with 15 minutes of COMSOL simulation. This lets us quickly identify the maximum power output point (P_{max}) for each parameter set and its associated voltage. From this, all following analyses will sweep the voltage and present the maximum power output point (P_{max}) instead. Even if utilize faster ways of modelling in COMSOL, such as decreasing the mesh size to speed up computation, the time required for creating the ANN training dataset will also be greatly reduced. This will benefit the ANN model as well.

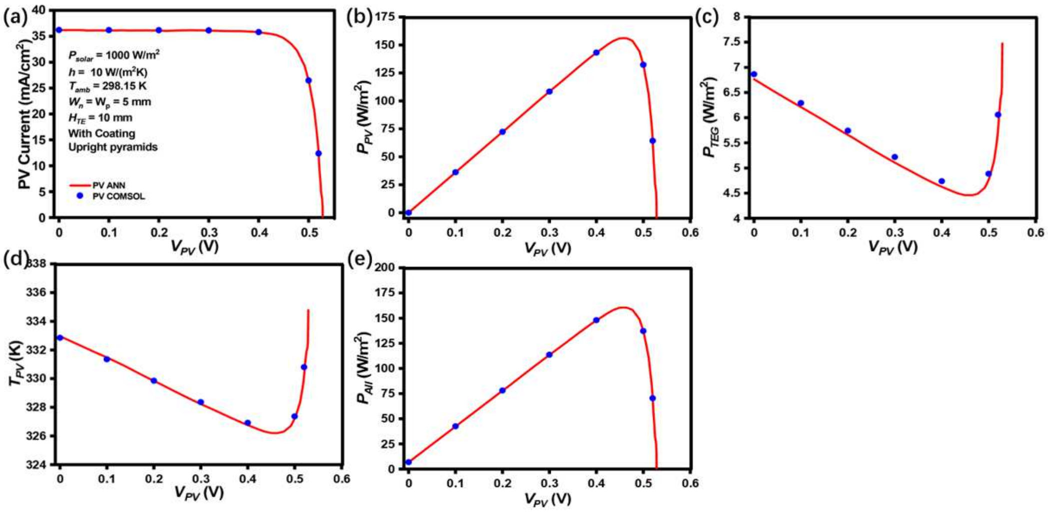

FIGURE 7.13: (a) PV current, (b) PV power density (P_{PV}), (c) TEG power density (P_{TEG}), (d) PV temperature (T_{PV}) and (e) total power density (P_{All}=P_{PV}+P_{TEG}) obtained from ANN (line) and COMSOL (dot) as a function of PV voltage. (P_{solar}=1000W/m^2, h=10$W/(m^2K)$, W_n=W_p=5mm, H_{TE}=10mm, T_{amb}=298.15K).

Figure 7.14 presents the performance of the PV-TEG system under various coatings and morphologies. The combinations of coatings and morphologies are coded in the figure for simplicity in representation. The first letter in each code denotes the presence or absence of coating: 'C' stands for with coating, and 'N' for without coating. The second letter corresponds to the morphology, with 'P', 'S', 'U', and 'V' representing the four different morphologies: Planar, Spherical Caps, Upright Pyramid, and V Grooves, respectively. For clear differentiation, these are depicted in various colours in Figure 7.14.

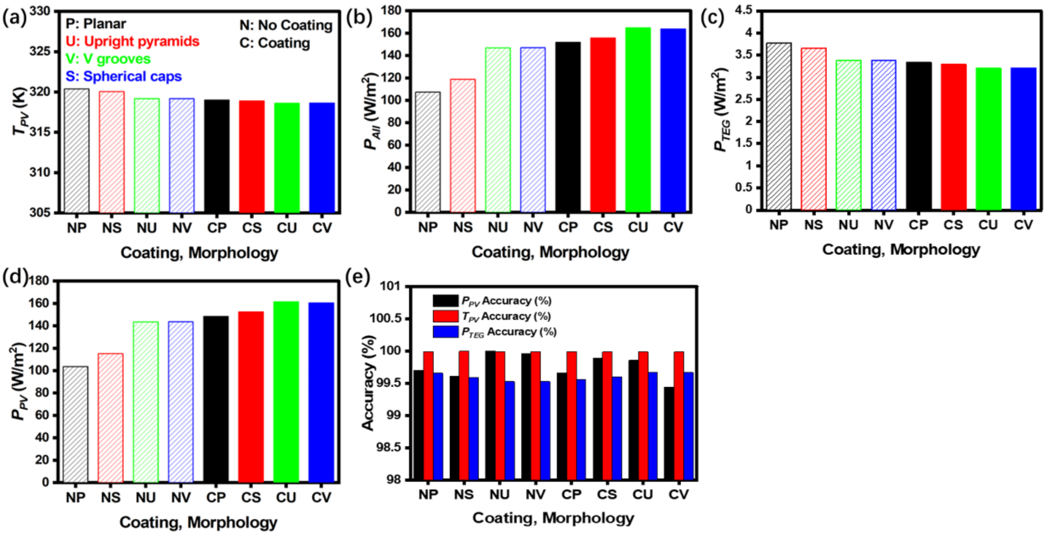

FIGURE 7.14: (a) PV temperature (T_{PV}), (b) Total power density (P_{All}), (c) TEG power density (P_{TEG}), (d) PV power density (P_{PV}) obtained from ANN and (e) Accuracy calculated from COMSOL as a function of coating (C_{PV}) and morphology (M_{PV}).

Figure 7.14a displays the results of T_{PV} under various coatings and morphologies. It is observable from the figure that the temperature is marginally higher in configurations without coating compared to those with coating. This can be explained by the fact that the absorption rate of PV is higher in the presence of coating, generating more P_{PV} and leading to lower T_{PV}. The various morphologies exhibit different temperatures, which can be attributed to their differing absorption rates.

Figure 7.14b shows the distribution of P_{All} in different morphology and coating. The specific analysis is based on Figure 7.14c and d. Figure 7.14c illustrates the distinct behaviour of P_{TEG}. The output of the TEG in this context primarily depends on the upper surface's temperature. Therefore, it follows a similar trend to that observed in Figure 7.14a.

Figure 7.14d depicts the distribution of P_{PV}. The output is significantly higher with coating, leading to increased light absorption into the PV. The different morphologies exhibit varying levels of surface roughness, and the more complex morphologies enable light to undergo multiple reflections within the coating, thereby enhancing the absorption rate. In contrast, with its smoother surface, the planar morphology allows for only a single reflection within the PV, resulting in the lowest absorption rate.

Overall, the accuracy of all output parameters exceeds 98%, as illustrated in Figure 7.14e. This high accuracy indicates that the PV-TEG cyclic ANN model is very well-fitted. Additionally, the models in this study can incorporate various morphologies and coatings into their parameters. This feature introduces diversity and enhances the generalizability of the model.

7.6.2 Environmental condition

Environmental factors like solar irradiance and convection significantly influence the performance of the PV-TEG system. Figure 7.15 demonstrates how the PV-TEG model performs under various scenarios of solar irradiance and convection coefficients. This illustration highlights the system's responsiveness to changes in these critical environmental conditions.

Figure 7.15 shows the performance of P_{PV} with the solar irradiance across all convection conditions. However, this increase tends to slow down at higher solar irradiance levels in conditions of lower convection. The reason for this is that lower convection hinders the transfer of energy to the environment, resulting in a significant increase in PV temperature (as depicted in Figure 7.15b), which in turn reduces the efficiency of the PV cells. This observation underscores the critical role of convection in the operation of PV cells.

Figure 7.15c illustrates the trend of P_{TEG} under varying solar irradiance and convection coefficient conditions. Overall, P_{TEG} increases with solar radiation. However, as

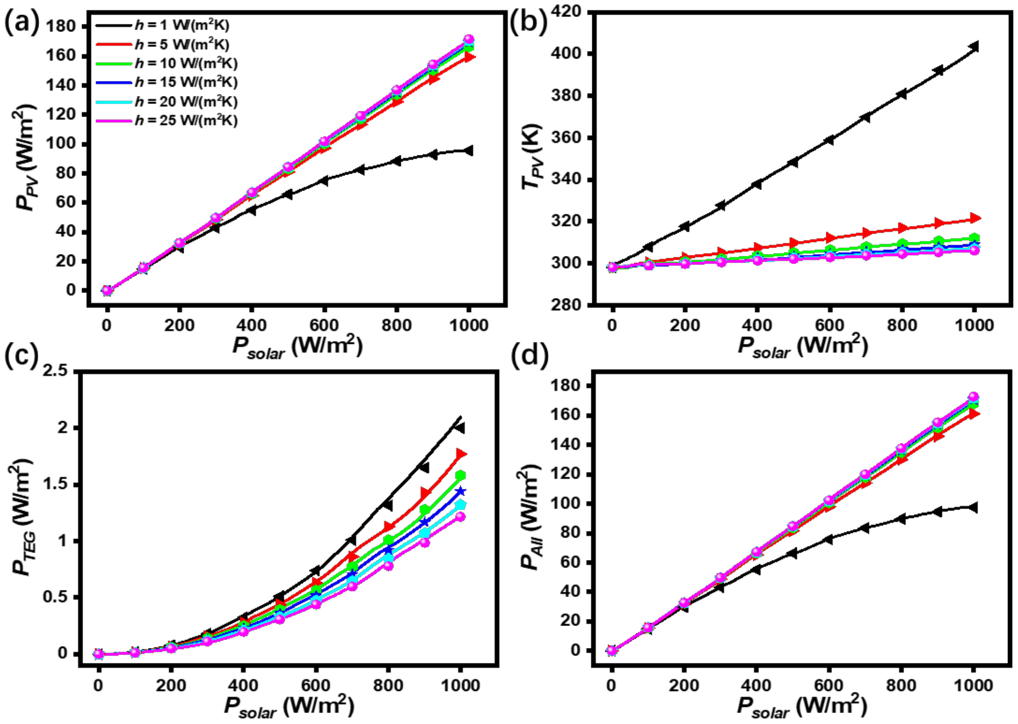

FIGURE 7.15: (a) PV power density (P_{PV}), (b) PV temperature (T_{PV}) (c) TEG power density (P_{TEG}), and (d) total power density (P_{All}) obtained from ANN (line) and COMSOL (dot) as a function of solar irradiance and convection coefficient. Other parameters are fixed with W_n=W_p=5mm, H_{TE}=10mm, and T_{amb}=298.15K.

convection intensifies, P_{TEG} gradually decreases. This trend occurs because higher convection dissipates more energy into the environment, resulting in less energy being available to enter and be converted by the TEG.

Figure 7.15d displays the variation in the total output power (P_{All}) of the PV-TEG system. The overall trend observed in this figure aligns with that seen in Fig. 10a, primarily because the contribution of P_{TEG} to the total output is relatively small. Figure 7.15b, on the other hand, highlights that the rate of increase in PV temperature is significantly steeper when the convection coefficient is minimal.

The line and point further corroborate the accuracy of the ANN model in comparison to the COMSOL simulations fits shown in Figure 7.15. These fit showcase the ANN model's ability to closely replicate results from the more complex COMSOL simulations, highlighting its effectiveness and reliability in modelling the PV-TEG system under diverse environmental conditions.

Figure 7.16 demonstrates the performance of the PV-TEG model for different ambient temperatures (T_{amb}) and convection coefficients. Figure 7.16a shows that the P_{PV} decreases with increasing ambient temperature, which is mainly on account of the increase in T_{PV} with ambient temperature as shown in Figure 7.16b. At the same ambient temperature, the greater the convection, the higher the P_{PV}. This correlation can be

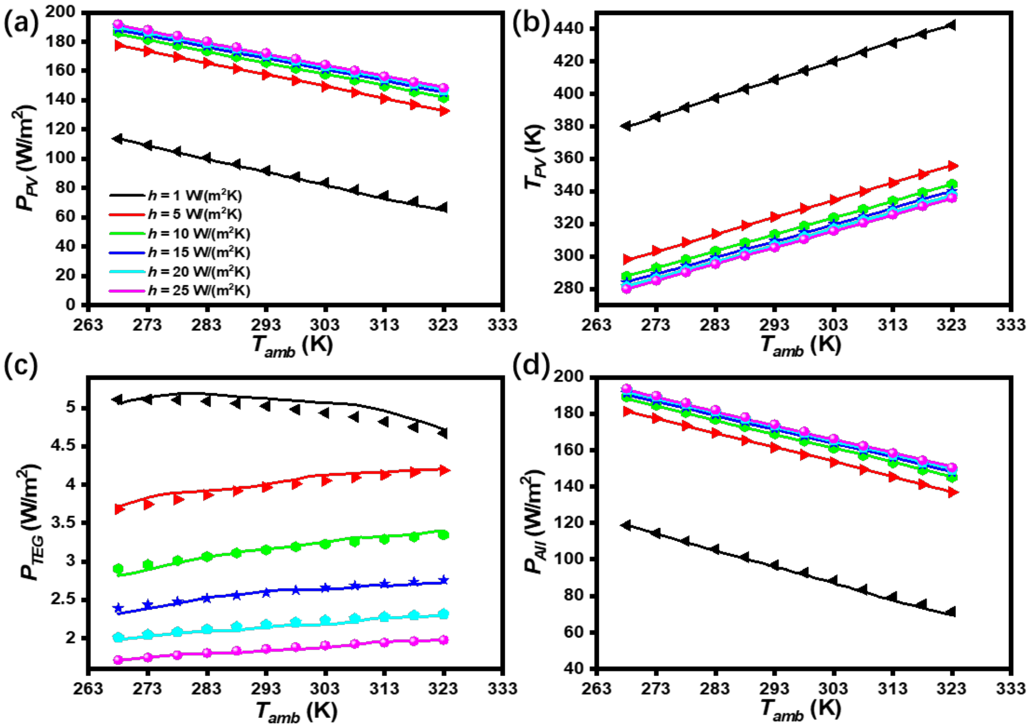

FIGURE 7.16: (a) PV power density (P_{PV}), (b) PV temperature (T_{PV}), (c) TEG power density (P_{TEG}), and (d) total power density (P_{All}) obtained from ANN (line) and COMSOL (dot) as a function of ambient temperature (T_{amb}) and convection coefficient. Other parameters are fixed with W_n=W_p=5mm, H_{TE}=10mm, and P_{solar}=1000W/m^2.

attributed to the reduced T_{PV} observed with increasing convection, as shown in Figure 7.16b.

Figure 7.16c shows that under lower convection conditions (e.g., 1 $W/(m^2K)$), P_{TEG} decreases slightly with an increase in ambient temperature. Conversely, in scenarios with higher convection rates, P_{TEG} exhibits a slight increase with rising ambient temperature. This behaviour can be attributed to the ZT (thermoelectric figure of merit) maxima for the two materials used in this study, which are between 350K and 400K, as illustrated in Figure 7.1. Therefore, the efficiency of the TEG improves when its temperature approaches this optimal range.

As depicted in Figure 7.16b, for convection coefficients ranging from 5 $W/(m^2K)$ to 25 $W/(m^2K)$, an increase in ambient temperature gradually brings the T_{PV} closer to this optimal temperature range. In contrast, at a convection coefficient of 1 $W/(m^2K)$, the temperature tends to move away from the 400K mark. The trend observed in Figure 7.16d aligns with that in Figure 7.16a. This consistency further highlights the impact of ambient temperature and convection conditions on the overall performance of the PV-TEG system, especially in terms of their effect on the efficiency and output of the TEG component

The data presented in Figure 7.15 and Figure 7.16 demonstrate that the model used in this work successfully integrates several crucial environmental parameters. By accounting for factors such as solar irradiance, convection coefficients, and ambient temperature, the model offers a comprehensive and adaptable framework for understanding and predicting the performance of the PV-TEG system in diverse real-world scenarios.

7.6.3 TEG geometry

Figure 7.17 demonstrates the performance of PV-TEG at different TEG leg widths (W_n, W_p) and heights (H_{TE}), setting W_n=W_p. Figure 7.17a clearly shows that P_{PV} experiences a gradual increase as the width of the TEG leg expands. However, this increment rate slows down as the leg width becomes larger. Notably, under comparable leg width conditions, P_{PV} gradually declines with an increase in H_{TE}. This phenomenon can be explained by understanding that a greater leg width, associated with lower electrical resistance in the TEG, results in a decreased temperature of the PV. This reduction in temperature, in turn, leads to an increase in the PV power output. This relationship highlights the intricate balance between the physical dimensions of the TEG and its impact on the overall efficiency and performance of the PV-TEG system.

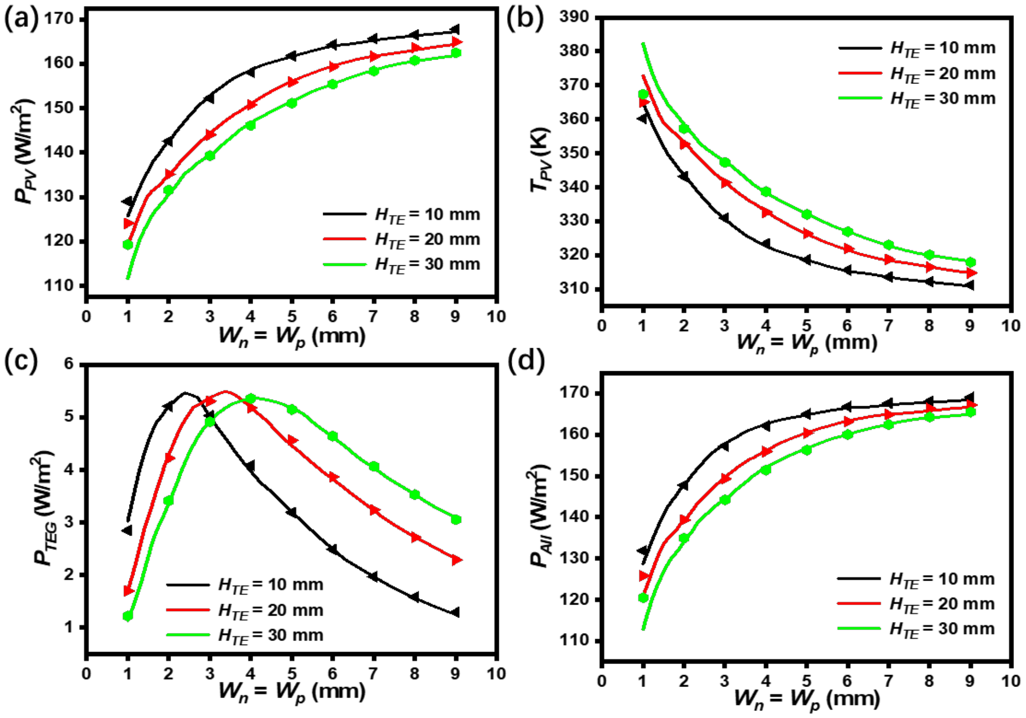

FIGURE 7.17: (a) PV power density (P_{PV}), (b) PV temperature (T_{PV}), (c) TEG power density (P_{TEG}), and (d) total power density (P_{All}) obtained from ANN (line) and COMSOL (dot) as a function of W_n, W_p and H_{TE}. Other parameters are fixed with, P_{solar}=1000W/m^2, T_{amb}=298.15K, Convection coefficient = 10 $W/(m^2K)$.

Figure 7.17c, a distinct trend is observed where P_{TEG} initially increases and then decreases as the width of the TEG leg (W_n) changes. This behaviour can be explained by examining the dynamics of electrical resistance in the system. When W_n is small, the system experiences higher electrical resistance, constraining the P_{TEG} output. As W_n increases, the electrical resistance decreases, facilitating an increase in P_{TEG}. However, beyond a certain point, as W_n becomes significantly oversized, the thermal resistance also decreases. This reduction in thermal resistance leads to a smaller temperature gradient across the TEG, resulting in a decrease in P_{TEG}. This pattern shows the complex interplay between electrical and thermal resistances in the TEG and their combined effect on its power output.

As the value of H_{TE} increased, a noticeable shift in the peak of P_{TEG} towards a higher W_n was observed. This shift can be rationalized by considering the impact of increased H_{TE} on the system's resistance. A higher H_{TE} implies greater resistance for a given W_n. To achieve a balance between thermal and electrical resistances, an increase in W_n becomes necessary. This increase in W_n effectively reduces the total resistance in the system. Figure 7.17d displays the variation in the total output power (P_{All}) of the PV-TEG system. Figure 7.17 verifies the effectiveness of this model for incorporating TEG structure parameters. Different TEG structures can be selected according to different parameters to increase the generalization of the model.

Figure 7.17 verifies the effectiveness of this model for incorporating TEG structure parameters. Different TEG structures can be selected according to various parameters to increase the generalization of the model.

7.7 PV-TEG system real-time data analysis

A primary advantage of our ANN model is its exceptional efficiency. Once the initial training phase is completed, the model can predict the performance of the PV-TEG system much more rapidly than traditional simulation tools like COMSOL. The simulation time has been dramatically reduced from 15 minutes to a mere 0.15 seconds. This significant acceleration in processing speed allows for real-time data integration into the simulation, enhancing the model's applicability and relevance in practical scenarios.

As a demonstration, we applied our ANN models to predict the potential power performance of the hybrid PV-TEG system as well as a standalone PV system with and without heat sink under real-time weather conditions in London on June 20th, 2022, for over 24 hours shown in Figure 7.18. The heat sink of the standalone PV is kept the same in the PV-TEG system. Weather conditions are based on Prediction of Worldwide Energy Resources (POWER NASA) data. The real-time data includes solar irradiance, ambient temperature, and wind speed and are presented in Figure 7.18a.

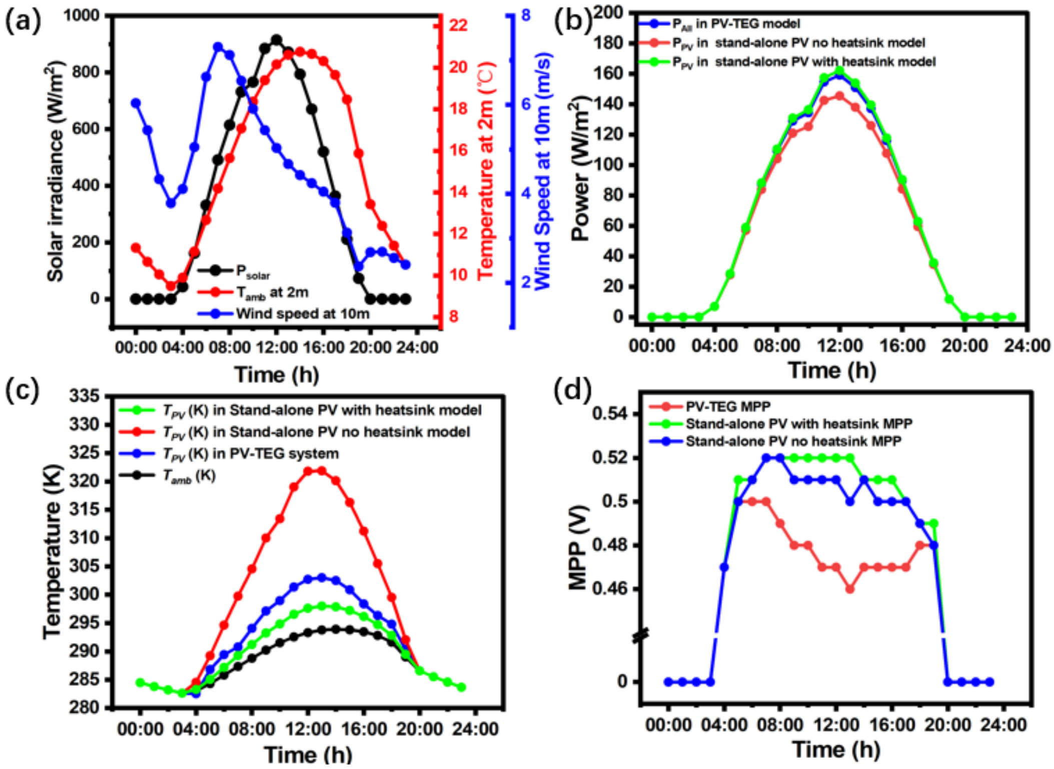

FIGURE 7.18: Real-time data of (a) Solar irradiance (P_{solar}), ambient temperature (T_{amb}) and wind speed. (b)The power performance and (c)the ambient temperature comparing T_{PV} in PV-TEG, standalone PV no heat sink and standalone PV with heat sink model. (d) PV maximum power point (MPP) voltage was obtained from ANN during the solar-powered period. The geometric parameters of the TEG remain constant, W_n=W_p=5mm, H_{TE}=10mm.

Figure 7.18b plots the total power output of the two systems over 24 hours. The findings indicate that, before 8 a.m., the variance in output between the PV-TEG and the standalone PV is negligible. By noon, this disparity amplifies, registering a maximum PV-TEG system power output of 160 W/m^2, compared to the 145 W/m^2 of the standalone PV without a heat sink and 162 W/m^2 with a heat sink. This suggests that this current structure in the PV-TEG will reduce the overall power generation.

Figure 7.18c compares the T_{PV} values of the two systems together with ambient temperature. It can be inferred that a key factor contributing to the higher power output of the PV-TEG system is the reduction in T_{PV}. The PV temperature suggests that combining TEG with PV increases the temperature of the PV when using the same heat sink. This increase in temperature causes the overall PV-TEG efficiency to decrease, as the TEGs are currently not very efficient.

Figure 7.18d showcases the PV voltage results at the highest power point under different solar irradiance levels. Leveraging the rapid computational abilities of the ANN, our model facilitates swift calculation of the voltage at the Maximum Power Point (MPP) in 0.15s, thousands of times faster than COMSOL simulation. This functionality is particularly valuable. By quickly determining the optimal operating voltage for maximum power output under varying solar conditions, the model can be instrumental in optimizing the performance of PV-TEG and standalone PV systems, leading to more energy production.

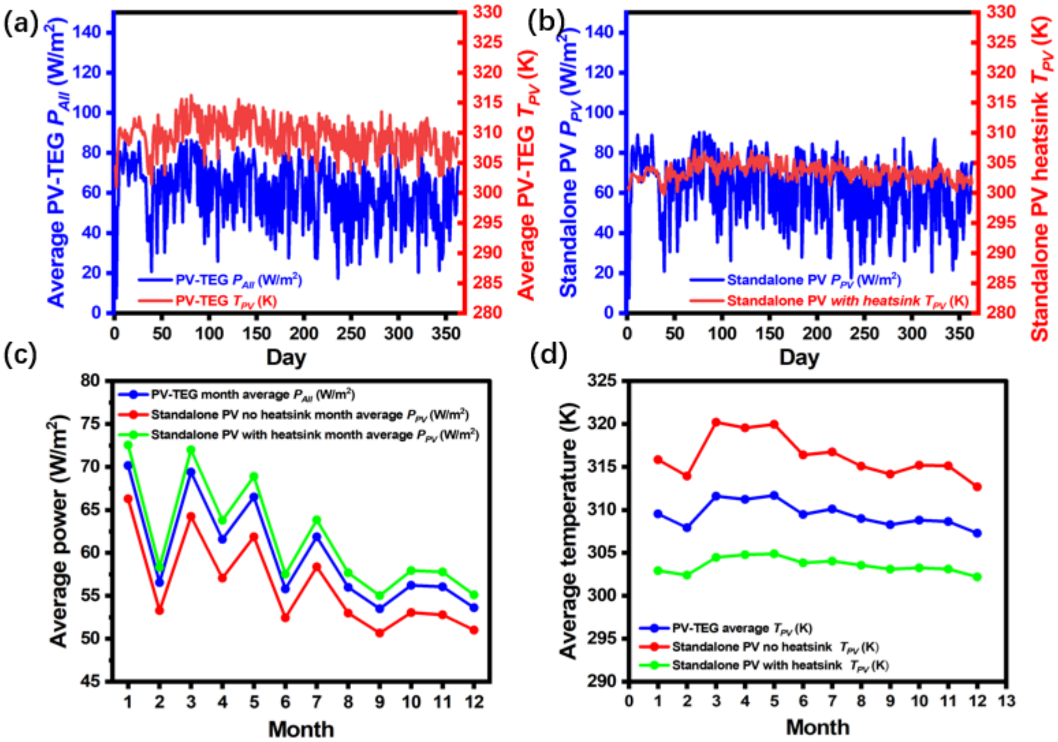

FIGURE 7.19: 365 days Real-time data simulation of (a) the integration of all output power. (b)Average PV temperature in operating times, (c) the average month output power, and (d) the average month operating temperature. Singapore from Jan 1, 2022, to Dec 31, 2022. The geometric parameters of the TEG remain constant, W_n=W_p=5mm, H_{TE}=10mm.

The real-time data simulation is now extended by introducing comprehensive weather data from Singapore, spanning the entire year of 2022 for 363 days (real-time data for the 7th and 8th of January are missing in the database). This set of data registers a total number of 8,712 entries of hourly data points.

After feeding this set of data into our ANN-based PV-TEG and PV models, both power output and operating temperature can be simulated and are presented in Figure 7.19a and Figure 7.19b. Figure 7.19c calculates the monthly average power output of the systems. It can be observed that the average output power of the PV-TEG system is higher than that of the standalone PV without heat sink system but lower than the PV with heat sink. In comparing the PV temperature with a heat sink, it is evident that the combination with the TEG causes a temperature rise. Therefore, the current PV-TEG system has limitations due to the inefficiency of the TEG in the sub-experimental TEG structure. In the future, with further development of TE materials to increase efficiency, PV-TEG systems will have more development. Additionally, other PV-TEG structures exist, such as spectrum beam splitting PV-TEG, which reflects the spectrum below the band gap to the TEG for collection [179]. This not only reduces the temperature of the

PV but also allows the TEG to recycle part of the separated heat. This structure can also be applied to the separation models studied in this chapter.

A key highlight of this study is the computational efficiency of our ANN model. It completed the power output simulation of the entire dataset in 18 minutes. In contrast, a similar number of computations based on COMSOL will necessitate a minimum of 46 days. This duration is impractical for most real-world applications, further emphasising the significant advantage of the ANN model in terms of speed and efficiency for extensive and time-sensitive simulations.

7.8 Conclusion

In this chapter, an ANN-based model has been developed to predict the performance of the hybrid PV-TEG system by employing a cyclic approach. The 3D model takes into account a wide variety of parameters, including the PV coating, morphology, TEG geometry, and temperature-dependent material properties, as well as different environmental conditions such as solar irradiance and convection. Owing to its integrated nature, the PV and TEG components in the model can also be decoupled and used independently. This adaptability significantly amplifies the versatility and generalizability of the PV-TEG model.

When benchmarked against the COMSOL simulation, this ANN model boasts an impressive accuracy of over 98%. A noteworthy enhancement in computational efficiency is achieved with a single simulation cost of only 0.15 s, representing a 6,000-fold acceleration compared with COMSOL. The swift computational abilities of the PV-TEG ANN model were fully leveraged in this study to perform extensive parameter sweeps across PV, environment, and TEG parameters. This thorough analysis facilitated a detailed exploration of how various parameters impact the performance of the PV-TEG model. The rapid processing capability of the model is especially important for large-scale simulations and real-world applications, where timely and accurate predictions are essential.

Chapter 8

Conclusions and future work

8.1 Conclusions

This project demonstrates the application of machine learning techniques in the forward modelling of TEG power performance, achieving over 98% prediction accuracy with ANNs trained on 3D COMSOL simulation data. The ANN models effectively handle constant temperature differences and heat flux conditions, incorporating complex thermoelectric effects like electrical contact resistance and surface heat transfer. Analytical studies using these networks align closely with COMSOL simulation results, validating the networks' performance.

Integrating ANNs with GAs for design optimization has shown superior efficiency, outperforming COMSOL simulations and GA optimization on average by over 1,000 times. This improvement shows the potential of machine learning in modelling and optimizing TEGs of various architectures and other energy harvesting technologies.

Further extending our work to more complex TEG structures, segmented TEG, an iterative training strategy improved the prediction accuracy for high-power STEG designs. It achieved over 4,000 times faster optimization than the conventional finite element method. This approach significantly enhances design optimization and parameter analysis efficiency, enabling rapid parametric sweep and revealing critical relationships between STEG power output and segment material ratios.

A systematic analysis of RC-TEG devices highlighted the importance of environmental conditions and TEG parameters on performance. Real-time environmental data analysis demonstrated RC-TEG's capability for continuous power supply around 160 mW/m^2, suitable for IoT devices.

Additionally, a PV-TEG model developed using ANNs showcased impressive accuracy (98%) and computational efficiency (6000 times faster), drastically reducing simulation time compared to COMSOL simulations. This model's flexibility and rapid computational abilities facilitate extensive parameter sweeps, offering deep insights into the performance impacts of various parameters. The current PV-TEG model is not as effective as expected due to the low efficiency of TEGs. However, with the development of more efficient TEGs in the future, the PV-TEG model will become more feasible. Meanwhile, other structures of PV-TEG systems are also being studied by many researchers, indicating that PV-TEG still has a high development potential.

Overall, the application of ANNs in this research not only achieves high accuracy and computational efficiency in modelling and optimization but also opens new avenues for designing and optimizing complex energy harvesting technologies, demonstrating the practical utility and effectiveness of machine learning in renewable energy technology. The current limitation of ANN is the acquisition of datasets. Generating datasets takes a lot of time for models that run very slowly. For many models, spending significant time training a fast ANN may not be cost-effective. Therefore, there is still a trade-off in deciding whether an ANN is needed to replace the original model. In the future, more research is needed to improve the efficiency of dataset generation.

8.2 Future work

In this project, the modelling of TEGs primarily focused on structural and environmental parameters. Future works could broaden these parameters to incorporate a variety of TE materials. Some thermoelectric studies have been based on phase change materials. Therefore, it will be interesting to see how more complex materials can be combined into artificial neural networks.

Furthermore, developing a parameter that encapsulates the properties of these diverse TE materials could further enhance the versatility of the TEG model, enabling it to cover a wider array of scenarios. In addition, exploring TEGs with alternative structures presents another promising direction for future modelling efforts. This could extend to incorporating parameters for curved structures, thereby broadening the utility of TEG models in practical scenarios, such as in water pipes.

Similarly, beyond the segmented thermoelectric generator, of which I've only modelled two segments here, incorporating more layers is theoretically feasible. With different material choices, one could model and optimize a layered thermoelectric generator with more layers. This multilayered STEG theoretically has better efficiency, allowing for the exploration of various combinations and variations of materials.

Additionally, the modelling of thermoelectric coolers represents a promising avenue for future research. Utilizing the same principles as TEGs, the modelling process for thermoelectric coolers is expected to be quite similar. Such modelling could facilitate the exploration of how varying the current affects the cooling capabilities of thermoelectric coolers. By modelling thermoelectric coolers, it becomes possible to control the current in real-time, thereby adjusting the temperature of the cold end. This capability opens up numerous practical applications for thermoelectric coolers, including on-chip cooling, car refrigerators, etc.

Appendix A

Code of the project

A.1 Conventional Bulk TEG Python code

Code related to ANN training and GA has been added here. Other code and specific datasets can be downloaded from the GitHub links https://github.com/LorewalkerZYX/Bulk-TEG-project.git.

A.1.1 ANN training python script

```
# TEG Constant TH experiment
# Available on https://github.com/LorewalkerZYX/Bulk-TEG-project.git


import pandas as pd
import numpy as np
import random
import torch
import torch.nn as nn
import torch.utils.data as Data
import xlsxwriter


# Set the random seed manually for reproducibility.
def seed_torch(seed=1029):
    torch.manual_seed(seed)
    torch.cuda.manual_seed(seed)
    torch.cuda.manual_seed_all(seed)  # if you are using multi-GPU.
    torch.backends.cudnn.benchmark = False
```

```
    torch.backends.cudnn.deterministic = True
    random.seed(seed)
    np.random.seed(seed)


seed_torch(10)
device = torch.device('cuda:0')


def LoadData():
    # preparing data
    data_X = pd.read_excel('input2.xlsx')
    data_Y = pd.read_excel('Output4.2.xlsx')
    dataX = data_X.iloc[:, :]

    dataY = data_Y.iloc[:, 0:3:2]
    X_train = dataX.to_numpy()
    Y_train = dataY.to_numpy()
    return X_train, Y_train


# const = 100000


# normalization
def normalize_x(x, input=True):
    temp = x

    if input:
        wn = 4.5  # wn = [0.5-5]
        wp = 4.5  # wp = [0.5-5]
        h = 4.5  # h = [0.5-5]
        h_ic = 2.5  # h_ic = [0.5-3]
        ff = 0.9  # ff = [0.05-0.95]
        t_h = 200  # T_H = [300-500]
        rho_c = 9.9E-8  # rho_c = [1E-9-1E-7]

        for i in range(len(temp)):
            temp[i, 0] = (temp[i, 0] - 0.5) / wn
            temp[i, 1] = (temp[i, 1] - 0.5) / wp
            temp[i, 2] = (temp[i, 2] - 0.5) / h
```

```
            temp[i, 3] = (temp[i, 3] - 0.5) / h_ic
            temp[i, 4] = (temp[i, 4] - 0.05) / ff
            temp[i, 5] = (temp[i, 5] - 300) / t_h
            temp[i, 6] = (temp[i, 6] - 1E-9) / rho_c

    else:
        for k in range(len(temp)):
            temp[k][0] = np.log(temp[k][0])
            temp[k][0] = (temp[k][0] - Mp) / Sp
            temp[k][1] = np.log(temp[k][1])
            temp[k][1] = (temp[k][1] - Me) / Se
    return temp


def recover_y(y):
    # y /= const
    for i in range(len(y)):
        y[i, 0] = y[i, 0] * Sp + Mp
        y[i, 1] = y[i, 1] * Se + Me
    outy = np.exp(y)
    return outy


def train_dev_split(X, Y, dev_ratio=0.25):
    size = int(len(X) * (1 - dev_ratio))
    label = np.array(range(len(X)))
    SelectT = random.sample(range(len(X)), size)  # np.random.randint(0, len(X) - 1,
    train_x = X[SelectT]
    train_y = Y[SelectT]
    SelectV = np.delete(label, SelectT)
    valid_x = X[SelectV]
    valid_y = Y[SelectV]
    # print(len(label), len(SelectT), len(SelectV))
    # return X[:size], Y[:size], X[size:], Y[size:]
    return train_x, train_y, valid_x, valid_y


[X_train, Y_train] = LoadData()

# Preparing the data
dev_ratio = 0.1
```

```
Train_x, Train_y, test_x, test_y = train_dev_split(X_train, Y_train, dev_ratio)

trainx, trainy, validx, validy = train_dev_split(Train_x, Train_y, dev_ratio)

testing_x = test_x.copy()
testing_y = test_y.copy()

Mp = -2.543717849328878  # -3.236864469716249
Sp = 1.956137781915298
Mq = 8.401629926494419
Sq = 1.050063542837697
Me = -4.730739701517070
Se = 1.175501917388629

trainx = normalize_x(trainx)
validx = normalize_x(validx)
testx = normalize_x(test_x)
trainy = normalize_x(trainy, False)
validy = normalize_x(validy, False)
Y_test = normalize_x(test_y, False)


# dataset
train_size = trainx.shape[0]
valid_size = validx.shape[0]

Batch_size = 64
epoch = 2000
learning_rate = 0.001
hidden_layers = 5
hidden_feature = 20
n = 0
step = 1
# print(train_size, valid_size)

# trainsfer numpy to torch
x = torch.from_numpy(trainx)
x = x.type(torch.FloatTensor)

y = torch.from_numpy(trainy)
y = y.type(torch.FloatTensor)
```

```
X_dev = torch.from_numpy(validx)
X_dev = X_dev.type(torch.FloatTensor)

Y_dev = torch.from_numpy(validy)
Y_dev = Y_dev.type(torch.FloatTensor)

train_data = Data.TensorDataset(x, y)
val_data = Data.TensorDataset(X_dev, Y_dev)

X_test = torch.from_numpy(testx)
X_test = X_test.type(torch.FloatTensor)

'''Y_test = torch.from_numpy(Y_test)
Y_test = Y_test.type(torch.FloatTensor)'''

loader = Data.DataLoader(
    dataset=train_data,
    batch_size=Batch_size,
    shuffle=True,
)

val_loader = Data.DataLoader(
    dataset=val_data,
    batch_size=Batch_size,
    shuffle=False
)



# create net
class Net(torch.nn.Module):
    def __init__(self, n_feature, n_hidden, n_output, n_layer):
        super(Net, self).__init__()
        self.input = nn.Linear(n_feature, n_hidden)
        self.relu = nn.ReLU()
        self.hidden = nn.Linear(n_hidden, n_hidden)
        self.dropout = nn.Dropout(p=0.5)
        self.out = nn.Linear(n_hidden, n_output)
        self.layernum = n_layer

    def forward(self, x):
```

```
        out = self.input(x)
        out = self.relu(out)
        for i in range(self.layernum):
            out = self.hidden(out)
            out = self.relu(out)
        out = self.out(out)
        return out


seed_torch(58)  # 58
Loss_Function = nn.MSELoss()

net = Net(7, hidden_feature, 2, hidden_layers)
net = net.to(device)
optimzer = torch.optim.Adam(
    net.parameters(),
    lr=learning_rate
    # weight_decay=0.001
)

stepsize = [1800, 1900]

scheduler = torch.optim.lr_scheduler.MultiStepLR(
    optimizer=optimzer,
    milestones=stepsize,
    gamma=0.1
)

# save in excel
workbook = xlsxwriter.Workbook('train_result_error_N%dL%dSeed=58.xlsx' %
                               (hidden_feature, hidden_layers))
worksheet = workbook.add_worksheet()
# worksheet2 = workbook.add_worksheet()


worksheet.write('A1', 'epoch')
worksheet.write('B1', 'training loss')
worksheet.write('C1', 'validation loss')
worksheet.write('D1', 'Test Power Data')
worksheet.write('E1', 'Test Efficiency Data')
worksheet.write('F1', 'Predict Power Data')
```

```
worksheet.write('G1', 'Predict Efficiency Data')
worksheet.write('H1', 'Power Relative error')
worksheet.write('I1', 'Efficiency Relative error')
worksheet.write('J1', 'Power Average Relative error')
worksheet.write('K1', 'Efficiency Average Relative error')


def TrainGA(epoch):
    # seed_torch(sd)
    for i in range(epoch):
        train_loss = 0.0
        # val_loss = 0.0
        temp_loss = 0.0
        temp_val = 0.0

        net.train()
        for num, (batch_x, batch_y) in enumerate(loader):
            optimzer.zero_grad()
            out = net(batch_x.to(device))
            loss = Loss_Function(out, batch_y.to(device))
            loss.backward()
            optimzer.step()
            temp_loss += loss.item()
        scheduler.step()
        train_loss = temp_loss / (train_size / Batch_size)
        net.eval()
        with torch.no_grad():
            for epnum, (val_x, val_y) in enumerate(val_loader):
                val_out = net(val_x.to(device))
                dev_loss = Loss_Function(val_out, val_y.to(device))
                temp_val += dev_loss.cpu().data.numpy()

        val_loss = temp_val / (valid_size / Batch_size)
        print('epoch: %d' % i, 'training loss:', train_loss, '|',
              'validation loss:', val_loss)
        worksheet.write(i + 1, 0, i + 1)
        worksheet.write(i + 1, 1, train_loss)
        worksheet.write(i + 1, 2, val_loss)
    return train_loss
```

```
# start training
TrainGA(epoch)

# test data
test_out = net(X_test.to(device))
t_out = test_out.cpu().data.numpy()

Predict_y = recover_y(t_out)

lengthT = len(t_out)
Ap = 0
Aq = 0
for j in range(lengthT):
    worksheet.write(j + 1, 3, testing_y[j, 0])
    worksheet.write(j + 1, 4, testing_y[j, 1])
    worksheet.write(j + 1, 5, Predict_y[j, 0])
    worksheet.write(j + 1, 6, Predict_y[j, 1])
    RelativeE_P = np.abs(Predict_y[j, 0] - testing_y[j, 0]) / testing_y[j, 0]
    RelativeE_Q = np.abs(Predict_y[j, 1] - testing_y[j, 1]) / testing_y[j, 1]
    worksheet.write(j + 1, 7, RelativeE_P)
    worksheet.write(j + 1, 8, RelativeE_Q)
    Ap += RelativeE_P
    Aq += RelativeE_Q

Aq /= lengthT
Ap /= lengthT
worksheet.write(1, 9, Ap)
worksheet.write(1, 10, Aq)
# print(temp1)
workbook.close()
# torch.save(net.state_dict(), 'TEGNetP4_V2.pkl')
```

A.1.2 ANN GA script

```
# TEG Constant TH GA experiment
# Available on https://github.com/LorewalkerZYX/Bulk-TEG-project.git

import pandas as pd
import matplotlib.pyplot as plt
import numpy as np
import torch
```

```
import torch.nn as nn
from sko.GA import GA
import xlsxwriter

Batch_size = 64
epoch = 2000
learning_rate = 0.001
hidden_feature = 400
Mp = -2.543717849328878
Sp = 1.956137781915298
Mq = 8.401629926494419
Sq = 1.050063542837697
Me = -4.730739701517070
Se = 1.175501917388629


# Set the random seed manually for reproducibility.
def seed_torch(seed=1029):
    torch.manual_seed(seed)
    torch.cuda.manual_seed(seed)
    torch.cuda.manual_seed_all(seed)  # if you are using multi-GPU.
    torch.backends.cudnn.benchmark = False
    torch.backends.cudnn.deterministic = True
    # random.seed(seed)
    np.random.seed(seed)


seed_torch(0)  # 30,


def recover_y(y):
    y[0] = y[0] * Sp + Mp
    y[1] = y[1] * Se + Me
    outy = np.exp(y)
    return outy


def selection_tournament(self, tourn_size=4):
    '''
    Select the best individual among *tournsize* randomly chosen
    individuals,
```

```
    :param self:
    :param tourn_size:
    :return:
    '''
    FitV = self.FitV
    sel_index = []
    for i in range(self.size_pop):
        aspirants_index = np.random.choice(range(self.size_pop), size=tourn_size)
        # aspirants_index = np.random.randint(self.size_pop, size=tourn_size)
        sel_index.append(max(aspirants_index, key=lambda i: FitV[i]))
    self.Chrom = self.Chrom[sel_index, :]  # next generation
    return self.Chrom


def ranking(self):
    # GA select the biggest one, but we want to minimize func, so we put a negative here
    self.FitV = (self.Y - np.argmin(self.Y))  # self.Y  # [np.argsort(1 - self.Y)]
    return self.FitV


# create net
class Net(torch.nn.Module):
    def __init__(self, n_feature, n_hidden, n_output, n_layer):
        super(Net, self).__init__()
        self.input = nn.Linear(n_feature, n_hidden)
        self.relu = nn.ReLU()
        self.hidden = nn.Linear(n_hidden, n_hidden)
        self.dropout = nn.Dropout(p=0.5)
        self.out = nn.Linear(n_hidden, n_output)
        self.layernum = n_layer

    def forward(self, x):
        out = self.input(x)
        out = self.relu(out)
        for i in range(self.layernum):
            out = self.hidden(out)
            out = self.relu(out)
        out = self.out(out)
        return out
```

```
TEG_NET = Net(7, hidden_feature, 2, 5)
TEG_NET.load_state_dict(torch.load('TEGNetP4_V2.pkl'))



# normalization
def normalize_x(x, input=True):
    temp = x

    if input:
        wn = 4.5  # wn = [0.5-5]
        wp = 4.5  # wp = [0.5-5]
        h = 4.5  # h = [0.5-5]
        h_ic = 2.5  # h_ic = [0.5-3]
        ff = 0.9  # ff = [0.05-0.95]
        t_h = 200  # T_H = [300-500]
        rho_c = 9.9E-8  # rho_c = [1E-9-1E-7]

        for i in range(len(temp)):
            temp[i, 0] = (temp[i, 0] - 0.5) / wn
            temp[i, 1] = (temp[i, 1] - 0.5) / wp
            temp[i, 2] = (temp[i, 2] - 0.5) / h
            temp[i, 3] = (temp[i, 3] - 0.5) / h_ic
            temp[i, 4] = (temp[i, 4] - 0.05) / ff
            temp[i, 5] = (temp[i, 5] - 300) / t_h
            temp[i, 6] = (temp[i, 6] - 1E-9) / rho_c

    else:
        for k in range(len(temp)):
            temp[k][0] = np.log(temp[k][0])
            temp[k][0] = (temp[k][0] - Mp) / Sp
            temp[k][1] = np.log(temp[k][1])
            temp[k][1] = (temp[k][1] - Me) / Se
    return temp



def normalize_new(x, input=True):
    temp = x
    wn = 4.5  # wn = [0.5-5]
    wp = 4.5  # wp = [0.5-5]
    h = 4.5  # h = [0.5-5]
    h_ic = 2.5  # h_ic = [0.5-3]
```

```
    ff = 0.9  # ff = [0.05-0.95]
    t_h = 200  # T_H = [300-500]
    rho_c = 9.9E-8  # rho_c = [1E-9-1E-7]
    temp[0] = (temp[0] - 0.5) / wn
    temp[1] = (temp[1] - 0.5) / wp
    temp[2] = (temp[2] - 0.5) / h
    temp[3] = (temp[3] - 0.5) / h_ic
    temp[4] = (temp[4] - 0.05) / ff
    temp[5] = (temp[5] - 300) / t_h
    temp[6] = (temp[6] - 1E-9) / rho_c
    return temp


# denormalization
def denormalize_x(x):
    temp = x.copy()
    wn = 4.5  # wn = [0.5-5]
    wp = 4.5  # wp = [0.5-5]
    h = 4.5  # h = [0.5-5]
    h_ic = 2.5  # h_ic = [0.5-3]
    ff = 0.9  # ff = [0.05-0.95]
    # q_in = 4000  # q_in = [1000-5000]
    # rho_c = 9.9E-8  # rho_c = [1E-9-1E-7]

    temp[0] = temp[0] * wn + 0.5
    temp[1] = temp[1] * wp + 0.5
    temp[2] = temp[2] * h + 0.5
    temp[3] = temp[3] * h_ic + 0.5
    temp[4] = temp[4] * ff + 0.05
    # temp[5] = temp[5] * q_in + 1000
    # temp[6] = temp[6] * rho_c + 1E-9

    return temp


Th = 0.5  # Th = 400
R_c = 1/11  # Rho_c = 1E-8

T_H = 400
Rhoc = 1E-8
```

```
def demo_func(x):
    # print(x[0, :])
    # x.reshape(4, 300)
    # temp = normalize_x(x)
    y = x / 100
    In = np.append(y, T_H)
    InputX = np.append(In, Rhoc)
    InputX = normalize_new(InputX)
    temp = torch.Tensor(InputX)
    # x1, x2, x3, x4 = temp
    # InX = normalize_new(temp)
    # print(InX)
    result = TEG_NET(temp)
    tempy = result.cpu().data.numpy()
    outy = recover_y(tempy)[1]
    return outy


all_history_X = []


def maxrun(self, max_iter=None):
    self.max_iter = max_iter or self.max_iter
    for i in range(self.max_iter):
        self.X = self.chrom2x(self.Chrom)
        self.Y = self.x2y()
        self.ranking()
        self.selection()
        self.crossover()
        self.mutation()

        # record the best ones
        generation_best_index = self.FitV.argmax()
        self.generation_best_X.append(self.X[generation_best_index, :])
        self.generation_best_Y.append(self.Y[generation_best_index])
        self.all_history_Y.append(self.Y)
        self.all_history_FitV.append(self.FitV)
        all_history_X.append(self.X)

    global_best_index = np.array(self.generation_best_Y).argmax()
```

```
    self.best_x = self.generation_best_X[global_best_index]
    self.best_y = self.func(np.array([self.best_x]))
    return self.best_x, self.best_y


leastB = [0, 0, 0, 0, 0]
MostB = [1, 1, 1, 1, 1]

leastB1 = [50, 50, 50, 50, 5]
MostB1 = [500, 500, 500, 300, 95]
# wn, wp, H, hic, ff
#
ga = GA(
    func=demo_func,
    n_dim=5, size_pop=100,
    max_iter=200,
    lb=leastB1,
    ub=MostB1,
    precision=1
)
# ga.register(operator_name='selection', operator=selection_tournament)
ga.register(operator_name='ranking', operator=ranking)

GA.run = maxrun


best_x, best_y = ga.run()
# origin_x = denormalize_x(best_x)
# print(origin_x)
print(best_x)
print(best_x/100)
print(best_y)

Y_history = pd.DataFrame(ga.all_history_Y)
# X_history = pd.DataFrame(all_history_X[199])

# print(History_values[:, 0])

# save in excel
workbook = xlsxwriter.Workbook('MaxGA_200G_Eff_All_X.xlsx')
worksheet = workbook.add_worksheet()
```

```
worksheet.write('A1', 'Numbers')
worksheet.write('B1', 'Wn')
worksheet.write('C1', 'Wp')
worksheet.write('D1', 'H')
worksheet.write('E1', 'Hic')
worksheet.write('F1', 'FF')
# length = len(History_values)
for i in range(200):
    X_history = pd.DataFrame(all_history_X[i])
    History_index = X_history.index
    History_values = X_history.values
    # worksheet.write(i+1, 1, np.max(History_values[i]))
    for j in range(100):
        worksheet.write(100*i+j+1, 0, 100*i+j+1)
        worksheet.write(100*i+j+1, 1, History_values[j, 0]/100)
        worksheet.write(100*i+j+1, 2, History_values[j, 1]/100)
        worksheet.write(100*i+j+1, 3, History_values[j, 2]/100)
        worksheet.write(100*i+j+1, 4, History_values[j, 3]/100)
        worksheet.write(100*i+j+1, 5, History_values[j, 4]/100)
workbook.close()
```

A.2 Segmented TEG Python script

Code of entire project with dataset can be downloaded from the GitHub links `https://github.com/LorewalkerZYX/Segmented-TEG-Project.git`.

A.3 PV-TEG Python script

Code of entire project with dataset can be downloaded from the GitHub links `https://github.com/LorewalkerZYX/Photovoltaic-TEG-Project.git`.

References

[1] Robert Freer and Anthony V. Powell. Realising the potential of thermoelectric technology: A Roadmap, 2020. `doi:10.1039/c9tc05710b`.

[2] IEA. Net zero by 2050 (2021), Global Energy Review 2021, https://www.iea.org/reports/net-zero-by-2050, 2021. URL: `https://www.iea.org/reports/net-zero-by-2050`.

[3] G Jeffrey Snyder and Eric S Toberer. Complex Thermoelectric Materials. *Nature Materials*, 7(2):105–114, feb 2008. `doi:10.1038/nmat2090`.

[4] Samson Shittu, Guiqiang Li, Xudong Zhao, and Xiaoli Ma. Review of thermoelectric geometry and structure optimization for performance enhancement. *Applied Energy*, 268(May):115075, 2020. `doi:10.1016/j.apenergy.2020.115075`.

[5] Terry M. Tritt. Thermoelectric Phenomena, Materials, and Applications. *Annual Review of Materials Research*, 41(1):433–448, aug 2011. `doi:10.1146/annurev-matsci-062910-100453`.

[6] Seyed Mohsen Pourkiaei, Mohammad Hossein Ahmadi, M. Sadeghzadeh, Soroush Moosavi, Fathollah Pourfayaz, Lingen Chen, Mohammad Arab Pour Yazdi, and Ravinder Kumar. Thermoelectric Cooler and Thermoelectric Generator Devices: A Review of Present and Potential Applications, Modeling and Materials. *Energy*, 186:115849, 2019. `doi:10.1016/j.energy.2019.07.179`.

[7] Daniel Champier. Thermoelectric generators: A Review of Applications. *Energy Conversion and Management*, 140:167–181, 2017. `doi:10.1016/j.enconman.2017.02.070`.

[8] D. T. Crane. An introduction to system-level, steady-state and transient modeling and optimization of high-power-density thermoelectric generator devices made of segmented thermoelectric elements. *Journal of Electronic Materials*, 40(5):561–569, 2011. `doi:10.1007/s11664-010-1451-6`.

[9] Zhen Chen, Linxiao Zhu, Wei Li, and Shanhui Fan. Simultaneously and Synergistically Harvest Energy from the Sun and Outer Space. *Joule*, 3(1):101–110, 2019. `doi:10.1016/j.joule.2018.10.009`.

[10] Aaswath P. Raman, Marc Abou Anoma, Linxiao Zhu, Eden Rephaeli, and Shanhui Fan. Passive radiative cooling below ambient air temperature under direct sunlight. *Nature*, 515(7528):540–544, 2014. `doi:10.1038/nature13883`.

[11] Vikas Khare, Savita Nema, and Prashant Baredar. Solar-wind hybrid renewable energy system: A review. *Renewable and Sustainable Energy Reviews*, 58:23–33, 2016. `doi:10.1016/j.rser.2015.12.223`.

[12] Ahmet Z. Sahin, Kehinde G. Ismaila, Bekir S. Yilbas, and Abdullah Al-Sharafi. A review on the performance of photovoltaic/thermoelectric hybrid generators. *International Journal of Energy Research*, 44(5):3365–3394, 2020. `doi:10.1002/er.5139`.

[13] Swapnil Dubey, Jatin Narotam Sarvaiya, and Bharath Seshadri. Temperature dependent photovoltaic (PV) efficiency and its effect on PV production in the world - A review. In *Energy Procedia*, volume 33, pages 311–321. Elsevier B.V., 2013. `doi:10.1016/j.egypro.2013.05.072`.

[14] Abdul Rehman Jatoi, Saleem Raza Samo, and Abdul Qayoom Jakhrani. Influence of temperature on electrical characteristics of different photovoltaic module technologies. *International Journal of Renewable Energy Development*, 7(2):85–91, 2018. `doi:10.14710/ijred.7.2.85-91`.

[15] Li Dong Zhao, Shih Han Lo, Yongsheng Zhang, Hui Sun, Gangjian Tan, Ctirad Uher, C. Wolverton, Vinayak P. Dravid, and Mercouri G. Kanatzidis. Ultralow thermal conductivity and high thermoelectric figure of merit in SnSe crystals. *Nature*, 508(7496):373–377, 2014. `doi:10.1038/nature13184`.

[16] Zohreh Soleimani, Stamatis Zoras, Boris Ceranic, Sally Shahzad, and Yuanlong Cui. A review on recent developments of thermoelectric materials for room-temperature applications. *Sustainable Energy Technologies and Assessments*, 37(December 2019):100604, 2020. `doi:10.1016/j.seta.2019.100604`.

[17] N. Neophytou, S. Foster, V. Vargiamidis, G. Pennelli, and D. Narducci. Nanostructured potential well/barrier engineering for realizing unprecedentedly large thermoelectric power factors. *Materials Today Physics*, 11:100159, 2019. `doi:10.1016/j.mtphys.2019.100159`.

[18] Weishu Liu, Jizhen Hu, Shuangmeng Zhang, Manjiao Deng, Cheng Gong Han, and Yong Liu. New trends, strategies and opportunities in thermoelectric materials: A perspective, 2017. `doi:10.1016/j.mtphys.2017.06.001`.

[19] Lei Yang, Zhi Gang Chen, Matthew S. Dargusch, and Jin Zou. High Performance Thermoelectric Materials: Progress and Their Applications, 2018. `doi:10.1002/aenm.201701797`.

[20] Maryam M. Najafabadi, Flavio Villanustre, Taghi M. Khoshgoftaar, Naeem Seliya, Randall Wald, and Edin Muharemagic. Deep Learning Applications and Challenges in Big Data Analytics. *Journal of Big Data*, 2(1):1–21, 2015. `doi:10.1186/s40537-014-0007-7`.

[21] Athanasios Voulodimos, Nikolaos Doulamis, Anastasios Doulamis, and Eftychios Protopapadakis. Deep Learning for Computer Vision: A Brief Review. *Computational Intelligence and Neuroscience*, 2018. `doi:10.1155/2018/7068349`.

[22] Ali Bou Nassif, Ismail Shahin, Imtinan Attili, Mohammad Azzeh, and Khaled Shaalan. Speech Recognition Using Deep Neural Networks: A Systematic Review. *IEEE Access*, 7:19143–19165, 2019. `doi:10.1109/ACCESS.2019.2896880`.

[23] Sunae So, Trevon Badloe, Jaebum Noh, Jorge Bravo-Abad, and Junsuk Rho. Deep learning enabled inverse design in nanophotonics. *Nanophotonics*, 9(5):1041–1057, feb 2020. `doi:10.1515/nanoph-2019-0474`.

[24] Peter R. Wiecha, Arnaud Arbouet, Christian Girard, and Otto L. Muskens. Deep Learning in Nano-photonics: Inverse Design and Beyond. *Photonics Research*, 9(5):B182, jan 2021. `doi:10.1364/prj.415960`.

[25] Wei Ma, Feng Cheng, and Yongmin Liu. Deep-Learning-Enabled On-Demand Design of Chiral Metamaterials. *ACS Nano*, 12(6):6326–6334, 2018. `doi:10.1021/acsnano.8b03569`.

[26] Lei Xu, Mohsen Rahmani, Yixuan Ma, Daria A. Smirnova, Khosro Zangeneh Kamali, Fu Deng, Yan Kei Chiang, Lujun Huang, Haoyang Zhang, Stephen Gould, Dragomir N. Neshev, and Andrey E. Miroshnichenko. Enhanced light–matter interactions in dielectric nanostructures via machine-learning approach. *Advanced Photonics*, 2(02):1, apr 2020. `doi:10.1117/1.AP.2.2.026003`.

[27] Li Gao, Xiaozhong Li, Dianjing Liu, Lianhui Wang, and Zongfu Yu. A Bidirectional Deep Neural Network for Accurate Silicon Color Design. *Advanced Materials*, 31(51):1905467, dec 2019. `doi:10.1002/adma.201905467`.

[28] Peng Dai, Yasi Wang, Yueqiang Hu, C. de Groot, Otto Muskens, Huigao Duan, and Ruomeng Huang. Accurate inverse design of Fabry–Pérot-Cavity-based color filters far beyond sRGB via a bidirectional artificial neural network. *Photonics Research*, 9(5):236–246, 2021. `doi:10.1364/prj.415141`.

[29] Jonathan Schmidt, Mário R.G. Marques, Silvana Botti, and Miguel A.L. Marques. Recent advances and applications of machine learning in solid-state materials science. *npj Computational Materials*, 5(1), 2019. `doi:10.1038/s41524-019-0221-0`.

[30] Yue Liu, Tianlu Zhao, Wangwei Ju, Siqi Shi, Siqi Shi, and Siqi Shi. Materials discovery and design using machine learning. *Journal of Materiomics*, 3(3):159–177, 2017. `doi:10.1016/j.jmat.2017.08.002`.

[31] Tian Wang, Cheng Zhang, Hichem Snoussi, and Gang Zhang. Machine Learning Approaches for Thermoelectric Materials Research. *Advanced Functional Materials*, 30(5):1–14, 2020. `doi:10.1002/adfm.201906041`.

[32] Zhi Lei Wang, Yuuki Yokoyama, Tetsuhiko Onda, Yoshitaka Adachi, and Zhong Chun Chen. Improved Thermoelectric Properties of Hot-Extruded BiTeSe Bulk Materials with Cu Doping and Property Predictions via Machine Learning. *Advanced Electronic Materials*, 5(6), 2019. `doi:10.1002/aelm.201900079`.

[33] Brian Kolb, Levi C. Lentz, and Alexie M. Kolpak. Discovering Charge Density Functionals and Structure-property Relationships with PROPhet: A general Framework for Coupling Machine Learning and First-principles Methods. *Scientific Reports*, 7(1):1–9, 2017. `doi:10.1038/s41598-017-01251-z`.

[34] Yuxiao Zhu, Daniel W. Newbrook, Peng Dai, C.H. Kees de Groot, and Ruomeng Huang. Artificial Neural Network Enabled Accurate Geometrical Design and Optimisation of Thermoelectric Generator. *Applied Energy*, 305:117800, jan 2022. `doi:10.1016/j.apenergy.2021.117800`.

[35] Wei He, Gan Zhang, Xingxing Zhang, Jie Ji, Guiqiang Li, and Xudong Zhao. Recent development and application of thermoelectric generator and cooler. *Applied Energy*, 143:1–25, 2015. `doi:10.1016/j.apenergy.2014.12.075`.

[36] Eliseo Ruiz, Santiago Alvarez, and Pere Alemany. Electronic structure and properties of aln. *Phys. Rev. B*, 49:7115–7123, Mar 1994. `doi:10.1103/PhysRevB.49.7115`.

[37] Maarten A.T.M. Broekmans. Structural properties of quartz and their potential role for asr. *Materials Characterization*, 53(2):129–140, 2004. EMABM 2003: 9th Euroseminar on Microscopy Applied to Building Materials. `doi:10.1016/j.matchar.2004.08.010`.

[38] Mohamed Hamid Elsheikh, Dhafer Abdulameer Shnawah, Mohd Faizul Mohd Sabri, Suhana Binti Mohd Said, Masjuki Haji Hassan, Mohamed Bashir Ali Bashir, and Mahazani Mohamad. A review on thermoelectric renewable energy: Principle parameters that affect their performance. *Renewable and Sustainable Energy Reviews*, 30:337–355, 2014. `doi:10.1016/j.rser.2013.10.027`.

[39] Samson Shittu, Guiqiang Li, Qindong Xuan, Xin Xiao, Xudong Zhao, Xiaoli Ma, and Yousef Golizadeh Akhlaghi. Transient and non-uniform heat flux effect on solar thermoelectric generator with phase change material. *Applied Thermal Engineering*, 173(March):115206, 2020. `doi:10.1016/j.applthermaleng.2020.115206`.

[40] Dongliang Zhao, Xin Qian, Xiaokun Gu, Saad Ayub Jajja, and Ronggui Yang. Measurement Techniques for Thermal Conductivity and Interfacial Thermal Conductance of Bulk and Thin Film Materials. *Journal of Electronic Packaging*, 138(4):040802, 10 2016. `doi:10.1115/1.4034605`.

[41] Giri Joshi, Tulashi Dahal, Shuo Chen, Hengzhi Wang, Junichiro Shiomi, Gang Chen, and Zhifeng Ren. Enhancement of thermoelectric figure-of-merit at low temperatures by titanium substitution for hafnium in n-type half-Heuslers Hf0.75-xTixZr0.25NiSn0.99Sb0.01. *Nano Energy*, 2(1):82–87, 2013. `doi:10.1016/j.nanoen.2012.07.020`.

[42] R. D. Rogers and A. H. Bond. Structure of [Ca(triethylene glycol)2]Cl2.4H2O. *Acta Crystallographica Section C Crystal Structure Communications*, 48(10):1782–1785, 1992. `doi:10.1107/s010827019200235x`.

[43] Jian Liu, Li Qiu, Riccardo Alessandri, Xinkai Qiu, Giuseppe Portale, Jing Jin Dong, Wytse Talsma, Gang Ye, Aprizal Akbar Sengrian, Paulo C.T. Souza, Maria Antonietta Loi, Ryan C. Chiechi, Siewert J. Marrink, Jan C. Hummelen, and L. Jan Anton Koster. Enhancing Molecular n-Type Doping of Donor–Acceptor Copolymers by Tailoring Side Chains. *Advanced Materials*, 30(7):1–9, 2018. `doi:10.1002/adma.201704630`.

[44] Shuo Chen and Zhifeng Ren. Recent progress of half-Heusler for Moderate Temperature Thermoelectric Applications. *Materials Today*, 16(10):387–395, 2013. `doi:10.1016/j.mattod.2013.09.015`.

[45] Bed Poudel, Qing Hao, Yi Ma, Yucheng Lan, Austin Minnich, Bo Yu, Xiao Yan, Dezhi Wang, Andrew Muto, Daryoosh Vashaee, Xiaoyuan Chen, Junming Liu, Mildred S. Dresselhaus, Gang Chen, and Zhifeng Ren. High-thermoelectric Performance of Nanostructured Bismuth Antimony Telluride Bulk Alloys. *Science*, 320(5876):634–638, 2008. `doi:10.1126/science.1156446`.

[46] Kuei Fang Hsu, Sim Loo, Fu Guo, Wei Chen, Jeffrey S. Dyck, Ctirad Uher, Tim Hogan, E. K. Polychroniadis, and Mercouri G. Kanatzidis. Cubic $AgPb_mSbTe_{2+m}$: Bulk Thermoelectric Materials with High Figure of Merit. *Science*, 303(5659):818–821, 2004. `doi:10.1126/science.1092963`.

[47] Kanishka Biswas, Jiaqing He, Qichun Zhang, Guoyu Wang, Ctirad Uher, Vinayak P Dravid, and Mercouri G Kanatzidis. Strained endotaxial nanostructures with high thermoelectric figure of merit. *Nature Chemistry*, 3(2):160–166, 2011. `doi:10.1038/nchem.955`.

[48] Han Li, Xinfeng Tang, Qingjie Zhang, and Ctirad Uher. High performance $In_xCe_yCo_4Sb_{12}$ thermoelectric materials with in situ forming nanostructured InSb phase. *Applied Physics Letters*, 94(10):92–95, 2009. `doi:10.1063/1.3099804`.

[49] Shuo Chen, Kevin C. Lukas, Weishu Liu, Cyril P. Opeil, Gang Chen, and Zhifeng Ren. Effect of Hf concentration on thermoelectric properties of nanostructured n-type half-heusler materials $Hf_xZr_{1-x}NiSn_{0.99}Sb_{0.01}$. *Advanced Energy Materials*, 3(9):1210–1214, 2013. doi:10.1002/aenm.201300336.

[50] H. Julian Goldsmid. *Introduction to Thermoelectricity*. Springer Berlin Heidelberg, Berlin, Heidelberg, 2010. doi:10.1007/978-3-642-00716-3_2.

[51] Jean Charles Athanase Peltier. *Nouvelles expériences sur la caloricité des courans électriques*. 1834.

[52] B. Sherman, R. R. Heikes, and R. W. Ure. Calculation of efficiency of thermoelectric devices. *Journal of Applied Physics*, 31(1):1–16, 1960. doi:10.1063/1.1735380.

[53] Frank P Incropera, David P DeWitt, Theodore L Bergman, Adrienne S Lavine, et al. *Fundamentals of heat and mass transfer*, volume 6. Wiley New York, 1996.

[54] David Halliday, Robert Resnick, and Jearl Walker. *Fundamentals of physics, chapters 33-37*. John Wiley & Sons, 2010.

[55] David Michael Rowe. *CRC handbook of thermoelectrics*. CRC press, 2018.

[56] Sadi Carnot. *Réflexions sur la puissance motrice du feu*. Number 26. Vrin, 1978.

[57] Ki-iti Horai. Thermal conductivity of rock-forming minerals. *Journal of geophysical research*, 76(5):1278–1308, 1971.

[58] W David Kingery, Harvey Kent Bowen, and Donald R Uhlmann. *Introduction to ceramics*, volume 17. John wiley & sons, 1976.

[59] Fumio Miyashiro, Takashi Takahashi, Nobuo Iwase, Akihiko Tsuge, and Masako Nakahashi. High Thermal Conductivity Aluminum Nitride Ceramic Substrates and Packages. *IEEE Transactions on Components, Hybrids, and Manufacturing Technology*, 13(2):313–319, 1990. doi:10.1109/33.56163.

[60] Jin-Cheng Zheng. Recent advances on thermoelectric materials. *Frontiers of Physics in China*, 3(3):269–279, 2008. doi:10.1007/s11467-008-0028-9.

[61] Luo Qinghai, Wang Yanjin, and Zhang Pengfei. A novel thermoelectric air-conditioner for a truck cab. In *2010 International Conference on Advances in Energy Engineering*, pages 178–181, 2010. doi:10.1109/ICAEE.2010.5557585.

[62] F. Stablers. Benefits of Thermoelectric Technology for the Automobile. Technical report, San Diego, CA, 2011. URL: https://www.energy.gov/eere/vehicles/articles/benefits-thermoelectric-technology-automobile.

[63] GMZ Energy Announces 1,000 Watt High-Temperature Thermoelectric Generator for U.S. Military, 2014. URL: https://www.businesswire.com/multimedia/home/20141203005186/en/.

[64] Zhongliang Ouyang and Dawen Li. Modelling of Segmented High-performance Thermoelectric Generators with Effects of Thermal radiation, Electrical and Thermal Contact Resistances. *Scientific Reports*, 6(April):1–12, 2016. `doi:10.1038/srep24123`.

[65] R. G. Moore. Exact Computer Solution of Segmented Thermoelectric Devices. *Advanced Energy Conversion*, 2(C):183–195, jan 1962. `doi:10.1016/0365-1789(62)90023-1`.

[66] G. Jeffrey Snyder. Application of the Compatibility Factor to the Design of Segmented and Cascaded Thermoelectric Generators. *Applied Physics Letters*, 84(13):2436–2438, 2004. `doi:10.1063/1.1689396`.

[67] Thierry Caillat, Jean-Pierre Fleurial, and Alex Borshchevsky. Development of High Efficiency Thermoelectric Generators using Advanced Thermoelectric Materials. *AIP Conference Proceedings*, 1647(April 2008):1647–1651, 2008. `doi:10.1063/1.54794`.

[68] Hua Tian, Na Jiang, Qi Jia, Xiuxiu Sun, Gequn Shu, and Xingyu Liang. Comparison of Segmented and Traditional Thermoelectric Generator for Waste Heat Recovery of Diesel Engine. *Energy Procedia*, 75:590–596, 2015. `doi:10.1016/j.egypro.2015.07.461`.

[69] Qihao Zhang, Jincheng Liao, Yunshan Tang, Ming Gu, Chen Ming, Pengfei Qiu, Shengqiang Bai, Xun Shi, Ctirad Uher, and Lidong Chen. Realizing a Thermoelectric Conversion Efficiency of 12% in Bismuth Telluride/Skutterudite Segmented Modules through Full-parameter Optimization and Energy-loss Minimized Integration. *Energy and Environmental Science*, 10(4):956–963, 2017. `doi:10.1039/c7ee00447h`.

[70] Sae Oki and Ryosuke Suzuki. Performance Simulation of a Flat-Plate Thermoelectric Module Consisting of Square Truncated Pyramid Elements. *Journal of Electronic Materials*, 46(5):2691–2696, 2017. `doi:10.1007/s11664-016-4905-7`.

[71] B. S. Yilbas and H. Ali. Thermoelectric generator performance analysis: Influence of pin tapering on the first and second law efficiencies. *Energy Conversion and Management*, 100:138–146, may 2015. `doi:10.1016/j.enconman.2015.05.005`.

[72] Yaoguang Shi, Deqing Mei, Zhehe Yao, Yancheng Wang, Haiyan Liu, and Zichen Chen. Nominal power density analysis of thermoelectric pins with non-constant cross sections. *Energy Conversion and Management*, 97:1–6, 2015. `doi:10.1016/j.enconman.2015.02.046`.

[73] Ran He, Gabi Schierning, and Kornelius Nielsch. Thermoelectric Devices: A Review of Devices, Architectures, and Contact Optimization. *Advanced Materials Technologies*, 3(4):1700256, apr 2018. `doi:10.1002/admt.201700256`.

[74] Gao Min and D. M. Rowe. Ring-structured thermoelectric module. *Semiconductor Science and Technology*, 22(8):880–883, 2007. `doi:10.1088/0268-1242/22/8/009`.

[75] Jovovic Vladimir. Thermoelectric Waste Heat Recovery Program for Passenger Vehicles. Technical report, U.S. Department of Energy, United States, 2015. `doi:10.2172/1337561`.

[76] Xiaoyuan Zhou, Yanci Yan, Xu Lu, Hangtian Zhu, Xiaodong Han, Gang Chen, and Zhifeng Ren. Routes for high-performance thermoelectric materials, nov 2018. `doi:10.1016/j.mattod.2018.03.039`.

[77] Soufiane El Oualid, Francis Kosior, Anne Dauscher, Christophe Candolfi, Gerhard Span, Ervin Mehmedovic, Janina Paris, and Bertrand Lenoir. Innovative design of bismuth-telluride-based thermoelectric micro-generators with high output power. *Energy and Environmental Science*, 13(10):3579–3591, 2020. `doi:10.1039/d0ee02579h`.

[78] Hailong He, Yi Wu, Weiwei Liu, Mingzhe Rong, Zhenxuan Fang, and Xiaojun Tang. Comprehensive Modeling for Geometric Optimization of a Thermoelectric Generator Module. *Energy Conversion and Management*, 183(October 2018):645–659, 2019. `doi:10.1016/j.enconman.2018.12.087`.

[79] Samson Shittu, Guiqiang Li, Xin Tang, Xudong Zhao, Xiaoli Ma, and Ali Badiei. Analysis of thermoelectric geometry in a concentrated photovoltaic-thermoelectric under varying weather conditions. *Energy*, 202:117742, 2020. `doi:10.1016/j.energy.2020.117742`.

[80] Wei Hsin Chen, Yi Xian Lin, Xiao Dong Wang, and Yu Li Lin. A Comprehensive Analysis of the Performance of Thermoelectric Generators with Constant and Variable Properties. *Applied Energy*, 241(November 2018):11–24, 2019. `doi:10.1016/j.apenergy.2019.02.083`.

[81] Gao Min and D. M. Rowe. Improved model for calculating the coefficient of performance of a Peltier module. *Energy Conversion and Management*, 41(2):163–171, 2000. `doi:10.1016/S0196-8904(99)00102-8`.

[82] Xiaolong Gou, Heng Xiao, and Suwen Yang. Modeling, experimental study and optimization on low-temperature waste heat thermoelectric generator system. *Applied Energy*, 87(10):3131–3136, 2010. `doi:10.1016/j.apenergy.2010.02.013`.

[83] Daniel W. Newbrook, Ruomeng Huang, Stephen P. Richards, Shivank Sharma, Gillian Reid, Andrew L. Hector, and C. H. de Groot. Mathematical Model and Optimization of a Thin-film Thermoelectric Generator. *JPhys Energy*, 2(1), 2020. `doi:10.1088/2515-7655/ab4242`.

[84] Zu Guo Shen, Shuang Ying Wu, Lan Xiao, and Gang Yin. Theoretical Modeling of Thermoelectric Generator with Particular Emphasis on the Effect of Side Surface Heat Transfer. *Energy*, 95:367–379, 2016. `doi:10.1016/j.energy.2015.12.005`.

[85] C. Suter, Z. R. Jovanovic, and A. Steinfeld. A $1kW_e$ Thermoelectric Stack for Geothermal Power Generation - Modeling and Geometrical Optimization. *Applied Energy*, 99:379–385, 2012. `doi:10.1016/j.apenergy.2012.05.033`.

[86] Lei Zhu, Huaqi Li, Sen Chen, Xiaoyan Tian, Xiaoya Kang, Xinbiao Jiang, and Suizheng Qiu. Optimization Analysis of a Segmented Thermoelectric Generator Based on Genetic Algorithm. *Renewable Energy*, 156:710–718, 2020. `doi:10.1016/j.renene.2020.04.120`.

[87] Wei Hsin Chen, Po Hua Wu, and Yu Li Lin. Performance optimization of thermoelectric generators designed by multi-objective genetic algorithm. *Applied Energy*, 209(July 2017):211–223, 2018. `doi:10.1016/j.apenergy.2017.10.094`.

[88] Wei Hsin Chen and Yi Bin Chiou. Geometry design for maximizing output power of segmented skutterudite thermoelectric generator by evolutionary computation. *Applied Energy*, 274(February):115296, 2020. `doi:10.1016/j.apenergy.2020.115296`.

[89] Jing Hui Meng, Hao Chi Wu, Liang Wang, Gui Lu, Kai Zhang, and Wei Mon Yan. Thermal management of a flexible controlled thermoelectric energy conversion-utilization system using a multi-objective optimization. *Applied Thermal Engineering*, 179(July):115721, 2020. `doi:10.1016/j.applthermaleng.2020.115721`.

[90] Zhichun Liu, Shiping Zhu, Ya Ge, Feng Shan, Lingping Zeng, and Wei Liu. Geometry optimization of two-stage thermoelectric generators using simplified conjugate-gradient method. *Applied Energy*, 190:540–552, 2017. `doi:10.1016/j.apenergy.2017.01.002`.

[91] Ya Ge, Zhichun Liu, Henan Sun, and Wei Liu. Optimal Design of a Segmented Thermoelectric Generator Based on Three-dimensional Numerical Simulation and Multi-objective Genetic Algorithm. *Energy*, 147:1060–1069, 2018. `doi:10.1016/j.energy.2018.01.099`.

[92] Wei Hsin Chen, Shih Rong Huang, and Yu Li Lin. Performance Analysis and Optimum Operation of a Thermoelectric Generator by Taguchi Method. *Applied Energy*, 158:44–54, 2015. `doi:10.1016/j.apenergy.2015.08.025`.

[93] Grant W Petty. *A first course in atmospheric radiation*. Sundog Publishing LLC, 2023.

[94] S. Catalanotti, V. Cuomo, G. Piro, D. Ruggi, V. Silvestrini, and G. Troise. The radiative cooling of selective surfaces. *Solar Energy*, 17(2):83–89, may 1975. `doi:10.1016/0038-092X(75)90062-6`.

[95] C. G. Granqvist and A. Hjortsberg. Surfaces for radiative cooling: Silicon monoxide films on aluminum. *Applied Physics Letters*, 36(2):139–141, 1980. `doi:10.1063/1.91406`.

[96] Muhammed Ali Kecebas, M. Pinar Menguc, Ali Kosar, and Kursat Sendur. Spectrally selective filter design for passive radiative cooling. *Journal of the Optical Society of America B*, 37(4):1173, 2020. `doi:10.1364/josab.384181`.

[97] Yao Zhai, Yaoguang Ma, Sabrina N David, Dongliang Zhao, Runnan Lou, Gang Tan, Ronggui Yang, and Xiaobo Yin. Scalable-manufactured randomized glass-polymer hybrid metamaterial for daytime radiative cooling. *Science*, 355(6329):1062–1066, mar 2017. `doi:10.1126/science.aai7899`.

[98] Eden Rephaeli, Aaswath Raman, and Shanhui Fan. Ultrabroadband photonic structures to achieve high-performance daytime radiative cooling. *Nano Letters*, 13(4):1457–1461, 2013. `doi:10.1021/nl4004283`.

[99] Mehdi Zeyghami, D. Yogi Goswami, and Elias Stefanakos. A review of clear sky radiative cooling developments and applications in renewable power systems and passive building cooling. *Solar Energy Materials and Solar Cells*, 178(January):115–128, 2018. `doi:10.1016/j.solmat.2018.01.015`.

[100] Bin Zhao, Mingke Hu, Xianze Ao, Nuo Chen, Qingdong Xuan, Yuehong Su, and Gang Pei. A novel strategy for a building-integrated diurnal photovoltaic and all-day radiative cooling system. *Energy*, 183:892–900, 2019. `doi:10.1016/j.energy.2019.06.166`.

[101] Zijie Shi, Kai Zhang, Kaiyu Jiang, Haoran Li, Peiliang Ye, Haibin Yang, and Omid Mahian. Maximizing energy generation: A study of radiative cooling-based thermoelectric power devices. *Energy*, 274:127283, 2023. `doi:10.1016/j.energy.2023.127283`.

[102] G. Jeffrey Snyder and Tristan S. Ursell. Thermoelectric efficiency and compatibility. *Physical Review Letters*, 91(14):148301/1–148301/4, 2003. `doi:10.1103/PhysRevLett.91.148301`.

[103] Ashish Kumar Chowdhary, Veluri Anurag Reddy, and Debabrata Sikdar. Nanophotonics-Enabled High-Efficiency Selective Solar Absorbers for Waste Heat Management. *IEEE Transactions on Nanotechnology*, 21:131–136, 2022. `doi:10.1109/TNANO.2022.3148333`.

[104] Aaswath P. Raman, Wei Li, and Shanhui Fan. Generating Light from Darkness. *Joule*, 3(11):2679–2686, 2019. `doi:10.1016/j.joule.2019.08.009`.

[105] Maciej Haras and Thomas Skotnicki. Thermoelectricity for IoT – A review. *Nano Energy*, 54(August):461–476, 2018. `doi:10.1016/j.nanoen.2018.10.013`.

[106] Zhibing Zhan, Mohamed ElKabbash, Zihao Li, Xiaoyun Li, Jihua Zhang, James Rutledge, Subhash Singh, and Chunlei Guo. Enhancing thermoelectric output power via radiative cooling with nanoporous alumina. *Nano Energy*, 65(August):104060, 2019. `doi:10.1016/j.nanoen.2019.104060`.

[107] Salman Khan, Jiyong Kim, Kyeongman Roh, Gimin Park, and Woochul Kim. High power density of radiative-cooled compact thermoelectric generator based on body heat harvesting. *Nano Energy*, 87(April):106180, 2021. `doi:10.1016/j.nanoen.2021.106180`.

[108] Yijie Liu, Shuaihang Hou, Xiaodong Wang, Li Yin, Zuoxu Wu, Xinyu Wang, Jun Mao, Jiehe Sui, Xingjun Liu, Qian Zhang, Zhiguo Liu, and Feng Cao. Passive Radiative Cooling Enables Improved Performance in Wearable Thermoelectric Generators. *Small*, 18(10):1–8, 2022. `doi:10.1002/smll.202106875`.

[109] Zhilin Xia, Zhenfei Zhang, Zhenghua Meng, Liyun Ding, and Zhongquan Yu. Thermoelectric Generator Using Space Cold Source. *ACS Applied Materials and Interfaces*, 11(37):33941–33945, 2019. `doi:10.1021/acsami.9b10981`.

[110] Erzhen Mu, Zhenhua Wu, Zhimao Wu, Xiang Chen, Yang Liu, Xuecheng Fu, and Zhiyu Hu. A novel self-powering ultrathin TEG device based on micro/nano emitter for radiative cooling. *Nano Energy*, 55(September 2018):494–500, 2019. `doi:10.1016/j.nanoen.2018.10.057`.

[111] Jia Liang, Muzhang Huang, Xuefei Zhang, and Chunlei Wan. Structural design for wearable self-powered thermoelectric modules with efficient temperature difference utilization and high normalized maximum power density. *Applied Energy*, 327(May):120067, 2022. `doi:10.1016/j.apenergy.2022.120067`.

[112] Ashish K. Chowdhary and Debabrata Sikdar. Design of electrotunable all-weather smart windows. *Solar Energy Materials and Solar Cells*, 222:110921, 2021. `doi:10.1016/j.solmat.2020.110921`.

[113] Junwei Liu, Ji Zhang, Jianjuan Yuan, Debao Zhang, Jincheng Xing, and Zhihua Zhou. Model development and performance evaluation of thermoelectric and radiative cooling module to achieve all-day power generation. *Solar Energy Materials and Solar Cells*, 220(July 2020):110855, 2021. `doi:10.1016/j.solmat.2020.110855`.

[114] Tianjun Liao, Qidong Xu, Yawen Dai, Chun Cheng, Qijiao He, and Meng Ni. Radiative cooling-assisted thermoelectric refrigeration and power systems: Coupling properties and parametric optimization. *Energy*, 242:122546, 2022. `doi:10.1016/j.energy.2021.122546`.

[115] Bin Zhao, Gang Pei, and Aaswath P. Raman. Modeling and optimization of radiative cooling based thermoelectric generators. *Applied Physics Letters*, 117(16), 2020. `doi:10.1063/5.0022667`.

[116] Md Muntasir Hossain and Min Gu. Radiative cooling: Principles, progress, and potentials. *Advanced Science*, 3(7):1–10, 2016. `doi:10.1002/advs.201500360`.

[117] B. A. Kimball, S. B. Idso, and J. K. Aase. A model of thermal radiation from partly cloudy and overcast skies. *Water Resources Research*, 18(4):931–936, 1982. `doi:10.1029/WR018i004p00931`.

[118] J. Khedari, J. Waewsak, S. Thepa, and J. Hirunlabh. Field investigation of night radiation cooling under tropical climate. *Renewable Energy*, 20(2):183–193, 2000. `doi:10.1016/S0960-1481(99)00104-4`.

[119] Lyu Zhou, Jacob Rada, Yanpei Tian, Yu Han, Zhiping Lai, Matthew F. McCabe, and Qiaoqiang Gan. Radiative cooling for energy sustainability: Materials, systems, and applications. *Physical Review Materials*, 6(9):1–22, 2022. `doi:10.1103/physrevmaterials.6.090201`.

[120] Pradeepkumar Sundarraj, Dipak Maity, Susanta Sinha Roy, and Robert A. Taylor. Recent advances in thermoelectric materials and solar thermoelectric generators-a critical review. *RSC Advances*, 4(87):46860–46874, 2014. `doi:10.1039/c4ra05322b`.

[121] Umar Abubakar Saleh, Muhammad Akmal Johar, Siti Amely Binti Jumaat, Muhammad Nazri Rejab, and Wan Akashah Wan Jamaludin. Evaluation of a PV-TEG Hybrid System Configuration for an Improved Energy Output: A Review. *International Journal of Renewable Energy Development*, 10, 12 2020. `doi:10.14710/ijred.0.33917`.

[122] Priscilla Huen and Walid A. Daoud. Advances in hybrid solar photovoltaic and thermoelectric generators. *Renewable and Sustainable Energy Reviews*, 72(November 2016):1295–1302, 2017. `doi:10.1016/j.rser.2016.10.042`.

[123] H J Goldsmid, J E Giutronich, and M M Kaila. Solar thermoelectric generation using bismuth telluride alloys. *Solar Energy*, 24(5):435–440, 1980. `doi:10.1016/0038-092X(80)90311-4`.

[124] R. Bjørk and K. K. Nielsen. The performance of a combined solar photovoltaic (PV) and thermoelectric generator (TEG) system. *Solar Energy*, 120:187–194, 2015. `doi:10.1016/j.solener.2015.07.035`.

[125] Mehdi Alian Fini, Derrick Gharapetian, and Masoud Asgari. Efficiency improvement of hybrid PV-TEG system based on an energy, exergy, energy-economic and environmental analysis; experimental, mathematical and numerical approaches. *Energy Conversion and Management*, 265(December 2021):115767, 2022. `doi:10.1016/j.enconman.2022.115767`.

[126] Adham Makki, Siddig Omer, Yuehong Su, and Hisham Sabir. Numerical investigation of heat pipe-based photovoltaic-thermoelectric generator (HP-PV/TEG) hybrid system. *Energy Conversion and Management*, 112:274–287, 2016. `doi:10.1016/j.enconman.2015.12.069`.

[127] Challa Babu and P. Ponnambalam. The theoretical performance evaluation of hybrid PV-TEG system. *Energy Conversion and Management*, 173(April):450–460, 2018. `doi:10.1016/j.enconman.2018.07.104`.

[128] Wenbo Gu, Tao Ma, Aotian Song, Meng Li, and Lu Shen. Mathematical modelling and performance evaluation of a hybrid photovoltaic-thermoelectric system. *Energy Conversion and Management*, 198(June):111800, 2019. `doi:10.1016/j.enconman.2019.111800`.

[129] P. Motiei, M. Yaghoubi, and E. GoshtasbiRad. Transient simulation of a hybrid photovoltaic-thermoelectric system using a phase change material. *Sustainable Energy Technologies and Assessments*, 34(April):200–213, 2019. `doi:10.1016/j.seta.2019.05.004`.

[130] Samson Shittu, Guiqiang Li, Xudong Zhao, Yousef Golizadeh Akhlaghi, Xiaoli Ma, and Min Yu. Comparative study of a concentrated photovoltaic-thermoelectric system with and without flat plate heat pipe. *Energy Conversion and Management*, 193(April):1–14, 2019. `doi:10.1016/j.enconman.2019.04.055`.

[131] Ya Ge, Qiyin Xiao, Wenhao Wang, Yousheng Lin, and Si Min Huang. Design of high-performance photovoltaic-thermoelectric hybrid systems using multi-objective genetic algorithm. *Renewable Energy*, 200(August):136–145, 2022. `doi:10.1016/j.renene.2022.09.091`.

[132] S. Mahmoudinezhad, A. Rezania, and L. A. Rosendahl. Behavior of hybrid concentrated photovoltaic-thermoelectric generator under variable solar radiation. *Energy Conversion and Management*, 164(March):443–452, 2018. `doi:10.1016/j.enconman.2018.03.025`.

[133] Yang Cai, Lei Wang, Wei Wei Wang, Di Liu, and Fu Yun Zhao. Solar energy harvesting potential of a photovoltaic-thermoelectric cooling and power generation system: Bidirectional modeling and performance optimization. *Journal of Cleaner Production*, 254:120150, 2020. `doi:10.1016/j.jclepro.2020.120150`.

[134] H. Hashim, J. J. Bomphrey, and G. Min. Model for geometry optimisation of thermoelectric devices in a hybrid PV/TE system. *Renewable Energy*, 87:458–463, 2016. `doi:10.1016/j.renene.2015.10.029`.

[135] Trevor Hocksun Kwan and Xiaofeng Wu. Power and mass optimization of the hybrid solar panel and thermoelectric generators. *Applied Energy*, 165:297–307, 2016. `doi:10.1016/j.apenergy.2015.12.016`.

[136] Samson Shittu, Guiqiang Li, Xudong Zhao, and Xiaoli Ma. Series of detail comparison and optimization of thermoelectric element geometry considering the PV effect. *Renewable Energy*, 130:930–942, 2019. `doi:10.1016/j.renene.2018.07.002`.

[137] A. A. Kandil, Mohamed M. Awad, Gamal I. Sultan, and Mohamed S. Salem. Performance of a photovoltaic/thermoelectric generator hybrid system with a beam splitter under maximum permissible operating conditions. *Energy Conversion and Management*, 280(October 2022):116795, 2023. `doi:10.1016/j.enconman.2023.116795`.

[138] D L Evans. Simplified method for predicting photovoltaic array output. *Solar Energy*, 27(6):555–560, 1981. `doi:10.1016/0038-092X(81)90051-7`.

[139] M. I. Jordan and T. M. Mitchell. Machine learning: Trends, perspectives, and prospects. *Science*, 349(6245):255–260, 2015. `doi:10.1126/science.aaa8415`.

[140] Jouko Lampinen and Aki Vehtari. Bayesian approach for neural networks - Review and case studies. *Neural Networks*, 14(3):257–274, 2001. `doi:10.1016/S0893-6080(00)00098-8`.

[141] Gérard Biau and Erwan Scornet. A random forest guided tour. *Test*, 25(2):197–227, 2016. `doi:10.1007/s11749-016-0481-7`.

[142] Mariana Belgiu and Lucian Drăgu. Random forest in remote sensing: A review of applications and future directions. *ISPRS Journal of Photogrammetry and Remote Sensing*, 114:24–31, 2016. `doi:10.1016/j.isprsjprs.2016.01.011`.

[143] Yann Lecun, Yoshua Bengio, and Geoffrey Hinton. Deep learning. *Nature*, 521(7553):436–444, 2015. `doi:10.1038/nature14539`.

[144] Ajay Shrestha and Ausif Mahmood. Review of deep learning algorithms and architectures. *IEEE Access*, 7:53040–53065, 2019. `doi:10.1109/ACCESS.2019.2912200`.

[145] Dac Khuong Bui, Tuan Ngoc Nguyen, Tuan Duc Ngo, and H. Nguyen-Xuan. An artificial neural network (ANN) expert system enhanced with the electromagnetism-based firefly algorithm (EFA) for predicting the energy consumption in buildings. *Energy*, 190:116370, 2020. `doi:10.1016/j.energy.2019.116370`.

[146] Osama S. Ebrahim, Mohamed A. Badr, Ali S. Elgendy, and Praveen K. Jain. ANN-based optimal energy control of induction motor drive in pumping applications. *IEEE Transactions on Energy Conversion*, 25(3):652–660, 2010. `doi:10.1109/TEC.2010.2041352`.

[147] Alberto Pliego Marugán, Fausto Pedro García Márquez, Jesus María Pinar Perez, and Diego Ruiz-Hernández. A survey of artificial neural network in wind energy systems. *Applied Energy*, 228(April):1822–1836, 2018. `doi:10.1016/j.apenergy.2018.07.084`.

[148] Harish Kumar Ghritlahre and Radha Krishna Prasad. Application of ANN technique to predict the performance of solar collector systems - A review. *Renewable and Sustainable Energy Reviews*, 84(September 2017):75–88, 2018. `doi:10.1016/j.rser.2018.01.001`.

[149] Fermín Rodríguez, Alice Fleetwood, Ainhoa Galarza, and Luis Fontán. Predicting solar energy generation through artificial neural networks using weather forecasts for microgrid control. *Renewable Energy*, 126:855–864, 2018. `doi:10.1016/j.renene.2018.03.070`.

[150] Z. H. Wang, Y. J. Ma, G. H. Tang, Hu Zhang, F. Ji, and Q. Sheng. Integration of thermal insulation and thermoelectric conversion embedded with phase change materials. *Energy*, 278(December 2022), 2023. `doi:10.1016/j.energy.2023.127784`.

[151] Simon Haykin. *Neural networks: a comprehensive foundation*. Prentice Hall PTR, 1998.

[152] Vinod Nair and Geoffrey E. Hinton. Rectified linear units improve Restricted Boltzmann machines. *ICML 2010 - Proceedings, 27th International Conference on Machine Learning*, (3):807–814, 2010.

[153] Christopher M Bishop. *Neural networks for pattern recognition*. Oxford university press, 1995.

[154] Trevor Hastie, Robert Tibshirani, Jerome H Friedman, and Jerome H Friedman. *The elements of statistical learning: data mining, inference, and prediction*, volume 2. Springer, 2009.

[155] Sun-Chong Wang. Artificial Neural Network. In *Interdisciplinary Computing in Java Programming*, pages 81–100. Springer US, Boston, MA, 2003. `doi:10.1007/978-1-4615-0377-4_5`.

[156] Annu Lambora, Kunal Gupta, and Kriti Chopra. Genetic algorithm- a literature review. In *2019 International Conference on Machine Learning, Big Data, Cloud and Parallel Computing (COMITCon)*, pages 380–384, 2019. `doi:10.1109/COMITCon.2019.8862255`.

[157] DE Goldberg. *Genetic Algorithms in Search, Optimization and Machine Learning. Addison-Wesley Longman Publishing Co., Inc.* Addison Wesley, 1989.

[158] Melanie Mitchell. *An introduction to genetic algorithms*. MIT press, 1998.

[159] Samson Shittu, Guiqiang Li, Xudong Zhao, Xiaoli Ma, Yousef Golizadeh Akhlaghi, and Emmanuel Ayodele. High Performance and Thermal Stress Analysis of a Segmented Annular Thermoelectric Generator. *Energy Conversion and Management*, 184(October 2018):180–193, 2019. `doi:10.1016/j.enconman.2019.01.064`.

[160] A. J. Westlake. Introduction to Probability and Statistics. *Journal of the Royal Statistical Society Series D: The Statistician*, 18(4):417–417, 12 2018. `doi:10.2307/2987143`.

[161] Diederik P. Kingma and Jimmy Ba. Adam: A method for stochastic optimization, 2017. `doi:10.48550/arXiv.1412.6980`.

[162] Kaiming He, Xiangyu Zhang, Shaoqing Ren, and Jian Sun. Delving deep into rectifiers: Surpassing human-level performance on imagenet classification. In *Proceedings of the IEEE international conference on computer vision*, pages 1026–1034, 2015.

[163] Philip Kosky, Robert Balmer, William Keat, and George Wise. Chapter 12 - mechanical engineering. In Philip Kosky, Robert Balmer, William Keat, and George Wise, editors, *Exploring Engineering (Third Edition)*, pages 259–281. Academic Press, Boston, third edition edition, 2013. `doi:10.1016/B978-0-12-415891-7.00012-1`.

[164] Xiao Yan, Bed Poudel, Yi Ma, W. S. Liu, G. Joshi, Hui Wang, Yucheng Lan, Dezhi Wang, Gang Chen, and Z. F. Ren. Experimental Studies on Anisotropic Thermoelectric Properties and Structures of n-type $Bi_2Te_{2.7}Se_{0.3}$. *Nano Letters*, 10(9):3373–3378, 2010. `doi:10.1021/nl101156v`.

[165] Liangwei Fu, Meijie Yin, Di Wu, Wei Li, Dan Feng, Li Huang, and Jiaqing He. Large Enhancement of Thermoelectric Properties in N-type PbTe via Dual-site Point Defects. *Energy and Environmental Science*, 10(9):2030–2040, 2017. `doi:10.1039/c7ee01871a`.

[166] Qian Zhang, Feng Cao, Weishu Liu, Kevin Lukas, Bo Yu, Shuo Chen, Cyril Opeil, David Broido, Gang Chen, and Zhifeng Ren. Heavy Doping and Band Engineering by Potassium to Improve the Thermoelectric Figure of Merit in P-type PbTe, PbSe, and $PbTe_{1-y}Se_y$. *Journal of the American Chemical Society*, 134(24):10031–10038, 2012. `doi:10.1021/ja301245b`.

[167] Junwei Liu, Ji Zhang, Jianjuan Yuan, Debao Zhang, Jincheng Xing, and Zhihua Zhou. Model development and performance evaluation of thermoelectric and radiative cooling module to achieve all-day power generation. *Solar Energy Materials and Solar Cells*, 220(July 2020):110855, 2021. `doi:10.1016/j.solmat.2020.110855`.

[168] Peng Sheng Wei, Hsuan Han Chiu, Yin Chih Hsieh, Da Lun Yen, Chieh Lee, Yi Cheng Tsai, and Te Chuan Ting. Absorption coefficient of water vapor across atmospheric troposphere layer. *Heliyon*, 5(1):e01145, 2019. `doi:10.1016/j.heliyon.2019.e01145`.

[169] Xingshu Sun, Yubo Sun, Zhiguang Zhou, Muhammad Ashraful Alam, and Peter Bermel. Radiative sky cooling: Fundamental physics, materials, structures, and applications. *Nanophotonics*, 6(5):997–1015, 2017. `doi:10.1515/nanoph-2017-0020`.

[170] Bruno Lorenzi, Maurizio Acciarri, and Dario Narducci. Analysis of Thermal Losses for a Variety of Single-Junction Photovoltaic Cells: An Interesting Means of Thermoelectric Heat Recovery. *Journal of Electronic Materials*, 44(6):1809–1813, 2015. `doi:10.1007/s11664-014-3562-y`.

[171] E. Skoplaki and J. A. Palyvos. Operating temperature of photovoltaic modules: A survey of pertinent correlations. *Renewable Energy*, 34(1):23–29, 2009. `doi:10.1016/j.renene.2008.04.009`.

[172] Martin A. Green. Self-consistent optical parameters of intrinsic silicon at 300 K including temperature coefficients. *Solar Energy Materials and Solar Cells*, 92(11):1305–1310, 2008. `doi:10.1016/j.solmat.2008.06.009`.

[173] D Aaron R Barkhouse, Oki Gunawan, Tayfun Gokmen, Teodor K Todorov, and David B Mitzi. Yield predictions for photovoltaic power plants:empirical validation,recent advances and remaining uncertainties. *Progress in Photovoltaics: Research and Applications*, 20(1):6–11, 2015. `doi:10.1002/pip.1160`.

[174] Emilie Raoult, Romain Bodeux, Sebastien Jutteau, and Samuel Rives. Optical Characterizations and Modelling of Semitransparent Perovskite Solar Cells for Tandem Applications. *European Photovoltaic Solar Energy Conference and Exhibition (EU PVSEC)*, 36(October):757 – 763, 2019. `doi:10.4229/EUPVSEC20192019-3BV.2.53`.

[175] PV lighthouse, https://www.pvlighthouse.com.au, 2023. URL: `https://www.pvlighthouse.com.au/`.

[176] M. Mattei, G. Notton, C. Cristofari, M. Muselli, and P. Poggi. Calculation of the polycrystalline PV module temperature using a simple method of energy balance. *Renewable Energy*, 31(4):553–567, 2006. `doi:10.1016/j.renene.2005.03.010`.

[177] Ji cheng Zhou, Zhe Zhang, Han jian Liu, and Qiang Yi. Temperature distribution and back sheet role of polycrystalline silicon photovoltaic modules. *Applied Thermal Engineering*, 111:1296–1303, 2017. `doi:10.1016/j.applthermaleng.2016.10.095`.

[178] Rasmus Bjørk. The Universal Influence of Contact Resistance on the Efficiency of a Thermoelectric Generator. *Journal of Electronic Materials*, 44(8):2869–2876, aug 2015. `doi:10.1007/s11664-015-3731-7`.

[179] S. Mahmoudinezhad, D.T. Cotfas, P.A. Cotfas, Enok J.H. Skjølstrup, K. Pedersen, L. Rosendahl, and A. Rezania. Experimental investigation on spectrum beam splitting photovoltaic–thermoelectric generator under moderate solar concentrations. *Energy*, 238:121988, 2022. `doi:10.1016/j.energy.2021.121988`.